

**ELECTRODEPOSITION OF MULTI-VALENT METAL OXIDES AT 1-
METHYL-3-OCTYLIMIDAZOLIUM
BIS(TRIFLUOROMETHYLSULFONYL) IMIDE IONIC LIQUID -
CARBON PASTE ELECTRODE**

**A thesis submitted in partial fulfillment of the requirements for the degree
of Magister Scientiae, in the Department of Chemistry, University of the**

Western Cape



By

**UNIVERSITY of the
WESTERN CAPE
SIBUSISO QWESHA**

Supervisor: Professor Emmanuel I. Iwuoha

Co-supervisor: Dr. Tesfaye T. Waryo

Bellville – Cape Town – Republic of South Africa

November 2012

Page Left Blank



**Electrodeposition of Multi-Valent Metal Oxides at 1-Methyl-3-octylimidazolium
Bis(trifluoromethylsulfonyl)imide Ionic Liquid - Carbon Paste Electrode**

Sibusiso Qwesa

KEY WORDS

Carbon paste electrodes

Room temperature ionic liquids

1-Methyl-3-octylimidazolium bis(trifluoromethylsulfonyl) imide

Transition metal oxides

Manganese oxide

Iron oxide

Cobalt oxide

Tin oxide

Electrodeposition

Electrode material



Page Left Blank



ABSTRACT

A study on carbon paste electrode (CPE) materials containing 1-methyl-3-octylimidazolium bis(trifluoromethylsulfonyl) imide [MOIM[Tf_2N] – a hydrophobic room temperature ionic liquid (IL) - is reported. CPEs with (a) the IL as the only binder (ILCPE) and (b) 1:1 (v/v) IL: paraffin mixture as the binder (ILPCPE) were prepared, characterized, and applied to the electrodeposition of films of multivalent transition metal oxides (MV-TMO) from five precursor ions (Fe^{2+} , Mn^{2+} , Cu^{2+} , Co^{2+} , Ce^{4+}) in aq. KCl. Cyclic voltammetry (CV) showed a potential window of +1.5 V to -1.8 V regardless of the electrode type, including the traditional paraffin CP electrode (PCPE). However, the IL increased the background current by 100-folds relative to paraffin. The electrochemical impedance spectroscopy (EIS) of ILPCPE in aq. KCl (0.1M) revealed two phase angle maxima in contrast with the single maxima for PCPE and ILCP. The study also included the CV and EIS investigation of the electrode kinetics of the $Fe(CN)_6^{3-/4-}$ redox system at these electrodes. The electrodeposition of Fe^{2+} , Co^{2+} , and Mn^{2+} possibly in the form of the MV-TMOs Fe_xO_y , Co_xO_y , and Mn_xO_y , respectively, onto the electrodes was confirmed by the observation of new and stable cathodic and anodic peaks in a fresh precursor ion –free medium. CVs of H_2O_2 as a redox probe supported the same conclusions. Both ATR-FTIR spectra and SEM image of surface samples confirmed the formation of electrodeposited films. This study demonstrated that the use of this hydrophobic IL alone or in combination with paraffin as a binder gives viable alternative CPE materials with better performance for the electrodeposition of MV-TMOs films than the paraffin CPE. Thus, in combination with the easy preparation methods and physical “morpheability” in to any shape, these CPEs are potentially more useful in electrochemical technologies based on high surface-area MV-TMO films in general, and Mn_xO_y films in particular.

Page Left Blank



DECLARATION

I declare that **Electrodeposition of Multi-Valent Metal Oxides at 1-Methyl-3-octylimidazolium Bis(trifluoromethylsulfonyl)imide Ionic Liquid - Carbon Paste Electrode** is my own work, that it has not been submitted for any degree or examination in any other university, and that all the sources I have used or quoted have been indicated and acknowledged by complete references.

Sibusiso Qwesha

November 2012

Signed



Page Left Blank



ACKNOWLEDGEMENTS

Firstly, I would like to thank the most important presence in my life, God for all the strength, perseverance, guidance and, most of all, the blessings he has given me throughout the process. I would also like to express my deepest gratitude to Professor Emmanuel I. Iwuoha, for his offering me the opportunity to carry out study at the Sensorlab, for his continued support, encouragements and inspirational advises, which were very indispensable to the success of my study. My appreciation to my co-supervisor, Dr. Tesfaye T. Waryo, who introduced me into the world of applied electrochemistry, ionic liquids and carbon paste electrodes, is also beyond my expression- for his persistent encouragement, patience, guidance, and indispensable inputs during all phases of my study.

Great thanks also given to all colleagues in SensorLab and Department of Chemistry for their continued encouragement during my study period.

To my mother, Mrs. N. Qweshu, my Father, Mr. G. Qweshu, my brother, Akhona Qweshu, my sister, Libonge Qweshu, I would like to thank you for your prayers, support and love. I would also like to acknowledge Liziwe Mkutu (my girlfriend) and Thimna Mkutu (my son) for the love, encouragement and support they have shown me during the process.

Last but not least, I would like to acknowledge the National Research Foundation of South Africa for financially supporting my study for the past three years, and the University of the Western Cape for offering me the opportunity of enrollment to the MSc chemistry program.

Page Left Blank



CONFERENCES AND MANUSCRIPTS FROM THIS WORK

Sibusiso Qwasha, Tesfaye Waryo, Emmanuel Iwuoha, Electrochemistry of ferricyanide, iron, copper, manganese, cobalt, and cerium ions at 1-methyl-3-octyl imidazolium bis(trifluoromethylsulfonyl)imide – carbon paste electrodes, “10th International symposium on Kinetics in analytical Chemistry”, 02-04 Dec., 2009; Fountains Hotel, Cape Town.
<http://associated.sun.ac.za/UWC/KAC2009/index.htm> (POSTER)

Tesfaye Waryo, **Sibusiso Qwasha**, Emmanuel Iwuoha; “Electrochemical deposition of multivalent metal oxides at 1-methyl-3-octylimidazolium bis(trifluoromethylsulfonyl)imide - carbon paste electrodes; 10th International symposium on Kinetics in analytical Chemistry”.02-04 Dec. 2009; Fountains Hotel, Cape Town – Republic of South Africa.
<http://associated.sun.ac.za/UWC/KAC2009/index.htm> (ORAL)

Tesfaye T. Waryo, **Sibusiso Qwasha**, Priscilla G.L. Baker, Emmanuel I. Iwuoha Ionic liquid (1-methyl-3-octylimidazolium bis(trifluoromethylsulfonyl)imide)/ paraffin/ carbon paste electrode electrochemical properties, evaluation with the $\text{Fe}(\text{CN})_6^{3-}$ redox-probe, and application for oxy-iron-film electrodeposition (Manuscript submitted to: *Electrochimica Acta*)

Electrodeposition studies on iron, copper, manganese, cobalt, and cerium ions at Ionic liquid (1-methyl-3-octylimidazolium bis(trifluoromethylsulfonyl)imide)/ paraffin/ carbon paste electrode (Manuscript under preparation)

Electrodeposition of oxy/ hydroxyl manganese films at Ionic liquid (1-methyl-3-octylimidazolium bis(trifluoromethylsulfonyl)imide)/ paraffin/ carbon paste electrode (Manuscript under preparation)

Cyclic voltammetry and impedance spectroscopy of Ionic liquid (1-methyl-3-octylimidazolium bis(trifluoromethylsulfonyl)imide)/ paraffin/ carbon paste electrode in different electrolytes (manuscript under preparation)

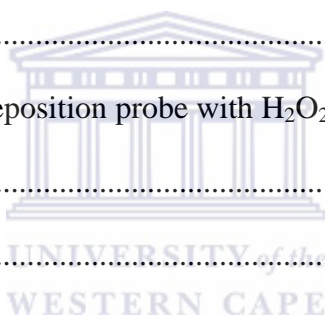


TABLE OF CONTENTS

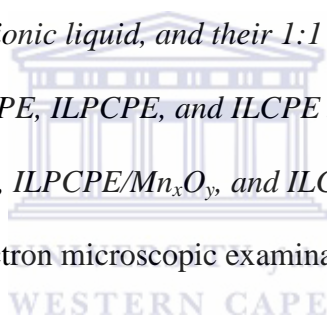
KEY WORDS.....	iii
ABSTRACT.....	v
DECLARATION.....	vii
ACKNOWLEDGEMENTS.....	ix
CONFERENCES AND MANUSCRIPTS FROM THIS WORK.....	xi
TABLE OF CONTENTS.....	xiii
LIST OF FIGURES.....	xix
1. INTRODUCTION.....	1
2. LITERATURE.....	3
2.1 Carbon Paste Electrodes (CPEs).....	3
2.2 Multivalent Metal Oxide – Modified CPEs.....	7
2.3 Room Temperature Ionic Liquids (RTILs).....	12
2.4 RTILs/CPEs as Electrodes.....	17
3. PRINCIPLES OF SELECTED ANALYTICAL METHODS.....	19
3.1 Cyclic Voltammetry (CV).....	19
3.2 Electrochemical Impedance Spectroscopy (EIS).....	23
3.3 Fourier Transform Infrared (FTIR) Spectroscopy.....	32
3.4. Microscopy Techniques.....	32

4.	EXPERIMENTAL.....	34
4.1	Chemicals and Materials	34
4.1.1	Chemicals.....	34
4.2	Carbon Paste Preparation & Electrode Construction	35
4.2.1	Paraffin/ carbon paste electrode (PCPE)	35
4.2.2	Ionic liquid/ paraffin/ carbon paste electrode (ILPCPE)	35
4.3	Electrochemical Measurements.....	36
4.4	ATR-FTIR Measurements.....	36
4.5	Preliminary Electrochemical Studies.....	37
4.6	Effecting and Probing of Metal oxide Species Electrodeposition.....	37
5.	RESULTS AND DISCUSSION.....	38
5.1	Preliminary Studies on as Prepared Ionic Liquid Carbon Paste Electrodes.....	38
5.1.1	Background cyclic voltammogram (CVs) in aq. KCl (0.1 M) solution ..	38
5.1.2	Cyclic voltammogram of $\text{Fe}(\text{CN})_6^{3-/4-}$	39
5.1.3	Cyclic voltammogram of H_2O_2 in aq. KCl (0.1 M) solution.	40
5.1.4	Scanning electron microscopic examination	41
5.2	Electrode Kinetics of $\text{Fe}(\text{CN})_6^{3-/4-}$ at PCPE, ILPCPE, and ILCPE.....	44
5.2.1	Cyclic voltammetry.....	44
5.2.2	Electrochemical impedance spectroscopy	46
5.3	Electrodeposition of Selected Transition Metal Ions in aq. KCl (0.1 M) solution.....	50
5.3.1	Electrodeposition cyclic voltammograms.....	50

	<i>Iron (II)</i>	50
	<i>Cobalt (II)</i>	51
	<i>Copper (II)</i>	52
	<i>Cerium (II)</i>	54
	<i>Manganese (II)</i>	55
5.3.2	Post-electrodeposition cyclic voltammograms in Aq KCl solution.....	56
	<i>Fe_xO_y films</i>	56
	<i>Co_xO_y films</i>	57
	<i>Cu_xO_y films</i>	58
	<i>Ce_xO_y films</i>	59
	<i>Mn_xO_y films</i>	60
5.3.3	Post-electrodeposition probe with H ₂ O ₂	62
	<i>Fe_xO_y films</i>	62
	<i>Co_xO_y films</i>	63
	<i>Cu_xO_y films</i>	64
	<i>Ce_xO_y films</i>	65
	<i>Mn_xO_y films</i>	66
5.4	Effect of Electrolyte Type on Mn _x O _y Electrodeposition	68
5.4.1	Electrodeposition	68
	<i>Aq. KCl as electrodeposition medium</i>	68
	<i>Aq. NaCl as electrodeposition medium</i>	69
	<i>Aq. KNO₃ as electrodeposition medium</i>	70
	<i>Aq. LiCl as electrodeposition medium</i>	72
	<i>Aq. NH₄Cl as electrodeposition medium</i>	73
	<i>Aq. NaOAC as electrodeposition medium</i>	74



	<i>Aq. NaClO₃ as electrodeposition medium</i>	75
5.4.2	Post-electro-deposition CVs in fresh Mn ²⁺ solution-free electrolytes.....	76
	<i>Aq. KCl solution as electrolyte</i>	76
	<i>Aq. NaCl solution as electrolyte</i>	78
	<i>Aq. KNO₃ solution as electrolyte</i>	79
	<i>Aq. LiCl solution as electrolyte</i>	80
	<i>Aq. NH₄Cl solution as electrolyte</i>	82
	<i>Aq. NaOAc solution as electrolyte</i>	84
	<i>Aq. NaClO₃ solution as electrolyte</i>	85
5.4.3	FTIR spectroscopic examination	87
	<i>Paraffin, the ionic liquid, and their 1:1 mixture</i>	87
	<i>Graphite, PCPE, ILPCPE, and ILCPE</i>	90
	<i>PCPE/Mn_xO_y, ILPCPE/Mn_xO_y, and ILCPE/Mn_xO_y</i>	90
5.4.4	Scanning electron microscopic examination	93
6.	SUMMARY AND CONCLUSIONS	96
7.	BIBLIOGRAPHY	99



LIST OF ABBREVIATIONS

[MOIM][Tf ₂ N]	: 1-Methyl-3-octylimidazolium bis(trifluoromethylsulfonyl)imide
ATR	: Attenuated total internal reflectance
ATR-FTIR	: Attenuated total reflectance – Fourier transform infrared spectroscopy
CNLS	: Complex non-linear least squares
CP	: Carbon paste
CPE	: Carbon paste electrode or the constant phase element
CV (or CVs)	: Cyclic voltammogram (or cyclic voltammograms)
EIS	: Electrochemical impedance spectroscopy or spectrum
IL (or RTIL)	: Ionic Liquids (or room temperature ionic liquid), also used to refer to [MOIM][Tf ₂ N] in this thesis
ILCPE	: Ionic liquid/ carbon paste electrode
ILPCPE	: Ionic liquid/ paraffin/ carbon paste electrode
PCPE	: Paraffin/ carbon paste electrode
SANS	: Small-angle neutron scattering
SEM	: Scanning electron microscopy
ZARC	: Impedance arc (semicircle)

Page Left Blank



LIST OF FIGURES

Figure 1: Microscopic model of plain CPE surface [17].	5
Figure 2: Molecular structure of the hydrophobic room temperature ionic 1-methyl-3-octyl imidazolium bis(trifluoromethyl)sulfonyl imide ([MOIM][Tf ₂ N]).	17
Figure 3: Typical cyclic voltammogram and its typical parameters (i_{pc} , i_{pa} , E_{pa} , E_{pc}).	19
Figure 4: The cyclic voltammograms of an electroactive thin layer and monolayer.	22
Figure 5: Typical impedance plots for a simple electrochemical system: (a) reversible, (b) quasi-reversible, and (c) irreversible.	24
Figure 6: The Randles cell.	25
Figure 7: The impedance spectra exhibited by electrochemical systems which can be modelled by the Randle's cell.	28
Figure 8: (a) A ZARC with depressed semi-circle; (b) Warburg short-circuit terminus; (c) finite length Warburg-open circuit [89].	30
Figure 9: Equivalent circuit for a system in which the Warburg impedance is unimportant.	31
Figure 10: Impedance spectrum of a thin film of a reversibly electroactive material [93].	31
Figure 11: Background CVs of PCPE (black), ILPCPE (red), and ILCPE (green) in aq. KCl.	39
Figure 12: CVs of Fe(CN) ₆ ^{3-/4-} at (a) PCPE and (b) ILPCPE in aq. KCl (0.1 M) solution.	40
Figure 13: CV of H ₂ O ₂ and at (a) PCPE, (b) ILPCPE, and (c) ILCPE. Black = 0 mM. Red = 10 mM H ₂ O ₂ .	41
Figure 14: SEM images of (a) Graphite, (b) PCPE, (c) ILPCPE, and (d) ILCPE.	42
Figure 15: Cyclic voltammograms of hexacyanoferrate(III) at different scan rates in aq. KCl (0.1 M) solution, a) PCPE, b) ILPCPE and c) ILCPE.	44
Figure 16. Dependence of E_{pa} , E_{pc} , ΔE_p , i_{pa}/i_{pc} ratio on scan rate for CVs of Fe(CN) ₆ ³⁻ (4 mM) at three CP electrodes in aq. KCl (0.1 M) solution.	45

Figure 17: Impedance spectra (Bode Plots) in aq. KCl (0.1 M) solution in the presence of $\text{Fe}(\text{CN})_6^{3-/4-}$ (8 mM; 1:1), $E_{ac} = 0.010$ V, $E_{dc} = 0.2$ V (for PCP & ILPCP) or 0.17 V (ILCP).	47
Figure 18: Generalised equivalent circuit models for: (a) PCP and (b) ILCP and ILPCP in the presence of a redox active substance.	48
Figure 19: CVs recorded for PCPE (a) and ILPCP (b) in the presence of Fe^{2+} solution in aq. KCl (0.1 M) solution. Curve in red: 0 mM Fe^{2+} . Curve in black: 10 mM Fe^{2+} .	51
Figure 20: CVs recorded for PCPE (a) and ILPCP (b) in the presence of Co^{2+} in aq. KCl (0.1 M) solution. Curve in red: 0 mM Co^{2+} solution. Curve in black: 10 mM Co^{2+} solution.	52
Figure 21: CVs recorded for PCPE (a) and ILPCP (b) in the presence of Cu^{2+} in aq. KCl (0.1 M) solution. Curve in red: 0 mM Cu^{2+} solution. Curve in black: 10 mM Cu^{2+} solution.	53
Figure 22: CVs recorded for PCPE (a) and ILPCP (b) in the presence of Ce^{4+} in aq. KCl (0.1 M) solution. Curve in red: 0 mM Ce^{4+} solution. Curve in black: 10 mM Ce^{4+} solution.	54
Figure 23: CVs recorded for PCPE (a) and ILPCP (b) in the presence of Mn^{2+} in aq. KCl (0.1 M) solution. Curve in red: 0 mM Mn^{2+} solution. Curve in black: 10 mM Mn^{2+} solution.	55
Figure 24: CVs recorded before and after Fe^{2+} -electrodeposition at (a) PCPE & (b) ILPCPE	56
Figure 25: CVs recorded before and after Co^{2+} -electrodeposition at (a) PCPE & (b) ILPCPE	58
Figure 26: CVs recorded before and after Cu^{2+} -electrodeposition at (a) PCPE & (b) ILPCPE	59

Figure 27: CVs recorded before and after Ce^{2+} -electrodeposition at (a) PCPE & (b) ILPCPE	60
Figure 28: CVs before and after Fe^{2+} -electrodeposition at (a) PCPE & (b) ILPCPE.....	61
Figure 29: CVs of H_2O_2 at (a) PCPE/ Fe_xO_y and (b) ILPCPE/ Fe_xO_y in aq. KCl.....	63
Figure 30: CVs of H_2O_2 at (a) PCPE/ Fe_xO_y and (b) ILPCPE/ Fe_xO_y in aq. KCl.....	64
Figure 31: CVs of H_2O_2 at (a) “PCPE/ Fe_xO_y “ and (b) “ILPCPE/ Fe_xO_y “ in aq. KCl	65
Figure 32: CVs of H_2O_2 at (a) “PCPE/ Ce_xO_y “ and (b) “ILPCPE/ Ce_xO_y “ in aq. KCl (0.1 M) solution.....	66
Figure 33: CVs of H_2O_2 at (a) PCPE/ Mn_xO_y and b) ILPCPE/ Mn_xO_y	67
Figure 34: Multi-cycle CVs of Mn^{2+} at (a) PCPE, (b) ILPCPE, and (c) ILCPE in aq. KCl (0.1 M) solution.....	69
Figure 35: Multi-cycle CVs of Mn^{2+} at (a) PCPE, (b) ILPCPE, and (c) ILCPE in aq. NaCl (0.1 M) solution.	70
Figure 36: Multi-cycle CVs of Mn^{2+} at (a) PCPE, (b) ILPCPE, and (c) ILCPE in aq. KNO_3 (0.1 M) solution.	71
Figure 37: Multi-cycle CVs of Mn^{2+} at (a) PCPE, (b) ILPCPE, and (c) ILCPE in aq. LiCl (0.1 M) solution.....	72
Figure 38: Multi-cyle CVs of Mn^{2+} at (a) PCPE, (b) ILPCPE, and (c) ILCPE in aq. NH_4Cl (0.1 M) solution.	73
Figure 39: Multi-cyle CVs of Mn^{2+} at (a) PCPE, (b) ILPCPE, and (c) ILCPE in aq. NaOAc (0.1 M) solution.	74
Figure 40: Multi-cyle CVs of Mn^{2+} at (a) PCPE, (b) ILPCPE, and (c) ILCPE in aq. $NaClO_3$ (0.1 M) solution.	75
Figure 41: CVs of (a) PCPE/ Mn_xO_y , (b) ILPCPE/ Mn_xO_y , and (c) ILCPE/ Mn_xO_y in aq. KCl (0.1 M) solution.	77

Figure 42: CVs of (a) PCPE/Mn _x O _y , (b) ILPCPE/Mn _x O _y , and (c) ILCPE/Mn _x O _y in aq. NaCl (0.1 M) solution.	78
Figure 43: CVs of (a) PCPE/Mn _x O _y , (b) ILPCPE/Mn _x O _y , and (c) ILCPE/Mn _x O _y in aq. KNO ₃ (0.1 M) solution.	80
Figure 44: CVs CVs of (a) PCPE/Mn _x O _y , (b) ILPCPE/Mn _x O _y , and (c) ILCPE/Mn _x O _y in aq. LiCl (0.1 M) solution.	81
Figure 45: CVs CVs of (a) PCPE/Mn _x O _y , (b) ILPCPE/Mn _x O _y , and (c) ILCPE/Mn _x O _y in aq. NH ₄ Cl(0.1 M) solution.....	83
Figure 46: CVs of (a) PCPE/Mn _x O _y , (b) ILPCPE/Mn _x O _y , and (c) ILCPE/Mn _x O _y in aq. NaOAc (0.1 M) solution.	84
Figure 47: CVs CVs of (a) PCPE/Mn _x O _y , (b) ILPCPE/Mn _x O _y , and (c) ILCPE/Mn _x O _y in aq. NaClO ₃ (0.1 M) solution.....	86
Figure 48: ATR-FTIR Spectra of the paraffin oil (P), ionic liquid (IL), and their 1:1 (v/v) mixture (P+IL)	89
Figure 49: ATR-FTIR spectra of graphite powder, PCPE, ILPCPE, and ILCPE.	91
Figure 50: ATR-FTIR spectra PCPE/ Mn _x O _y , ILPCPE/ Mn _x O _y , and ILCPE/ Mn _x O _y prepared in aq. KCl (0.1 M) solution. The spectra of the CPEs before electrodeposition are also shown overlaid.	92
Figure 51: SEM images of surface samples of PCPE (a & a'), ILPCPE (b & b'), & ILCPE (c & c') after electrodeposition of Mn ²⁺ in aq. KNO ₃ (a, b, & c) and KCl solution (a', b' & c').....	94

LIST OF TABLES

Table 1: Classes of ionic liquids [62].	13
Table 2: A summary of some physico-chemical properties of ionic liquids at 25°C	16
Table 3: Electrode properties and $\text{Fe}(\text{CN})_6^{3-/4-}$ electrode-kinetics data based on CV analysis are shown.	46
Table 4: Equivalent circuit and kinetic parameters estimated using the EIS data (Figure 17) for PCPE, ILCPE, and ILPCP in $\text{Fe}(\text{CN})_6^{3-/4-}$ (8 mM)/ aq. KCl (0.1 M) solution.	49
Table 5: Values of E_{pa} , E_{pc} , and I_{pa} of Mn_xO_y films formed in aq. KCl (0.1 M) solution.	77
Table 6: Values of E_{pa} , E_{pc} , and I_{pa} of Mn_xO_y films formed in aq. NaCl as measured in fresh aq. NaCl (0.1 M) solution.	79
Table 7: Postdeposition E_{pa} , E_{pc} , and I_{pa} values of Mn_xO_y films in aq. KNO_3 (0.1 M) solution.	80
Table 8: Postdeposition E_{pa} , E_{pc} , and I_{pa} values of Mn_xO_y films aq. LiCl (0.1 M) solution.	82
Table 9: Postdeposition E_{pa} , E_{pc} , and I_{pa} values of Mn_xO_y films in aq. NH_4Cl (0.1 M) solution.	83
Table 10: Postdeposition E_{pa} , E_{pc} , and I_{pa} values of Mn_xO_y films in aq. NaOAc (0.1 M) solution.	85
Table 11: Postdeposition E_{pa} , E_{pc} , and I_{pa} values of Mn_xO_y films in aq. NaClO_3 (0.1 M) solution.	87

Page Left Blank



1. INTRODUCTION

Room temperature ionic liquids (RTILs or ILs), generally touted as environmentally green solvents, have been acknowledged to possess good chemical and thermal stability, excellent conductivity, and show good solvation of inorganic and organic substances [1]. In this dissertation, the author is interested in the application of RTILs as binders in carbon paste electrodes (CPEs) and electrodeposition of transition metal oxide (TMO) films. Transition metal oxides possess easily tune-able structure-property relationships and show high thermodynamic stability under ordinary conditions as may be learnt from their roles in metal-surface passivity [2]. These properties make them suitable for multifunctional component applications in chemical sensors, biosensors, and other technological devices [3, 4].

Most previous studies were made with solid electrodes (mostly – glassy carbon electrodes), which were film modified with TMOs or screen printed carbon electrodes (SPCEs) and normal CPEs bulk-modified with TMOs. Some reports with ILs as binders in CPEs are also available. Current work deals with the effect of incorporating the hydrophobic IL 1-methyl-3-octylimidazolium bis(trifluoromethyl)sulfonyl imide into a CPE on electrode properties, electrochemistry of redox probes ($\text{Fe}(\text{CN})_6^{3-/4-}$, H_2O_2), electrodeposition of TMO oxide films from aqueous solutions of Fe^{2+} , Mn^{2+} , Co^{2+} , Cu^{2+} , and Ce^{2+} ions study of the electrochemistry. In addition to the ease of their bulk-modification, working with CPEs is convenient as their surfaces can be renewed by simple single-step polishing on an ordinary filter paper [5, 6].

This dissertation is presented in seven sections including the introduction. Section 2, a brief account of literature on CPEs, TMO – modified CPEs, and RTILs are given. Section 3 briefly describes the principles of selected analytical techniques. Section 4 is the experimental part.

Section 5 is on results and discussion. Section 6 presents conclusions. Section 7 is the Bibliography.



2. LITERATURE

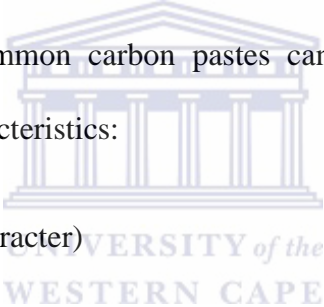
2.1 Carbon Paste Electrodes (CPEs)

CPEs are electrode materials with a wide range of promising electrochemical applications [7, 8]. Adams [2009] was the first to issue a report in which he introduced this kind of electrode, originally designed as an alternative to the dropping mercury electrode and primarily focused on the characterization of CPEs with respect to their applicability in anodic and cathodic voltammetry [9]. Even though the dynamic renewable concept was unsuccessful, it turned out that the material with paste-like consistency could be practically employed in voltammetric analysis [10]. CPE made from carbon particles and inorganic liquid comprising numerous test measurements and has been the most popular electrode materials used in the laboratory preparations of different electrodes, sensors and detectors [11]. CPEs, the most common representative of heterogeneous carbon materials, have been used as electrochemical sensors and biosensors because they are available in different forms, low cost, wide potential window, low background current, chemically inertness, ease of chemical derivatisation and modifications and their suitability for various applications [1]. However, CPEs also exhibit weaker fabrication reproducibility and mechanical stability comparing with the bare solid electrodes, which greatly limit the practical utility for enzymatic assays and probes [12].

Heterogeneous electrodes in general are electrochemical sensors composed not only of one uniform substance, but also consist of electrically conductive embedded material. CPEs are an example of the more general class of the composite electrodes, in which chemically useful functionalities can be introduced during physical mixing of graphite and pasting liquids. The lifetime of carbon paste electrodes is closely connected to the quality of the binder and sometimes to the carbon-to-pasting liquid ratio.

These electrodes are classified as bare or unmodified carbon electrodes. Other carbonaceous materials aside from carbon are used on rare occasions, such as charcoal, soot [13], carbon microspheres and foam [11], carbon nanotubes [14], and even powdered diamonds [15]. Paste electrodes contain a liquid binder, which is usually an electric insulator, such as paraffin oil, silicone oil, bromonaphthalene, and esters such as organophosphates and phthalates.

For special studies electrolytic components may also be used [16, 17]. As a matter of fact, paste-like materials are exclusively used as bulk electrodes. The ratio of liquid binder to particulate matter may vary from 0.3 ml per gram for dry to over 1 ml per g for wet pastes. The material may be put into simple holders, cut-off pipette tips, or piston-driven devices. The nature and behavior of common carbon pastes can be portrayed by means of the following physico-chemical characteristics:

- 
- *Heterogeneity* (composite character)
 - *Lipophilia* (hydrophobicity)
 - *Low ohmic resistance* (high conductivity)
 - *Instability* in non-aqueous solutions (disintegration)
 - *Ageing* effects (limited life-time)

These properties are closely connected with a specific microstructure of carbon pastes. Recently, some newly made real images of the carbon paste microstructure have been presented based on scanning electron- and optical microscopic observations [18]. The images have confirmed the conclusion of the previous studies that carbon pastes represent mixtures with rather unconsolidated structure where the graphite particles are practically covered with

a very thin film of the binder. Nevertheless, the individual graphite particles are apparently in some physical contact beneath the binder layer, which may explain a very low ohmic resistance of most carbon pastes (varying in ohms, max. in tens of ohms). Alternative interpretation of their surprisingly high conductivity can be due to a “tunnel effect” similar to that known for semiconductors.

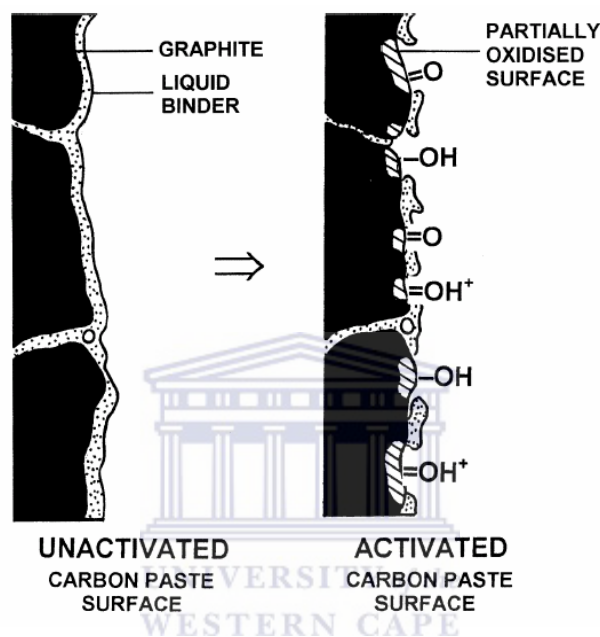


Figure 1: Microscopic model of plain CPE surface [17].

Amongst different carbon-based electrodes available for the development of electrochemical sensors and biosensors, CPEs because they are renewable, versatile, controlled bulk modification, easily fabricated, low background and a renewable surface, the CPE has been widely applied in the electro-analytical community [1, 17]. Therefore, the CPE can provide a suitable electrode substrate for preparation of modified electrodes. However, the electron transfer rates observed at carbon surfaces are often slower than those observed on noble metal electrodes. Electron transfer reactivity is strongly affected by the origin and history of the carbon surface. These electrodes are represented by carbon paste which is done by mixing graphite powder and paraffin oil (binder) and packed into a hydrophobic plastic tube-tip with

an electrical contact. Generally, the organic liquid as binder component of the pastes is a non-conductive mineral oil, such as Nujol®, paraffin or alike. This non-conductive viscous liquid is always favored in the process of fabricating the traditional CPE because it is chemically inert and has a good adhesive ability [19]. Figure 1 illustrates an artist's view of the microscopic structure of a carbon paste electrode.

The choice of carbon paste components, their quality and mutual ratio in the mixture as well as the way of preparation of carbon pastes and their most favorable homogenization determine the performance of a CPE. Due to a number of advantageous properties and characteristics, these electrodes are still popular and are mainly used in voltammetric measurements and have been the most commonly studied or used electrodes in the development of chemical sensors obtainable at a very low cost; however, carbon paste-based sensors can also be applied in amperometry [20], coulometry [21], and potentiometry [22]. These electrodes can be highly selective for both organic and inorganic. Carbon Paste electrodes (CPEs) can also display some disadvantages by reproducing a weaker fabrication and mechanical stability compared to solid electrodes [5] and also the success in working with carbon paste-base electrodes depends very significantly upon experimental experience of the user. Electrochemical properties of different types of CPEs can be predicted only approximately and their more detailed characterization needs appropriate testing measurements [22].

Physico-chemical properties of carbon pastes are always mirrored in the overall electrochemical behavior of CPEs, which results in some special features and benefits, such as, very low background currents (favorable signal-to-noise ratio), individual polarisability (with variable potential window), specific reaction kinetics (affected by both carbon paste constituents), electrode activity at the carbon paste surface as well as in the carbon paste

bulk, variability in utilizing various interactions and their synergistic effects at both CPEs and chemically modified carbon paste electrodes, CMCPE (electrolysis, catalysis, adsorption, extraction, ion-pairing, and their combination) and various alternative procedures for pre-treating, conditioning and regenerating the electrode surface and carbon paste [23]. CPEs also exhibit several disadvantages such as relative weaker fabrication reproducibility and mechanical stability comparing with the bare solid electrodes, which greatly limit the practical utility of enzymatic assays and probes [24].

2.2 Multivalent Metal Oxide – Modified CPEs

Multivalent metal oxides are interesting materials because of the wide spectrum of structure properties they exhibit and they are thermodynamically stable, are easily and economically available [17, 22, 25]. Metal oxides have attracted attention of researchers due to their optical, electrical, magnetic, mechanical and catalytic properties, which makes them useful in technology [26] and development of electrochemical [3, 27]. Brief background information on iron oxide and manganese oxide is given below. The literature on iron oxide was largely based on an unpublished manuscript by Waryo et al. [28].

As the chemistry of iron oxides is rather diverse, most of the following discussions focus only on Fe_3O_4 with an objective to provide a background for its potential electrocatalytic applications. Some topics are based on online knowledge/ information sources [29]. Especially the web site sustained by Grygar [2002] and generally dedicated to electrochemistry of metal oxides and hydroxides in aqueous environment provides a critical review (until April 2002) of descriptive stuff worth reading before embarking on an electro-analytical study connected with these substances. Fe_3O_4 (CAS # 1309-38-2) is known by several synonyms like magnetite, black iron oxide, magnetic iron ore, lodestone, ferro ferrite,

or ferrous ferric oxide. It is the earliest discovered magnet (~1500 B.C.) and one of the most abundant transition metal oxides [30].

The crystal structure of magnetite, denoted as $\text{Fe}^{3+}[\text{Fe}^{2+}\text{Fe}^{3+}]\text{O}_4$, is an inverse spinel type in which the Fe^{2+} ions go into octahedral sites displacing half the Fe^{3+} ions into the tetrahedral positions [31]. This arrangement causes a transfer of electrons between the different irons in a structured path or vector. This electric vector generates a magnetic field. The stacking of Fe and O ion layers with opposite charges also gives rise to a large dipole moment perpendicular to the surface. Fe_3O_4 is also described as a half-metal: only electrons of one spin direction are responsible for its metallic conductivity; those of opposite spin are insulating [32]. Magnetite is an important ore of iron with applications which include magnetic properties, pigment, magnetic inks, light metals casting, heat storage, functional polymer filler, media recording, ballast, brick/ refractory, catalysts, cement, ceramic, coal, coloring, radiation shielding, smelting, and water treatment to mention a few. Thus synthesis and production of magnetite is of wide commercial and scientific interest.

Chemical methods for bulk synthesis of magnetite include co-precipitation of both iron (II) and iron (III) salts in alkaline aqueous solution, oxidation of iron(II)-hydroxide with alkaline nitrate or oxygen, or reduction, at high temperature, of $\gamma\text{-Fe}_2\text{O}_3$ by means of a CO/CO_2 or a hydrogen gas flow, hydrothermally from $(\text{NH}_4)_2\text{SO}_4 \cdot \text{FeSO}_4 \cdot 6\text{H}_2\text{O}$ in the presence of hydrazine [33-35]. Recently, “mechanochemical” redox process of producing magnetite was proposed in which $\gamma\text{-Fe}_3\text{O}_4$ powder is synthesized by simple planetary milling of a mixture of metallic Fe and $\text{FeO}(\text{OH})$ (1:2) in H_2O_2 containing acetone [36]. An even totally dry method involves mechanical alloying in an inert atmosphere of a stoichiometric mixture of micrometric iron and hematite powders which would give nanocrystalline magnetite [37].

However, in sensing applications, more interesting and fascinating are methods of synthesis suitable for in-situ deposition of magnetite and others.

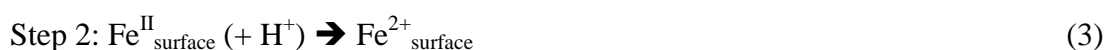
Unlike the other oxides of iron, magnetite lends itself to a direct study as a bulk electrode, yields several electrochemical reactions and is the best starting point to learn more about electrochemistry of Fe oxides [29]. The other polymorphs of iron oxide have much lower bulk electric conductivity than Fe₃O₄, and therefore need to be studied in carbon paste [38-41] or by micro-particle voltammetry (abrasive stripping voltammetry) [42, 43]. Fe₃O₄ and different polymorphs of Fe₂O₃ and FeOOH behave electrochemically differently [44]. However, the phenomena of electro-reductive dissolution of Fe(III) oxides [29] and oxygen insertion into metal-substituted Fe-oxides (electrochemical solid-to-solid oxidation) [45] have been generally observed. The electrochemical properties of iron oxides are mainly controlled by two factors, viz., the phase composition and substitution of Fe by other metals [29]. The most important phases are Fe₃O₄, Fe₂O₃ (hematite and maghemite), FeOOH (goethite, lepidocrocite, and few others), spinels such as MeFe₂O₄, and perovskites such as SrFeO₃. The most common metals substituting Fe are Al and Cr. The dissolution of magnetite was investigated using compact electrodes [46, 47]. The electrochemistry of magnetite involves reductive dissolution, reduction to metallic iron, hydrogen evolution, and the reduction of possible dissolved oxygen. The direct electrochemical oxidation or oxidative dissolution of bulk magnetite to ferric products is hardly possible [48]. The same is valid for spinels with Fe(II) [49] studied in carbon paste. Normal reductive dissolution proceeds in acidic solution and yields soluble ferrous ions:



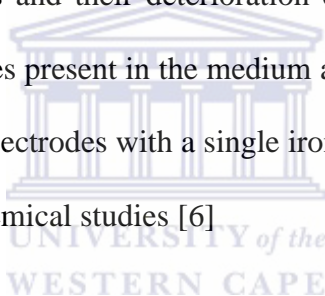
This reaction is a sequence of three steps (equations 2 to 4): 1) redox reaction of Fe in the crystal lattice (electrochemical reaction); 2) conversion of Fe(II) in the lattice to Fe²⁺ by

protonation and hydration (chemical reaction); and 3) detachment of Fe^{2+} and its transport through the diffuse layer around the oxide (Coulomb forces and transport mechanisms) [29].

While step 1 is rate determining at more positive potentials, step 3 is so at more negative potentials.



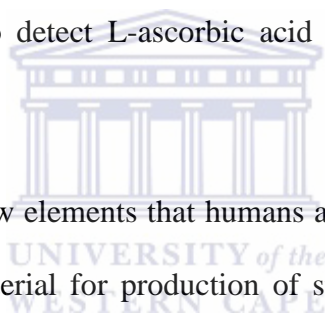
Fe_3O_4 is said to be good materials for data storage and transmission. Materials containing iron are widely used in various fields and their deterioration due to corrosion is a well-known problem. Depending on the species present in the medium a variety of corrosion products can be formed. The development of electrodes with a single iron corrosion product presents many advantages to carry out electrochemical studies [6]



Magnetite has natural magnetic properties that provide a large number of uses in the industry. The quality of magnetite used has been particularly important to the magnetic recording industry. With the demand for smaller and lighter-weight magnetic recording devices, there has been an increasing need for recording media (such as magnetic recording tape and magnetic disks, for example) to have a higher recording density and sensitivity. In order to meet these demands, the magnetite particles produced would desirably have a smaller particle size with a higher coercive force [33].

In the field of biotechnology and bio-analytical chemistry, manganese dioxide is an important functional material and has been used as a mediator to fabricate chemical sensors and biosensors [50]. Manganese dioxide (MnO_2) has been proven to be an appropriate mediating or catalytic substance to lower the over-potential for H_2O_2 oxidation. Wang [2007] prepared a

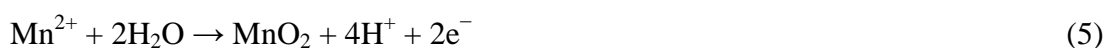
GCE with a film of MnO₂ deposited from MnCl₂/NaOH solution and showed that it could be used in strongly alkaline solution [1]. Schachl's research group reported a CPE modified with commercially available manganese dioxide and used for H₂O₂ detection in connection flow-injection analysis [50] and achieved a detection limit of 1.3×10^{-6} M for H₂O₂ using a CPE modified by bulk MnO₂ powder [51]. In addition, they covered the electrode with a layer of glucose oxidase and measured glucose in beer and wine. Recently, the development of sensors and biosensors based on heterogeneous carbon electrodes modified with manganese dioxide has been reviewed by [52]. On the basis of the special reaction capability of MnO₂ nanoparticles with H₂O₂, a glucose biosensor has been fabricated by co-immobilizing GOx and MnO₂ nanoparticles on the gate of an ion-sensitive field effect transistor. MnO₂ nanoparticles have also been used to detect L-ascorbic acid with an ion-sensitive field effect transistor [53].



Manganese (Mn) is one of the few elements that humans and industries use on a daily basis. Mn ore is an important raw material for production of steel, ferromanganese, non-ferrous alloys, dry cell batteries, paints and other chemicals. The different needs of manganese have therefore caused a great deal of attention to be devoted to improve recovery from its ore and slags. Beneficiation of low-grade manganese ores is an area of hydrometallurgy that has been extensively studied. Manganese is an important metal in human life and industry. In recent years, the world manganese demand has been driven by towering steel production, particularly in China. Steelmaking, including its iron making component, has accounted for most of the world manganese consumption, presently in the range of 85% to 90% of the total demand [54]. It is an essential micronutrient for all organisms but at high concentrations can be toxic, contributing for example to the early development of Parkinson's disease symptoms in susceptible people. Manganese toxicity is also a serious constraint to crop cultivation since manganese is taken-up by plants and can easily be passed into the food chain again causing

symptoms of Parkinson's disease [55]. The biological importance of manganese has been well known for a long time. As a microelement of great relevance, it is responsible for a variety of cell activities, being intimately involved in certain biochemical pathways [56]. Manganese oxides are of considerable interest, and they have been widely used as catalyst, ion-exchanger, solid ionic conductor, and battery materials [57].

When carbon based electrode materials are used, cathodic stripping voltammetry is a sensitive and selective technique. Manganese can be oxidized on an electrode surface forming insoluble manganese (IV) dioxide according to the equation below:




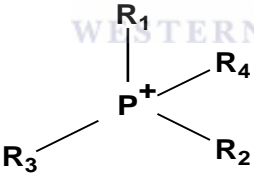
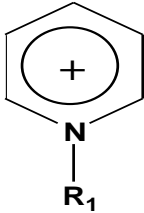
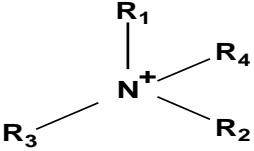
The biological importance of manganese has been well known for a long time. As a microelement of great relevance, it is responsible for a variety of cell activities being intimately involved in certain biochemical pathways.

2.3 Room Temperature Ionic Liquids (RTILs)

Room temperature ionic liquids (RTILs) are ionic compounds that consist of organic cations and different kinds of anions, which are liquid at room temperature. These are salts having low melting points so they can act as solvents in which reaction can be performed, since ionic liquids are made of ions rather than molecules such reactions give distinct selectivities and reactivity compared to organic solvents. RTILs have chemical properties such as high thermal stability, high ionic conductive, vapor pressure negligibility and as well having a wider electrochemical windows [58]. These ionic liquids have been proposed to be very interesting and efficient pasting binders in replacement of non-conductive organic binders for preparation of carbon ionic liquid electrodes (CILEs) [59].

Over a couple of years, a considerable number of studies have been made on the syntheses and application of room temperature ionic liquids (RTILs or ILs), sometimes called room temperature molten salts in the liquid state [55, 60]. RTILs usually consist of an organic cation (such as N-alkyl-methylimidazolium, N-alkyl-methylpyridinium group, etc.) and inorganic anions (such as, halogen anion, tetrafluoroborate, hexafluorophosphate, etc.). A high degree of asymmetry in these organic salts frustrates the molecular packing thus inhibiting crystallization, and rendering a broad liquids temperature range [61]. Well known classes of cations and anions that form in ILs are summarized in Table 1.

Table 1: Classes of ionic liquids [62].

Class name	Cations	Anions	Reference
Imidazolium		[Cl ⁻], [Br ⁻], [BF ₄ ⁻], [Tf ₂ N ⁻]	[60, 63]
Tertra alkylphosphonium		[PF ₆ ⁻], [CF ₃ SO ₃ ⁻],	[61, 64]
Pyridinium		[NO ₃ ⁻], [AlCl ₄ ⁻]	[65, 66]
Quaternary ammonium		[AlBr ₄ ⁻], [(CF ₃ SO ₂) ₂ N ⁻]	[67, 68]

RTILs have fascinating properties which makes them fundamental to chemist, such as non-volatility, non-flammability, high ionic conductivity and wide liquid-state temperature range.

The chemistry is different and unpredictable at our current state of knowledge because both the thermodynamics and kinetics of reactions carried out in ionic liquids are different to those in the conventional molecular solvents [66]. ILs also have unique physical and chemical properties including ionic conductivity, amphiphilicity and catalytic functions. All these characteristics project ILs as a potential alternative medium for many organic reactions [68]. Interestingly, RTILs are also applied as safe electrolytes for electrochemical devices in this field in addition to the use as reaction media for organic syntheses [65].

The low melting point of ILs can be ascribed to the asymmetry in molecular structures, which largely lowers the packing efficiency and inhibits crystallization. Large sizes of anions can also contribute to the low melting point. The non-volatility and thermal stability of ILs result from the strong ionic interactions, hydrogen bonding, and sometimes relatively strong hetero-carbon interactions [61]. The amphiphilicity of ILs originates from molecular structures typically consisting of two incompatible parts in one molecule, i.e. hydrophobic group and hydrophilic group. The amphiphilic property of an IL is endowed with low surface tension [69], self-aggregation behavior in water [70], and, for an ILs with long alkyl chains, the ability to form a liquid crystal phase. RTILs, generally touted as environmentally green solvents for the electro-deposition of metals, alloys and semiconductors, especially for very active elements because hydrogen evolution can be avoided and also been acknowledged to possess good chemical and thermal stability, excellent conductivity, and show good solvation of inorganic and organic [1, 71]. Due to the amphiphilic nature, IL molecules can self-aggregate similarly to common ionic surfactants. Bowers [2004], reported the self-aggregation behavior exhibited by the ILs in aqueous solutions by measuring surface tension, conductivity, and by small-angle neutron scattering (SANS). However, the information about the self-aggregation behavior of ILs in the presence of other organic solvents is still lacking. Ionic liquids are complex fluids compared to normal simple fluids, due to the strong

Colombic interactions and other intermolecular interactions. These interactions result in extended correlations in IL, as well as slower translational and rotational mobility [72]. The strong interactions, complicated structures, and low mobility may easily lead to a glassy state after the temperature is lowered. Due to the features mentioned above, ILs have found their applications in various types of organic reactions as catalysts, for example, Diels-Alder reaction [73], Friedel-Crafts reaction [74], and polymerization [4], etc. Other applications include nanostructured material fabrication [68], separation and extraction [63], biotechnology [75] and electrochemistry [76].

In some contexts, the term has been restricted to salts whose melting point is below some arbitrary temperature, such as 100 °C (212 °F). While ordinary liquids such as water and gasoline are predominantly made of electrically neutral molecules, ILs are largely made of ions and short-lived ion pairs. These substances are variously called liquid electrolytes, ionic melts, ionic fluids, fused salts, liquid salts, or ionic glasses. RTILs are novel solvents with favorable environmental and technical features. Synthetic routes to over 200 RTILs are known but for most ionic liquids physicochemical data are generally lacking or incomplete. Ionic liquids are simply liquids composed entirely of ions. They have garnered increasing interest in the last few years as novel solvents for synthesis, separations, electrochemistry and process chemistry [65, 77]. An important discipline of science that benefits from the use of RTILs is electrochemistry. From an electrochemical point of view, RTILs open a field of new solvents with high conductance (additives not needed) and an extended electrochemical window combined with high stability. The most important reason is that ionic liquids negligible vapour pressure and hence they do not evaporate to environment [66]. This is because RTILs have a number of desirable characteristics, including negligible volatility, non-flammability, high thermal stability, low melting point, and controlled miscibility with organic compounds, especially some heterocyclic compounds. RTILs are non-symmetrical

and large organic cationic liquids of imidazolium, pyrrolidinium, fluorophosphate, fluoroborate, tosylate or glycolate origin. Most recently, it is found that the ionic liquids alkyimidazolium tetrafluoroborates were a kind of versatile lubricants for the contact of steel/steel, steel/aluminum, steel/copper, steel/SiO₂, Si₃N₄/SiO₂, steel/Si (100), steel/sialon ceramics, and Si₃N₄/sialon ceramics [78, 79]. McEwen et al. [61] found that alkyimidazolium-bis (trifluoromethylsulfonyl)-imide salts showed better thermal stability than alkyimidazolium tetrafluoroborate salts.

Table 2: A summary of some physico-chemical properties of ionic liquids at 25°C

Ionic Liquid	Density / g cm ⁻³	Viscosity / cP	Conductivity / mS cm ⁻¹
[BMIM][BF ₄]	1.12	1.7	233
[BMIM][PF ₆]	1.368	450	N/A
[BMIM][Tf ₂ N]	1.436	52	N/A
[BMIM] I	1.44	110	N/A
[BMIM][TfO]	1.29	90	3.7
[BMIM][CF ₃ CO ₂ H]	1.21	73	3.2
[OMIM][PF ₆]	1.237	682	N/A
[EMIM][Tf ₂ N]	1.519	28	N/A
[EMIM][NMs ₂]	1.343	787	1.7
[EM2IM][Tf ₂ N]	1.51	88	3.2
[OMIM][Tf ₂ N]	1.320		N/A
[OMIM]Cl	1.00	337	N/A

Their physicochemical properties are the same as high temperature ionic liquids, but the practical aspects of their maintenance or handling are different enough to merit a distinction. These properties of ionic can be dramatically altered by impurities such as water, organic

solvents and chloride ions. Hence, precautions need to be taken when synthesizing ionic liquids to avoid such impurities. Physico-chemical properties and solvent properties for some ionic liquids are listed in Table 2. Room temperature ionic liquid of interest in the current study is 1-methyl-3-octylimidazolium bis(trifluoromethylsulfonyl) imide [MOIM][Tf₂N] which is given in Figure 2. [MOIM][Tf₂N] (see Figure 2) is a hydrophobic ionic liquid with a density of 1.33 g/mL and twice as viscous (90.80 mm²/s) as the mineral oil paraffin (density = 0.827-0890 g/mL). The ionic conductivity of [MOIM][Tf₂N] has been estimated as 1.6 mS cm⁻¹.

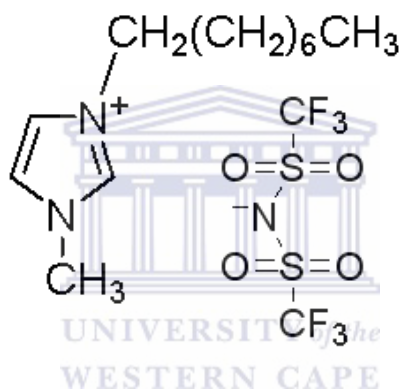


Figure 2: Molecular structure of the hydrophobic room temperature ionic 1-methyl-3-octylimidazolium bis(trifluoromethylsulfonyl) imide ([MOIM][Tf₂N]).

2.4 RTILs/CPEs as Electrodes

Since the first report of Adams [2009], the carbon paste electrodes (CPEs) have been used for a large number of electro-analytical applications, mostly including the developments for the quantification of hydrogen peroxide [80]. CPEs attracted a lot of interest, this might be due to improved renewability stable response and a low ohmic resistance of CPEs compared to membranes electrode or as ion selective electrodes. CPEs are ideally suited for preparation of bulk-modified-electrodes by incorporation of reactive materials, for example into a mixture of graphite powder dispersed in a non-conductive mineral oil [81]. The mineral oil

component in the carbon paste causes disadvantages of the resulting CPEs, the major one is caused by the preparation process of the oils. Typical parameters required for pasting liquids are: i) chemical inertness and electro-inactivity, ii) high viscosity and low volatility, and iii) minimal solubility in aqueous solutions. Thus, the commonly used pasting liquids for the preparation of CP were mainly organic mineral oils (e.g. Nujol®, paraffin) [24]. Mineral oils have unpredictable components due to the fact that these compounds are prepared during refining of petroleum and processing of crude oil, which can influence the detection characteristics of the resulting CPEs. In contrast, IL as mentioned earlier, possess good solvating properties, high conductivity, non-volatility, low toxicity, good electrochemical and chemical stability, low vapor pressure, low toxicity, and high ionic conductivity [59]. Thus, recently, ILs have received much attention in different areas including bio-catalytic processes. CPEs prepared with imidazolium-based ionic liquids exhibited increased sensitivity of response towards potassium ferricyanide [78], Even though the replacement of the paraffin oil causes a very high back ground current, advantages over normal CPEs include high conductivity, fast electron transfer, good thermal and chemical stability of inorganic and organic substances.

3 PRINCIPLES OF SELECTED ANALYTICAL METHODS

3.1 Cyclic Voltammetry (CV)

Cyclic voltammetry is used for study of redox processes rather than quantification; understand reaction intermediates and obtaining stability of reaction products [82]. The current at the working electrode is plotted versus the potential difference between the working electrode and a reference electrode. During the experiment the potential is ramped linearly versus time, when the cyclic voltammogram reaches a set potential, the working electrode ramp is inverted. This technique is based on varying potential at the working electrode in both the forward and reversible directions at some scan rate while monitoring current. The important parameters are the peak potentials (E_{pa} , E_{pc}) and peak currents (I_{pa} , I_{pc}) of the anodic and cathodic peaks [82].

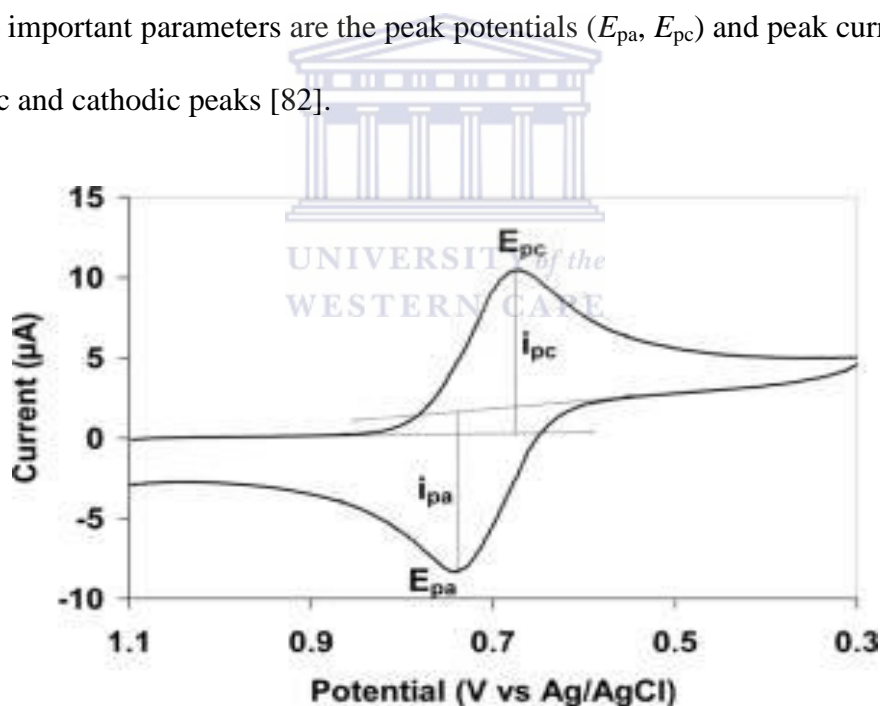


Figure 3: Typical cyclic voltammogram and its typical parameters (i_{pc} , i_{pa} , E_{pa} , E_{pc}).

For a simple heterogeneous electron transfer reaction ($Ox + ne^- \rightarrow Red$) involving n ($=1$ or 2) electrons, if the electroactive reactant (Ox) is dissolved in an electrolyte solution of sufficient conductivity and the electrochemical reaction is not extensive enough to alter the composition

of the bulk of the electrolyte, the product (Red) is stable and also soluble in the electrolyte, the following relations apply.

Reversible electrode reaction:

$$\Delta E_p = E_{pa} - E_{pc} = 2.3 \frac{RT}{nF} \approx \frac{0.058}{n} \text{ V at } 25^\circ \text{ C} \quad (6)$$

$$i_{p,c} = 0.4463nFA \left[\frac{nF}{RT} \right]^{1/2} C_{Ox}^{bulk} D_{Ox}^{1/2} \nu^{1/2} \quad (7)$$

$$i_{p,a} = 0.4463nFA \left[\frac{nF}{RT} \right]^{1/2} C_{Red}^{bulk} D_{Red}^{1/2} \nu^{1/2} \quad (8)$$

E_{pa} : constant regardless of scan rate

E_{pc} : constant regardless of scan rate

Where A – area of electrode (cm^2), D_{Ox} or D_{Red} – diffusion coefficients ($\text{cm}^2 \text{ s}^{-1}$), C^{bulk} – bulk concentrations (in mol cm^{-3}), ν - scan rate (V s^{-1}), $R = 8.314 \text{ J K}^{-1} \text{ mol}^{-1}$, T is temperature (K), and $F = 98485 \text{ C mol}^{-1}$.

For irreversible reactions:

$$\Delta E_p = E_{pa} - E_{pc} > 2.3 \frac{RT}{nF} = \frac{0.058}{n} \text{ V at } 25^\circ \text{ C} \quad (9)$$

$$\left| E_{p,c} - E_{p/2} \right| = \frac{1.86RT}{\alpha nF} = \frac{47.7}{\alpha n} \text{ mV at } 25^\circ \text{ C} \quad (10)$$

$$i_{p,c} = 0.4958 \times nF \times \left(\frac{\alpha nF}{RT} \right)^{1/2} A D_o^{1/2} \nu^{1/2} C_o^{bulk} \quad (11)$$

$$i_{p,a} = 0.4958 \times nF \times \left(\frac{(1-\alpha)nF}{RT} \right)^{1/2} AD_R^{1/2} \nu^{1/2} C_R^{bulk} \quad (12)$$

$$E_{p,c} = E^{o'} - \frac{RT}{\alpha nF} \left(0.780 + \frac{2.3}{2} \log \left(\frac{\alpha nF D_O}{RT (k^o)^2} \right) \right) - \frac{2.3RT}{2\alpha nF} \log \nu \quad (13)$$

$$E_{p,a} = E^{o'} + \frac{RT}{(1-\alpha)nF} \left(0.780 + \frac{2.3}{2} \log \left(\frac{(1-\alpha)nF D_R}{RT (k^o)^2} \right) \right) + \frac{2.3RT}{2(1-\alpha)nF} \log \nu \quad (14)$$

Where $E^{o'}$ is the formal potential, α is the electron transfer coefficient (dimensionless), k^o is the heterogeneous standard heterogeneous rate constant (cm s^{-1}). Provided reactant and product possess similar diffusion coefficients, the formal potential may be approximated as the mid-point of the two peak potentials or more accurately as per following equation:

$$E^{o'} = \alpha E_{p,c} + (1-\alpha) E_{p,a} \quad (15)$$

For a quasi-reversible reaction under the above experimental set-up,

$$\psi = \left(\frac{RT}{nF D_{Ox} \pi} \right)^{1/2} \left(\frac{D_{Ox}}{D_{Red}} \right)^{\alpha/2} k^o \nu^{-1/2} \quad (16)$$

Where ψ Nicholson's parameter with numerically calculated values as a function of $n \times \Delta E$ for each scan rate [83].

The cyclic voltammograms of an electroactive substance in a thick layer films immobilized on the surface of the electrode follows the same mathematical relations as above. Thin layer electro-active films, mono-layers or a few molecular layers for which diffusion is not necessary for reaction to occur, exhibit voltammograms of different shape and hence different current-potential relationships. For reversible electrode reaction in a thin film to which the reactant is confined, provided both reactant and product are insoluble in the interfacing

electrolyte medium, and if intermolecular interactions before and after reaction are the same, a typical voltammogram would look like as in Figure 4 [84]:

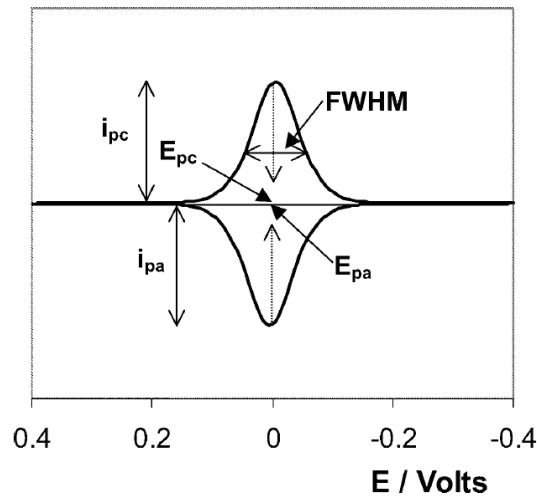


Figure 4: The cyclic voltammograms of an electroactive thin layer and monolayer

In such a case, the CV parameters, including the peak-shape or the full-width at half-maximum (FWHM), are given by the corresponding Equations 17 – 20.

$$i_{p,c} = -i_{p,a} = \frac{n^2 F^2}{4RT} \nu A \Gamma \quad (17)$$

$$\Gamma = \frac{Q}{nFA} \quad (18)$$

$$E_{p,c} = E_{p,a}, \text{ i.e. } \Delta E_p = 0 \text{ regardless of scan rate} \quad (19)$$

$$\text{FWHM} = 3.53 \frac{RT}{nF} = \frac{0.0906}{n} \text{ V at } 25^\circ \text{ C} \quad (20)$$

Where Γ is initial surface concentration of reactant (mol cm^{-2}), Q = charge passed during forward or reverse scan causing a complete electrolysis and conversion of the reactant into product.

For the electrode reaction of the reactant confined to the thin film is irreversible, we have the following current-potential relations [85].

$$i_{p,c} = \frac{\alpha n^2 F^2 \Gamma}{2.718RT} v \quad (21)$$

$$i_{p,a} = -\frac{(1-\alpha)n^2 F^2 \Gamma}{2.718RT} v \quad (22)$$

$$E_{p,c} = 2.3 \frac{RT}{\alpha nF} \log\left(\frac{RTk^o}{\alpha nFv}\right) \quad (23)$$

$$E_{p,a} = 2.3 \frac{RT}{(1-\alpha)nF} \log\left(\frac{RTk^o}{(1-\alpha)nFv}\right) \quad (24)$$

$$FWHM = \frac{0.0625}{\alpha n} \text{ V (cathodic)} \quad (25)$$

$$FWHM = \frac{0.0625}{(1-\alpha)n} \text{ V (anodic)} \quad (26)$$



3.2 Electrochemical Impedance Spectroscopy (EIS)

Electrochemical Impedance Spectroscopy (EIS) is a very powerful, rapid and accurate nondestructive method for the evaluation of the wide range of materials [86]. EIS has many advantages in comparison with other techniques. Recently, EIS or ac impedance has seen tremendous increase in popularity. EIS was initially applied to the determination of the double-layer capacitance and in ac polarography, they are now applied to the characterisation of the electrode processes and complex interfaces. In EIS studies, the system's impedimetric response to the application of a periodic small amplitude ac signal super-imposed over a constant dc potential is measured and analyzed. These measurements are carried out at

different ac frequencies to generate an impedance plot. In Nyquist plot, imaginary component of the total impedance (Z_{Im}) is plotted against the real component of the total impedance (Z_{Re}). In Bode plot, the log of total impedance magnitude ($\log |Z|$) and the phase angle (ϕ) are plotted on the right axis and left axis, respectively, against the log of ac frequency ($\log f$). Figure 5 shows typical types of impedance spectra for dissolved electroactive substance under semi-infinite conditions depending in the degree of reversibility of the electrode reaction it undergoes.

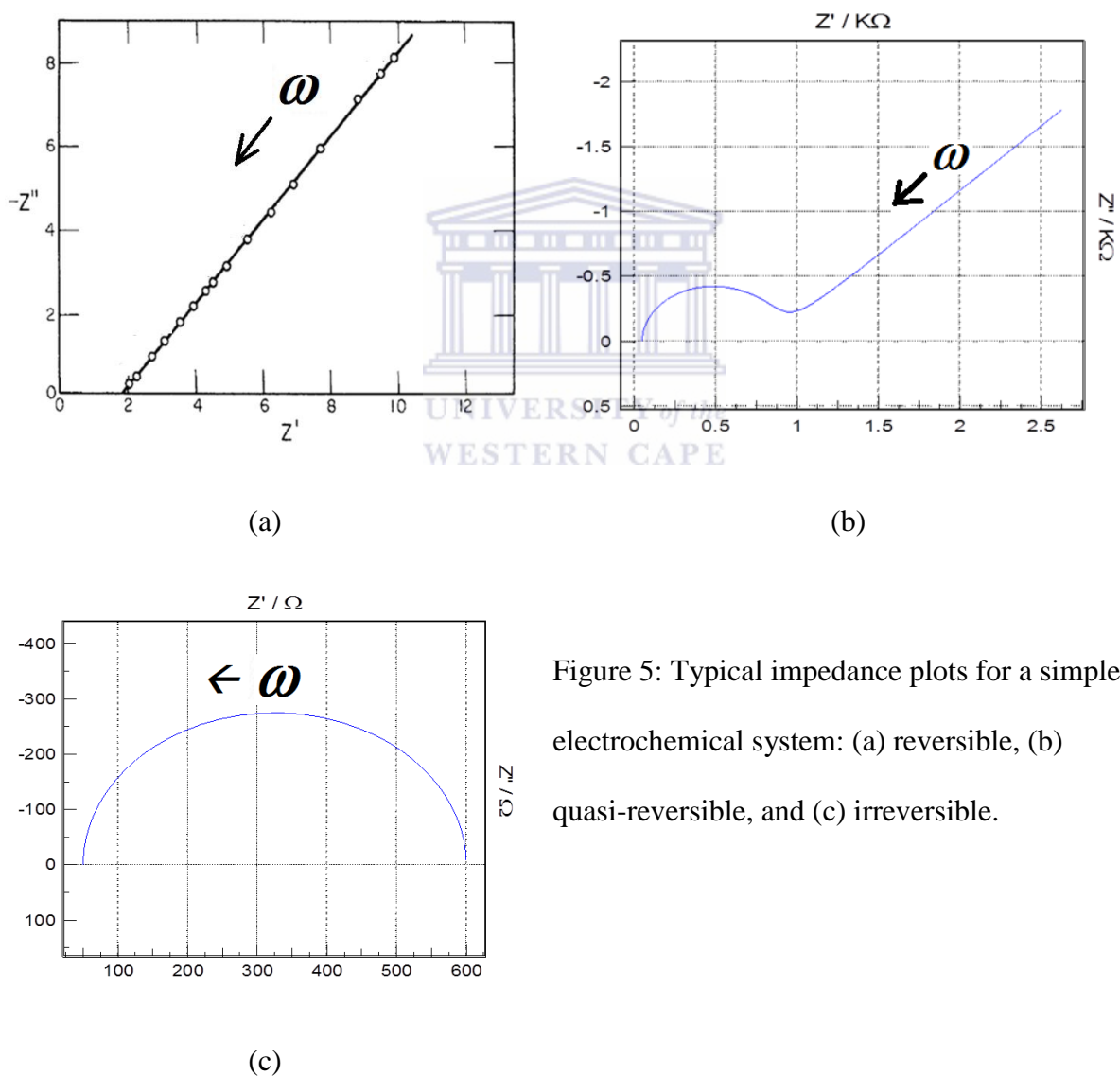


Figure 5: Typical impedance plots for a simple electrochemical system: (a) reversible, (b) quasi-reversible, and (c) irreversible.

The interpretation of an impedance spectrum depends on the model of the system under study. It can provide detailed information of the systems under examinations; parameters such as corrosion rate, electrochemical mechanisms and reaction kinetics, detection of localized corrosion, can all be determined from these data. The Randle's cell (see Figure 6) is simplest electrical equivalent circuit model for the heterogeneous electron transfer reaction ($\text{Ox} + n\text{e}^- \rightarrow \text{Red}$) involving n ($=1$ or 2) electrons, if the electroactive reactant (Ox) is dissolved in an electrolyte solution of sufficient conductivity and the electrochemical reaction is not extensive enough to alter the composition of the bulk of the electrolyte, the product (Red) is stable and also soluble in the electrolyte.

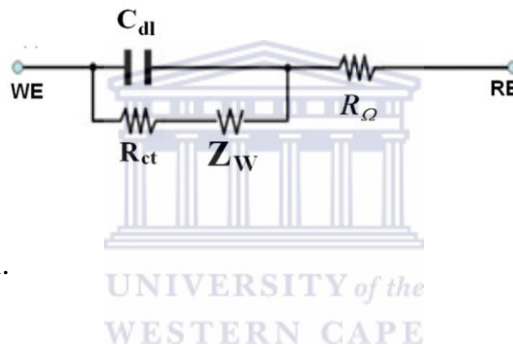


Figure 6: The Randles cell.

Where:

WE = Working Electrode

Z_w = Warburg impedance

C = Capacitance

C_{dl} = double layer capacitance (also C_d)

R_{Ω} = uncompensated ohmic solution resistance (also R_u)

RE = reference electrode

The impedance of a purely resistive element is equal to the magnitude of its resistance (R) and constant regardless of the frequency of the ac-excitation input ($Z_R = R$). The double layer capacitor of an electrode/ electrolyte system may some times approximately behave as a purely capacitive element, in which its impedance is given by equation (27), where $j = \sqrt{-1}$. Bode plots with phase angle of -90° is the hall mark of purely capacitive elements. In the presence of an electroactive substance, an RC parallel circuit of the charge transfer resistance (R_{ct}) and the double layer capacitance explains the arc in the impedance plots (also called ZARC) shown in Figures 8 (a) and (c), and Figure 7 as well.

$$Z_C = \frac{1}{j\omega C} \quad (27)$$

ZARCs are often observed as depressed semi-circles as in Figure 8(a) instead of the perfect semi-circles expected of ideal capacitor components in parallel with a charge transfer resistor [87]. Depressed semi-circles impedance plots are caused by non-ideal capacitive behavior exhibiting any constant phase angles less than -90° in absolute values. Thus, such impedance responses are modeled by an electrical equivalent circuit of a generalized element called the constant phase element (CPE) in parallel with a charge transfer resistor. The impedance of a CPE, Z_{CPE} is given by Equation 28 [88]:

$$Z_{CPE} = \frac{1}{T_{cpe}(j\omega)^{P_{cpe}}} \quad (28)$$

Where T_{CPE} is a scale coefficient and the power index P_{CPE} varies in the range $-1 < n < 1$. It is known that at P_{CPE} of 0.1 and -1, the CPE degenerates to resistance (R), a capacitance (C), and an inductance (L), respectively. In a limited frequency segment, the impedance corresponding to a positive fractional value of P_{CPE} may be modeled by a distributed RC

circuit while fractional negative values of P_{CPE} are modeled by a circuit consisting of RL elements.

The manifestation of a Warburg impedance (Z_W) - the impedance related with reactant diffusion-limitations – is known when a phase shift of -45° is exhibited in the impedance plot regardless of the frequency of the ac-excitation input. When the reactant traverses a semi-infinite diffusion length, diffusion impedance is referred to as the infinite Warburg ($Z_{W,\infty}$) and responsible for the diagonal line (slope = (-1)) in Figure 8 (a) and (b), and Figure 7 as well. Under an ideal situation, its complex and magnitude forms are given by Equations 29 and 30 [82].

$$Z_{W,\infty} = \frac{\sigma}{\sqrt{\omega}}(1 - j) \quad (29)$$

$$\bar{Z}_{W,\infty} = \frac{\sigma\sqrt{2}}{\sqrt{\omega}} \quad (30)$$



Where σ is the Warburg coefficient given by Equation 31.

$$\sigma = \frac{RT}{n^2 F^2 A \sqrt{2}} \left(\frac{1}{D_{Ox}^{1/2} C_{Ox}^{bulk}} + \frac{1}{D_{Red}^{1/2} C_{Red}^{bulk}} \right) \quad (31)$$

Thus $Z_{W,\infty}$ curves can be fit with two experimental parameters $W_R = \frac{\sigma\sqrt{2}}{\sqrt{\omega_o}}$ and P according to

Equation 32 where ω_o is a unit angular frequency and $P = 0.5$ in an ideal case. A Warburg impedance also can be fit with the model for the so-called the constant phase element (CPE) (see later in this section).

$$\bar{Z}_{W,\infty} = \frac{W_R}{\left(\frac{\omega}{\omega_o}\right)^P} \quad (32)$$

Figure 7 maps the equivalent circuit parameters for a general type of the impedance spectra exhibited by electrochemical systems which can be modelled by the Randle's cell [82].

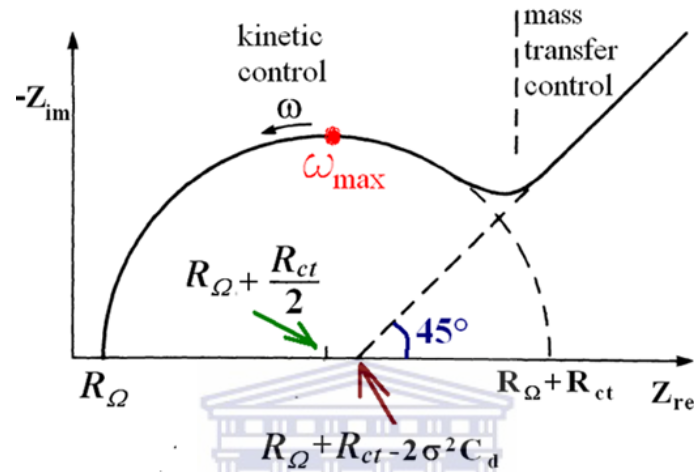


Figure 7: The impedance spectra exhibited by electrochemical systems which can be modelled by the Randle's cell.

Where:

ω = angular frequency of the sinusoidal ac-excitation potential or current input

ω_{max} = the angular frequency of the ac-input at which the maximum imaginary impedance when the impedance (Nyquist) plot forms an arc (semicircle).

Z_{re} (or Z') = real componnet of impedance

Z_{im} (or Z'') = imaginary component of impedance

$$\omega_{max} = 2\pi f_{max} = \frac{1}{R_{ct}C_{dl}}; \tau = R_{ct}C_{dl}; i_o = \frac{RT}{nFR_{ct}} \quad (33)$$

$$i_o = nFAk^o C_{Ox}^{bulk(1-\alpha)} C_{Red}^{bulk\alpha} \quad (34)$$

Where,

f_{max} = the frequency of maximum Z_{Im} in the semicircle of a Nyquist plot

τ = time constant for charge/ discharge process in an RC circuit

i_o = exchange current

During EIS measurements done on electroactive multi-layers or thick films, an impedance plot with a short Warburg-like line, in the region of higher frequencies, and an upward vertical line, in the low frequencies region, may be observed as shown in Figure 8(c) [88]. This is known as the finite length Warburg-open circuit terminus ($Z_{W,o}$). The open-circuit terminus is because of a geometric capacitor coming into the picture following the complete depletion of the reactant from film. Such impedance plots can be fitted with a three-parameters ($R_{W,o}$, $T_{W,o}$, and $P_{W,o}$) model according to Equation 35 [90, 91]. Under ideal conditions, $P_{W,o} = 0.5$ and the other two parameters are given by Equations 36 and 37.

$$Z_{W,o} = R_{W,o} \frac{ctnh[(jT_{W,o}\omega)^{P_{W,o}}]}{(jT_{W,o}\omega)^{P_{W,o}}} \quad (35)$$

$$R_{W,o} = \lim_{\omega \rightarrow 0} Z'_{W,o} \quad (36)$$

$$T_{W,o} = \frac{L^2}{D} \quad (37)$$

Where:

L = the effective diffusion thickness (or film thickness of the electroactive layer)

D = the effective diffusion coefficient

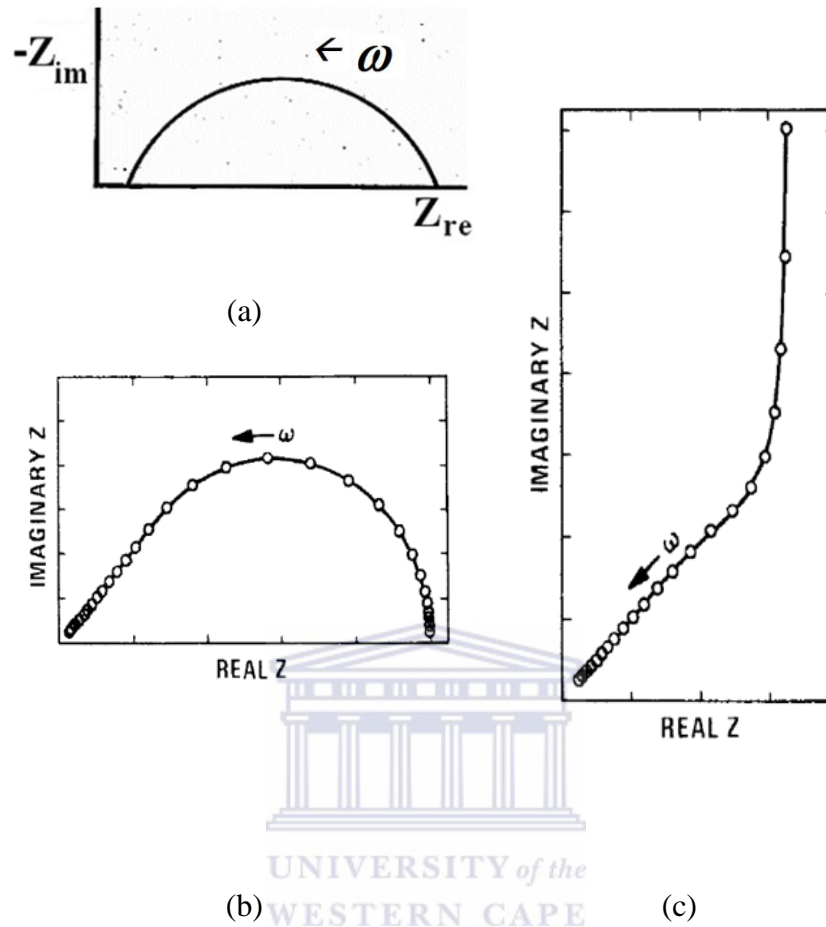


Figure 8: (a) A ZARC with depressed semi-circle; (b) Warburg short-circuit terminus; (c) finite length Warburg-open circuit [89].

Another diffusion impedance scenario is when carrying out a rotating disc electrode EIS measurement on a dissolved reactant under a semi-infinite condition. A short Z_W line would be terminated by an arc approaching the real-axis as in Figure 8(b). Such a impedance plots are termed finite length Warburg short-circuit terminus ($Z_{W,s}$), and can be modeled with a modified version of Equation 35: $ctnh$ function is replaced by the $tanh$ function; and its three parameters by $R_{W,s}$, $T_{W,s}$, and $P_{W,s}$, but still keeping the same mathematical significance.

Thin-layer electroactive films, mono-layers or a few molecular layers for which diffusion is not necessary for reaction to occur, exhibit impedance spectra without the Warburg line and

are described by a slightly different model, for instance as in Figure 9 [82]. “ C_{ads} ” is the capacitance of the geometric capacitor element arising as a result of the complete discharge of the thin-film. In contrast, for the simplest case of a thick electroactive-film electrochemistry, where diffusion is manifested as a finite length Warburg, the relevant equivalent circuit would be a modified version this model in which the Z_{W_o} or the C_{ads} is replaced by $Z_{W,s}$.

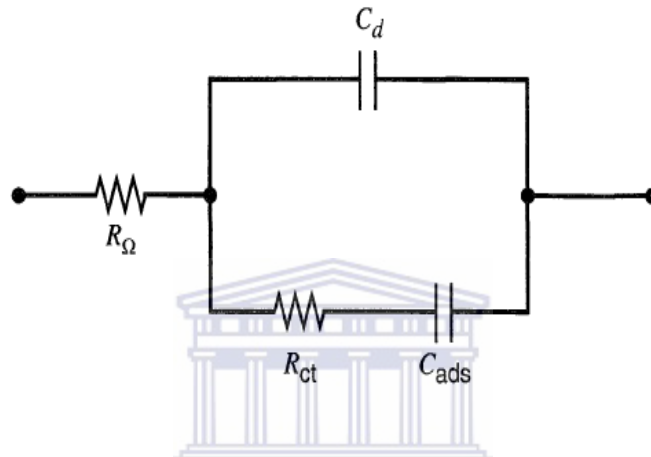


Figure 9: Equivalent circuit for a system in which the Warburg impedance is unimportant.

For reversible electrode reaction taking place in a thin film to which the reactant is confined, provided both reactant and product are insoluble in the interfacing electrolyte medium, and if intermolecular interactions before and after reaction are the same, a typical impedance spectrum would look like as follows:

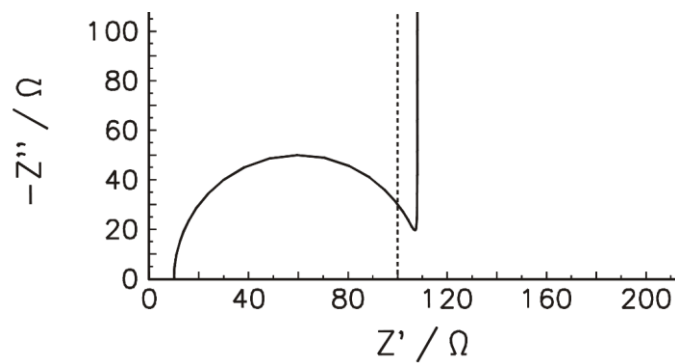


Figure 10: Impedance spectrum of a thin film of a reversibly electroactive material [93].

3.3 Fourier Transform Infrared (FTIR) Spectroscopy

FTIR is the most analytical device for identification of unknowns, determine the quality or consistency of a sample and determine the amount of components in a mixture [93]. It can be applied to the analysis of solids, liquids, and gases. FTIR is a non-destructive technique, provides a precise measurement method which requires no external calibration, increases speed, collecting a scan every second, can increase sensitivity – one second scans can be co-added together to ratio out random noise, has greater optical throughput and is mechanically simple with only one moving part [94]. FTIR is perhaps the most powerful tool for identifying types of chemical bonds (functional groups). The wavelength of light absorbed is characteristic of the chemical bond as can be seen in this annotated spectrum. In infrared spectroscopy, IR radiation is passed through a sample. Some of the infrared radiation is absorbed by the sample and some of it is passed through (transmitted). The resulting spectrum represents the molecular absorption and transmission, creating a molecular fingerprint of the sample. Like a fingerprint no two unique molecular several types of analysis [95].

Thus, the Fourier Transform Infrared (FTIR) technique has brought significant practical advantages to infrared spectroscopy. It has made possible the development of many new sampling techniques which were designed to tackle challenging problems which were impossible by older technology. It has made the use of infrared analysis virtually limitless [96].

3.4. Microscopy Techniques

Microscopy Techniques uses microscopes to view samples and objects that are not within the resolution range of the normal eye. There are three well-known branches of microscopy, optical, electron, and scanning probe microscopy [97].

Optical and electron microscopy involve the diffraction, reflection, or refraction of electromagnetic radiation/electron beams interacting with the specimen, and the subsequent collection of this scattered radiation or another signal in order to create an image. This process may be carried out by wide-field irradiation of the sample (for example standard light microscopy and transmission electron microscopy) or by scanning of a fine beam over the sample [98]. A scanning electron microscope (SEM) is a type of electron microscope that images a sample by scanning it with a focused beam of high-energy electrons to generate variety of signals at the surface of solid specimens. The signals that derive from electron-sample interactions reveal information about the sample including external morphology (texture), chemical composition, and crystalline structure and orientation of materials making up the sample [99]. In most applications, data are collected over a selected area of the surface of the sample, and a 2-dimensional image is generated that displays spatial variations in these properties. Areas ranging from approximately 1 cm to 5 microns in width can be imaged in a scanning mode using conventional SEM techniques (magnification ranging from 20X to approximately 30,000X, spatial resolution of 50 to 100 nm). The SEM is also capable of performing analyses of selected point locations on the sample; this approach is especially useful in qualitatively or semi-quantitatively determining chemical compositions (using EDS), crystalline structure, and crystal orientations (using EBSD). The design and function of the SEM is very similar to the EPMA and considerable overlap in capabilities exists between the two instruments [100].

4. EXPERIMENTAL

4.1 Chemicals and Materials

4.1.1 Chemicals

- 1-Methyl-3-octylimidazolium bis(trifluoromethylsulfonyl)imide (Merck, $\geq 99\%$, Product # 00797)
- Graphite powder (natural micro crystal grade, Aps 2-15 microns, 99.9995 %) (Alfa Aesar, Product # 14736)
- Paraffin oil (Spectranal, Riedel-De Haen, Product # 8012-951)
- $\text{CuCl}_2 \cdot 6\text{H}_2\text{O}$ (99%) (Riedel-De Haen, Product #62330)
- $\text{FeCl}_2 \cdot 4\text{H}_2\text{O}$ (99%) (Sigma-Aldrich, Product # 577002-149)
- $\text{CoCl}_2 \cdot 6\text{H}_2\text{O}$ (98%) (Sigma-Aldrich, Product # 565553-059).
- $\text{Ce}(\text{SO}_4)_2 \cdot 4\text{H}_2\text{O}$ ($>98\%$) (SAAR Chem., Product # 27978)
- $\text{MnSO}_4 \cdot \text{H}_2\text{O}$ (98.0%) (BDH Chemicals, Product #10355).
- H_2O_2 (30%) (Sigma-Aldrich, Product # 95302)
- Potassium hexacyanoferrate (*III*) (98%) (Fluka, Biochemica, Product # 60280)
- KCl (99.5%) (Fluka, Biochemica, Product # 60128)
- NH_4Cl (99.5%) (Fluka, Biochemica, Product # 09700)
- LiCl (99.0%) (Fluka, Product # 73036)

- KNO_3 (99.0%) (Sigma Aldrich, Product # 542040)
- NaCl ($\geq 99.5\%$) (Sigma Aldrich, Product # S9625)
- CH_3COONa ($\geq 99.0\%$) (Sigma Aldrich, Product # S8750)
- NaClO_3 ($\geq 99\%$) (Sigma Aldrich, Product # 244147)

4.1.2 Reagent solutions

All solutions were prepared with ultrapure water ($18\text{M}\Omega\text{ cm}$) from a reverse osmosis/ ion-exchange combined water purification system (RiosTM 3/ Synergy, Millipore)

4.2 Carbon Paste Preparation & Electrode Construction

4.2.1 Paraffin/ carbon paste electrode (PCPE)

The PCPE was prepared by thoroughly hand mixing 0.30 g of graphite powder with 200 μL of paraffin oil in an agate mortar; mixing proceeded for 20 minutes to produce a well homogenized paste. A small portion of the resulting paste was taken with polyethylene tip and packed tightly into a Teflon tube electrode body (BAS, MF-2015) with internal diameter 1.6 mm. The surface of the CPE was always polished to visual flatness on a paper and rinsed with ultrapure water prior to each experiment.

4.2.2 Ionic liquid/ paraffin/ carbon paste electrode (ILPCPE)

ILPCPE was prepared by thoroughly hand mixing 0.30 g of graphite powder with 50:50 paraffin oil/ [MOIM] [Tf_2N] (i.e. 100 μL paraffin oil and 100 μL of [MOIM][Tf_2N]) in an agate mortar; mixing proceeded for 20 minutes to produce a well homogenized paste. A small portion of the resulting paste was taken with polyethylene tip and packed tightly into a Teflon

tube electrode body (BAS, MF-2015) with internal diameter 1.6 mm. The surface of the CPE was always polished to visual flatness on a paper and rinsed with ultrapure water prior to each experiment.

4.3 Electrochemical Measurements

Electrochemical experiments i.e. cyclic voltammetry were performed with BAS 100B and BASi Epsilon electrochemical analyzers (Bioanalytical systems, Inc.) controlled with software BAS100W and Epsilon software (Bioanalytical Systems, Inc., West Lafayette, USA), respectively. Electrochemical impedance spectroscopy measurements were performed using the PAR 273A potentiostat (Princeton Applied Research) and a Lock in amplifier (Signal Recovery, Model 5210) while the data acquisition was made via the PowerSINE and PowerCV software (Princeton Appli. Res., Version 2.46, 2003 AMETEK, INC., Berwyn, PA, USA). Complex non-linear least squares (CNLS) fitting of impedance data to equivalent circuit models were done by the help of the Z-view software (Version 3.1c, 1990-2007 Scribner Associates, inc., Sothern Pines, NC, USA). The goodness of fit indicators for EIS-modeling, Chi-squared and sum of squares were always kept less than or equal to 10^{-3} and 0.1, respectively. All studies were carried out with a three-electrode system, the CP electrode as the working electrode, platinum wire as auxiliary/counter electrode, and an Ag/AgCl (3M NaCl) as reference electrode. Measurements were carried out in various electrolytes (0.1M) which were always purged with ultra-pure Argon (Afrox, South Africa) and kept under Ar blanket during measurements.

4.4 ATR-FTIR Measurements

Attenuated total internal reflectance FTIR measurements were carried out using the Model Spectrum100 (PerkinElmer).

4.5 Preliminary Electrochemical Studies

The prepared CP electrodes were characterized with respect to their background voltammograms and their responses to the hexacyanoferrate (II/III) and hydrogen peroxide redox systems. The kinetics of hexacyanoferrate(II/III) system was studied both by recording the cyclic voltammograms (CVs) at various scan rates, and by electrochemical impedance spectroscopy (EIS).

4.6 Effecting and Probing of Metal oxide Species Electrodeposition

1000 μL of 0.1 M aq. solution of the metal ion (Fe^{2+} , Cu^{2+} , Co^{2+} , and Mn^{2+}) was added to 10 mL of the KCl supporting electrolyte. In the case of Ce^{2+} ion, the volume added was only 100 μL because it significantly precipitated. Then cyclic voltammograms of the ions were recorded between +1.5 V to -1.8 V at 0.1 V/s starting with a cathodic scan from 0.0 V. After the recording of the voltammogram was completed, the deposition of any metallic species from the solution was then probed by running CV of the resulting CP electrode in a new portion of KCl solution. In separate set of experiments, an additional electrochemical probe, H_2O_2 was spiked into the supporting electrolyte and CVs were recorded.

5. RESULTS AND DISCUSSION

5.1 Preliminary Studies on as Prepared Ionic Liquid Carbon Paste Electrodes

5.1.1 Background cyclic voltammogram (CVs) in aq. KCl (0.1 M) solution

In Figure 11 shown are overlaid background CVs of the PCPE (black), ILPCPE (red), and ILCPE (green) in aq. KCl (0.1 M) solution. Similar potential windows which spanned between +1.5 V to -1.8 V were observed regardless of the electrode type. However, the introduction of the ionic liquid raised the background double layer charging current by about 100-folds relative to typical value for the PCPE (0.1 μA). Typical residual Faradaic peaks were also increased by about as high as 50-folds relative to that of the PCPE (1.4 μA). The range of potential of pure charging currents spanned from 1.4 to (-) 1.6 V in the absence of the ionic liquid, and between 1.00 and -1.00 V after the introduction of the ionic liquid. In the case of the ILCP, the background current was even much more excessive, for example, it had a 10-fold charging current relative to the ILPCP. The trend in the magnitude of background current was as follows: ILCP > ILPCP > PCP. The increase in background current in accordance with previous studies on ionic liquid-modified carbon paste electrodes [101]. Possible causes include electro-active impurities in the ionic liquid, ionic-migration within the carbon paste, and enhanced double-layer charging phenomena. Nevertheless, the fact that the overall potential windows of both electrodes were identical meant the ILPCPE provides a new electrochemically inert surface for the study and sensing of as many substances as which have been tested with traditional CPE. Furthermore, the high residual and background current characteristics of the IL/PCPE makes it a candidate for applications in super-capacitors.

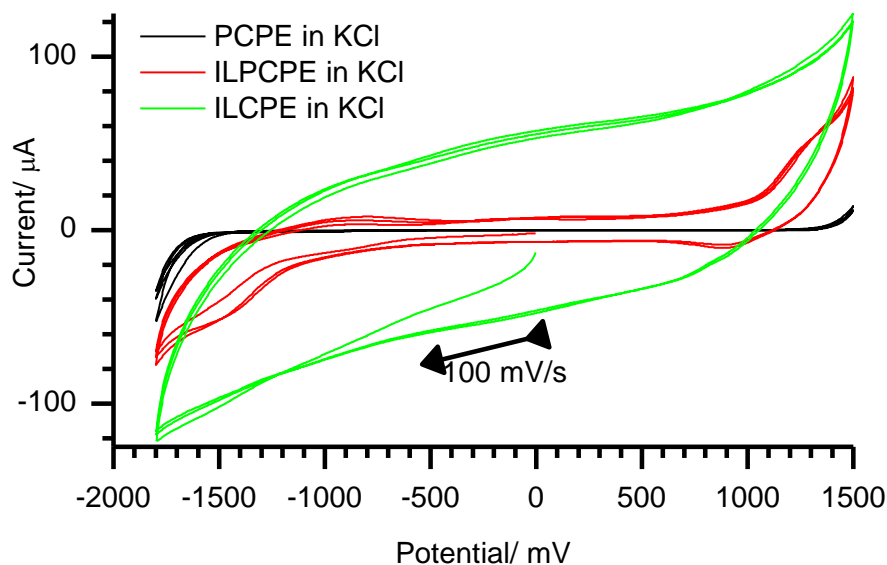


Figure 11: Background CVs of PCPE (black), ILPCPE (red), and ILCPE (green) in aq. KCl.

5.1.2 Cyclic voltammogram of $\text{Fe}(\text{CN})_6^{3-/4-}$

$\text{Fe}(\text{CN})_6^{3-/4-}$ is the most common standard redox system utilized for probing electrochemical activities of bare and modified electrodes. As presented in a later section in this work, the electrode kinetics of this redox probe was also studied to evaluate the PCPE, ILPCPE, and ILCPE. Typical cyclic voltammograms recorded at a scan rate of 100 mV/s for $\text{Fe}(\text{CN})_6^{3-}$ (0.004 M) in aq. KCl (0.1 M) solution are shown in Figures 12 (a), (b), and (c), respectively. The highest peak height (current density) was observed at the ILCP according to the order: $I_p(\text{ILCP}) \gg I_p(\text{ILPCP}) > I_p(\text{PCP})$. Thus, the electrode reaction of $\text{Fe}(\text{CN})_6^{3-/4-}$ was found to be faster because of incorporating the IL.

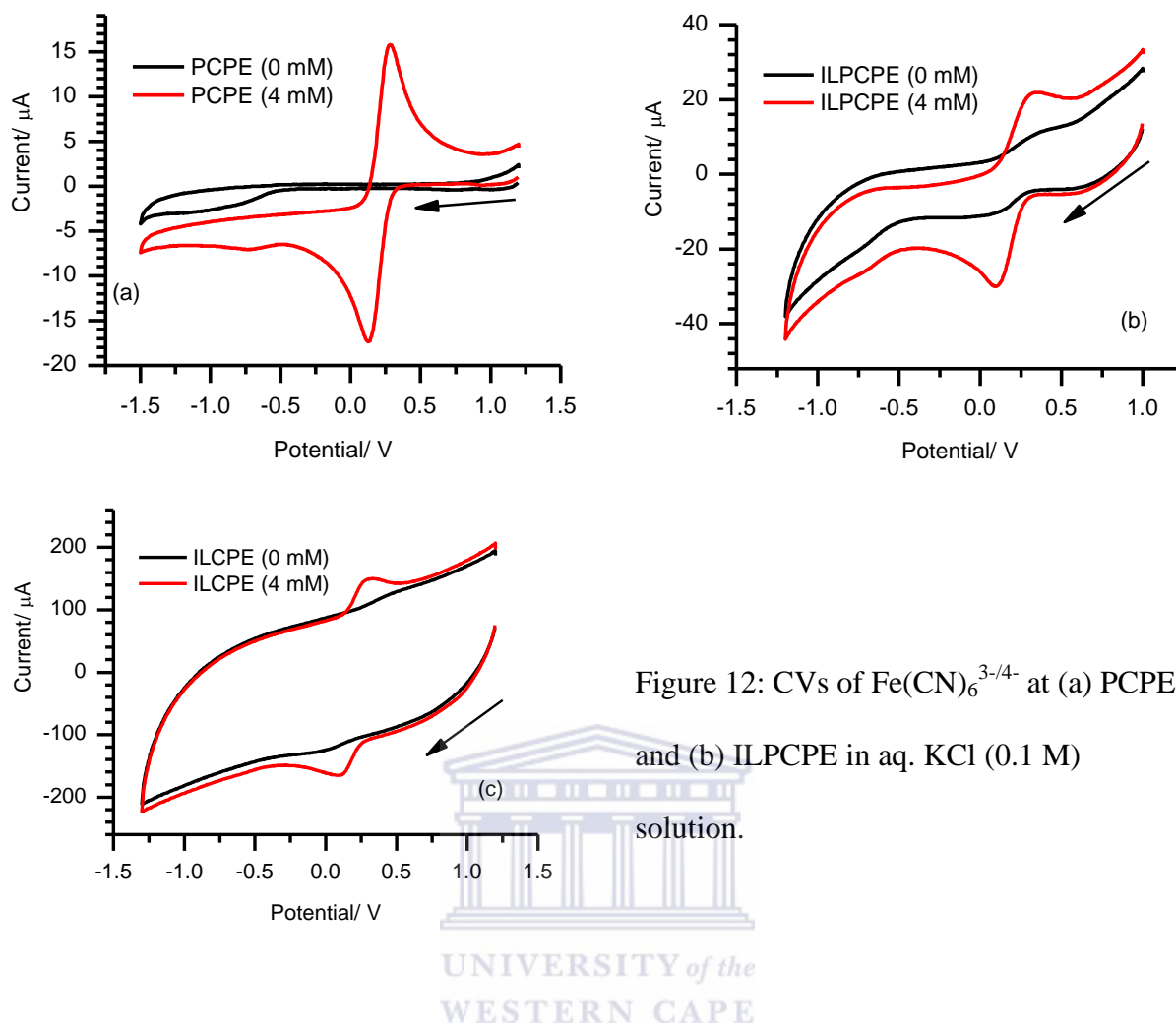


Figure 12: CVs of $\text{Fe}(\text{CN})_6^{3-/4-}$ at (a) PCPE and (b) ILPCPE in aq. KCl (0.1 M) solution.

5.1.3 Cyclic voltammogram of H_2O_2 in aq. KCl (0.1 M) solution.

Since multi-valent metal oxides or hydroxides are known for their electrocatalytic or electron-transfer mediation activities in H_2O_2 electrochemistry [3], H_2O_2 was exploited in this work as a probe for signaling the formation of electrodeposited metal oxide/ hydroxide products at the PCP and ILPCP electrodes. Thus, CVs of H_2O_2 at the freshly prepared CP electrodes were first studied to generate control voltammograms. According to Figure 13c, H_2O_2 exhibited higher current at the PCPE than at the ILPCPE. The anodic peak observed at about 1.5 V (for the PCPE) was diminished when the ILPCPE was used. It even disappeared totally in the case of the ILCP electrode. However, a small new cathodic peak was apparently

observed at about -0.75 V for the ILPCPE. The cathodic reaction at both electrodes was irreversible and no oxidation peak was observed.

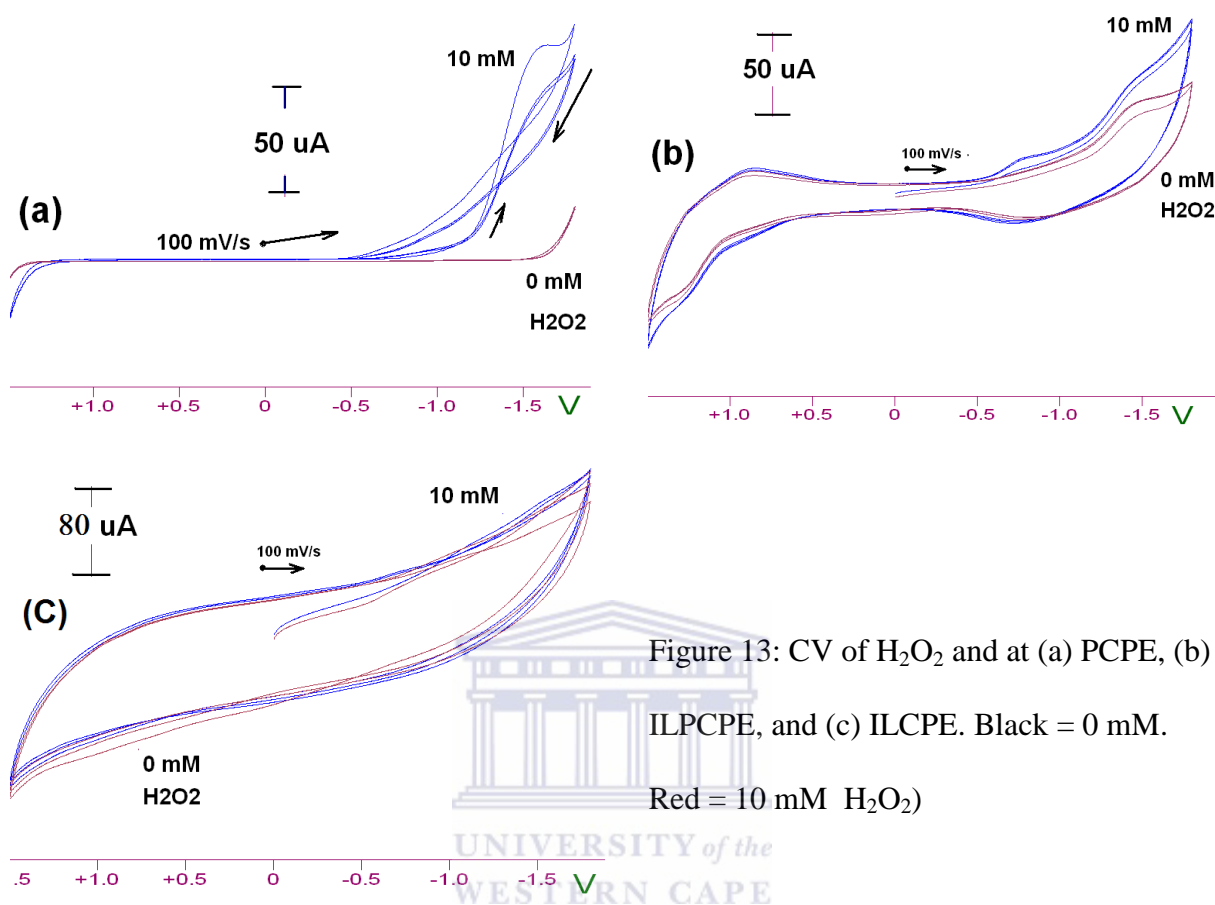


Figure 13: CV of H₂O₂ and at (a) PCPE, (b) ILPCPE, and (c) ILCPE. Black = 0 mM. Red = 10 mM H₂O₂)

5.1.4 Scanning electron microscopic examination

Figure 14 shows the scanning electron microscopic top views of a pure graphite powder (a) and the three carbon paste electrode prepared from this graphite powder using paraffin (nujol) (b), ionic liquid + paraffin mixture (c), and ionic liquid (d) as binders. In (a), graphite flakes were observed, isolated and irregularly oriented since the powder was not processed into a paste. In (b), (c), and (d), well compacted and ordered flakes were observed for the PCPE, ILPCPE and ILCPE samples due to the presence of the binding liquids and the process followed during the preparation of these pastes. It appears that, as a liquid with good

conductivity, high viscosity, and possessing ions which can interact with surface functional groups of the graphite particles, the RTILs exhibited enhanced binding of more particles and surface area coverage resulting in more compact pastes than the conventional mineral oil.

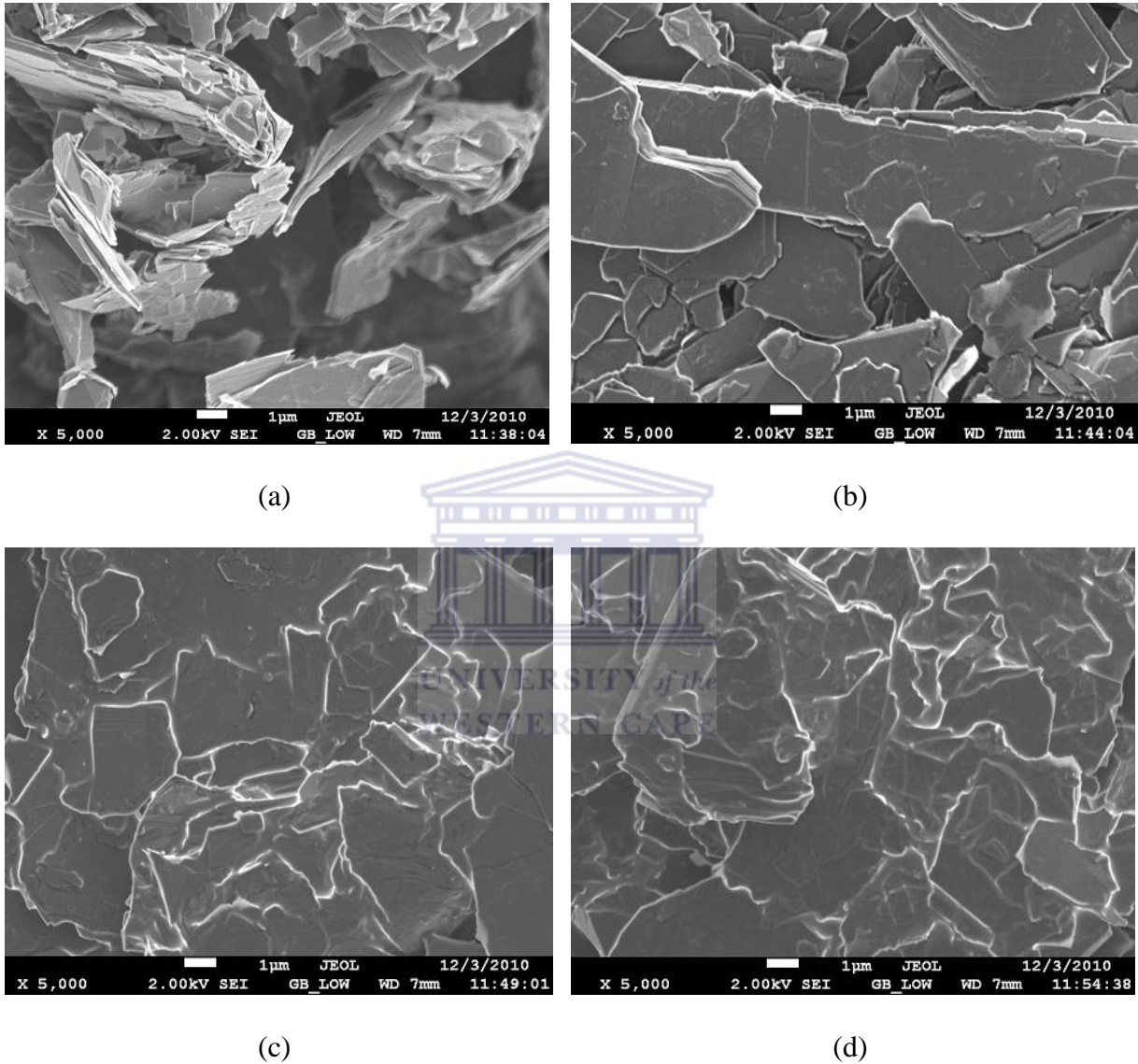


Figure 14: SEM images of (a) Graphite, (b) PCPE, (c) ILPCPE, and (d) ILCPE

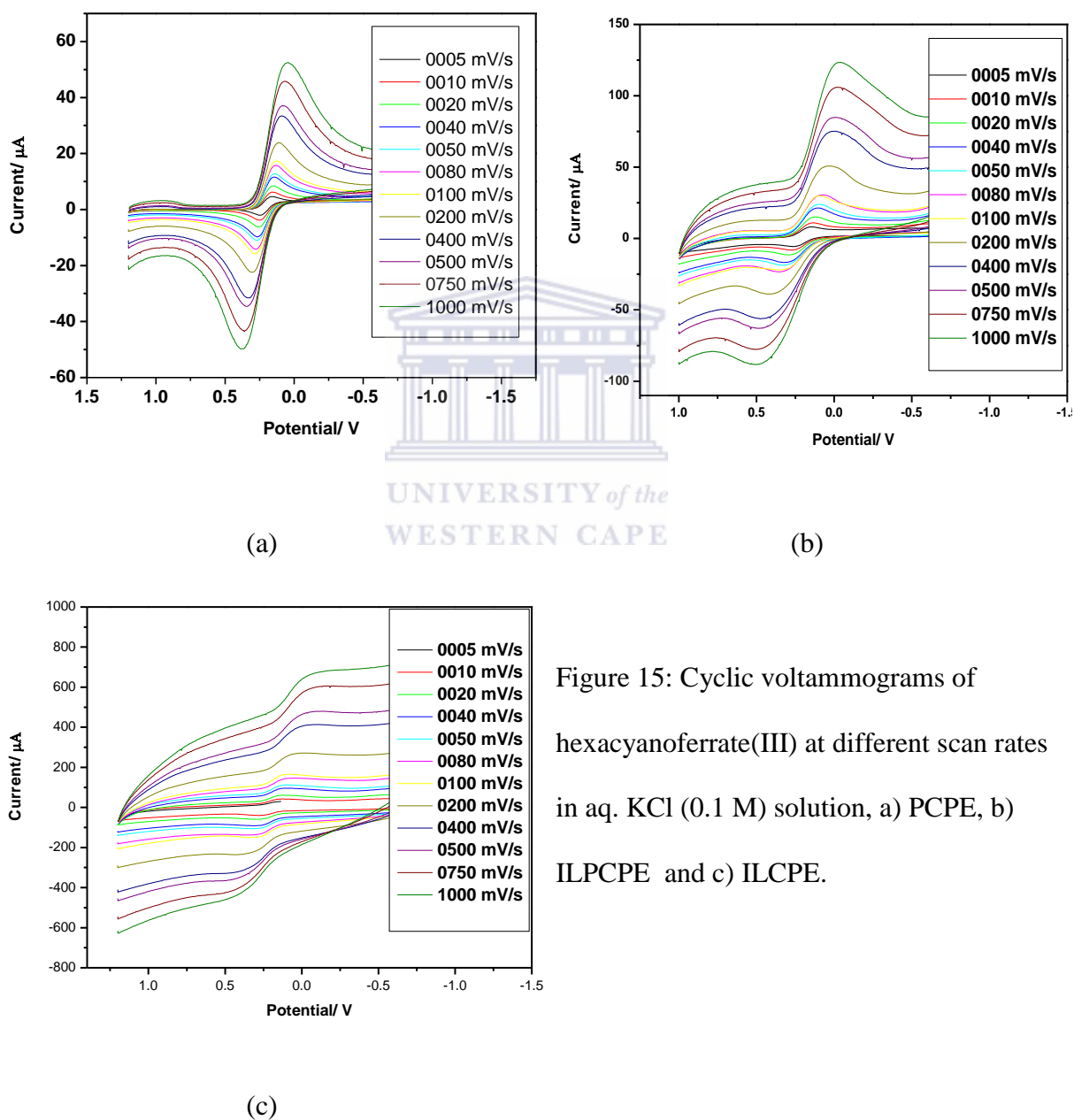
Page Left Blank

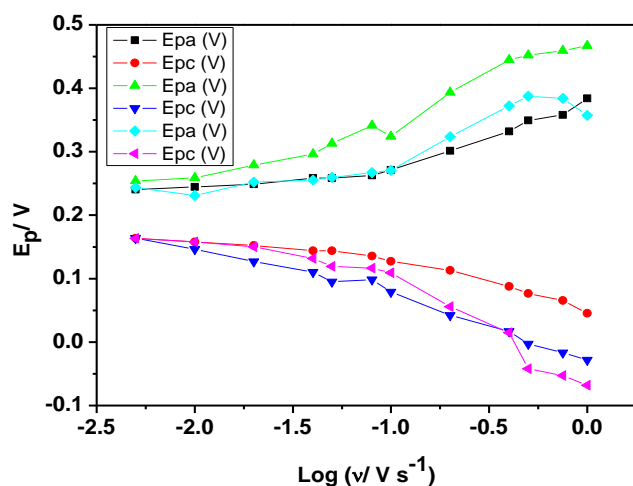


5.2 Electrode Kinetics of $\text{Fe}(\text{CN})_6^{3-/4-}$ at PCPE, ILPCPE, and ILCPE

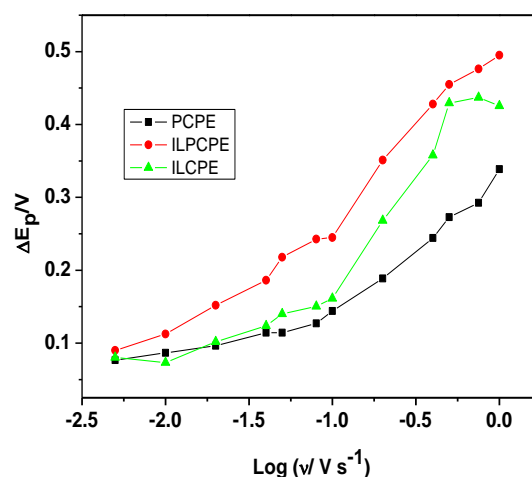
5.2.1 Cyclic voltammetry

Cyclic voltammograms of $\text{Fe}(\text{CN})_6^{3-/4-}$ recorded at different scan rates (0.005 to 1.000 V/s) for the PCPE, ILPCPE, and ILCPE are shown in Figure 15.

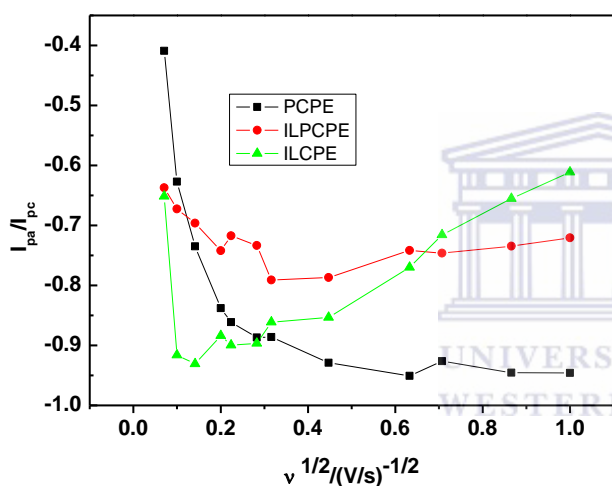




(a)



(b)



(c)

Figure 16. Dependence of E_{pa} , E_{pc} , ΔE_p , i_{pa}/i_{pc} ratio on scan rate for CVs of $\text{Fe}(\text{CN})_6^{3-}$ (4 mM) at three CP electrodes in aq. KCl (0.1 M) solution.

Various plots based on CVs of $\text{Fe}(\text{CN})_6^{3-/4-}$ (0.005 mV/s to 1 V/s) presented in Figure 16 for each type of electrode is shown. Based on how the plots of peak separation (ΔE_p) varied with $\log v$, conclusions were made as to the extent of the reversibility of the electrode reactions. The reaction gradually shifted from being reversible to being irreversible as the scan rate was increased regardless of the electrode type. Using the linear section of the respective E_{pc} vs $\log v$ plots, the cathodic transfer coefficients (α) was estimated for the reaction at each electrode according to Equations 13 and 14. D_o is diffusion coefficient of $\text{Fe}(\text{CN})_6^{3-}$. The “ α ” values thus determined were used in the calculation of the standard heterogeneous rate constant (k^0)

from the intercept. In Table 3 presented are α and k^o together with effective electrode areas (A_{eff}), mean formal potentials (E^o), and mean peak current ratios (i_{pa}/i_{pc}). Literature values of $6.1 \times 10^{-5} \text{ cm}^2/\text{s}$ and $5.8 \times 10^{-5} \text{ cm}^2/\text{s}$ in 0.1 M KCl solution [102, 103] were used for D_{Red} (diffusion coefficient of $\text{Fe}(\text{CN})_6^{4-}$) and D_{Ox} , respectively, in Equations 11 and 12 in order to estimate A_{eff} .

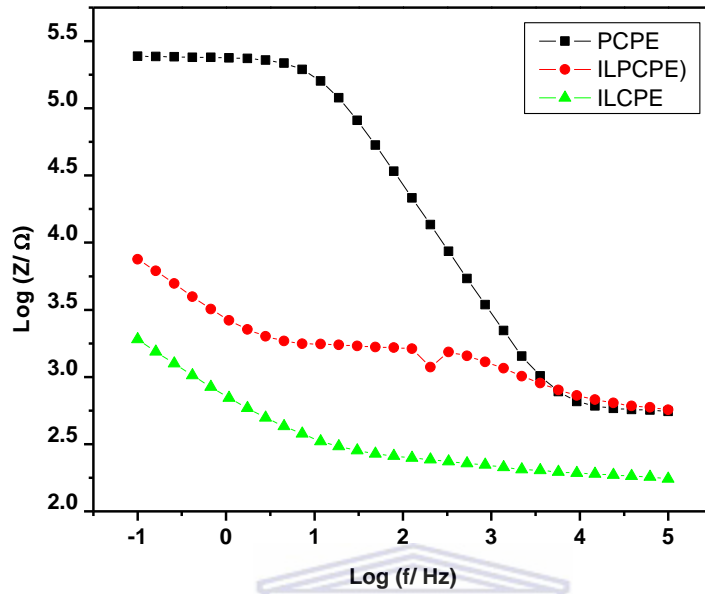
Table 3: Electrode properties and $\text{Fe}(\text{CN})_6^{3-/4-}$ electrode-kinetics data based on CV analysis are shown.

Parameter	A_{geom}/ cm^2	A_{eff}	E^o/ V	I_{pa}/I_{pc}	α	$k^o/ 10^{-3} \text{ cm/s}$
Method	πr^2		Mean	Mean	$E_{pc} \text{ vs } \log \nu$	$E_{pc} \text{ vs } \log \nu$
PCP	0.0201	0.0258	0.207	1.07	0.603	1.5
ILPCP	0.0201	0.0365	0.206	0.86	0.441	1.0
ILCP	0.0314	0.0513	0.201	1.05	0.332	1.7

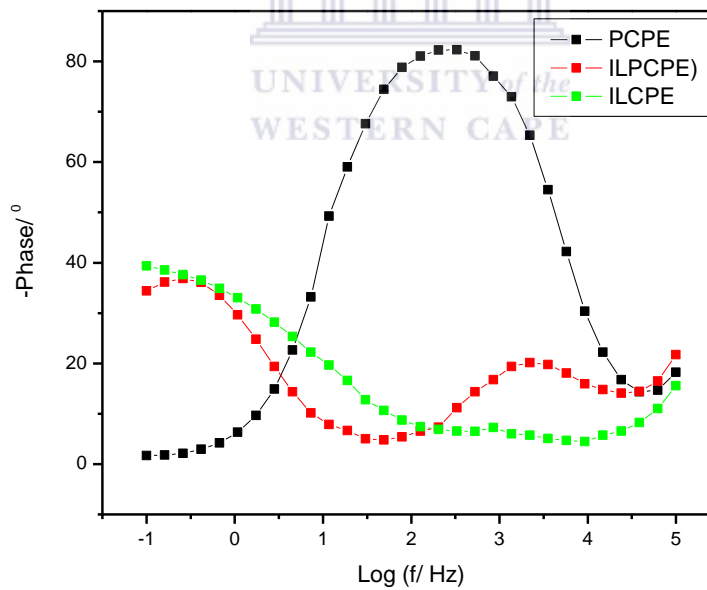
5.2.2 Electrochemical impedance spectroscopy

Electrochemical impedance spectroscopy (EIS) measurements were carried out in the presence and absence of $\text{Fe}(\text{CN})_6^{3-/4-}$ solution. Bode plots of the three electrodes, i.e. PCPE, ILPCPE, and ILCPE are shown in Figure 17 (a) and (b) for the frequency range 10^{-1} to 10^5 Hz. Generally, the PCPE and the ILCPE respectively exhibited the highest and the lowest impedances due to the higher conductivity of the IL compared to paraffin. The equivalent circuit models in Figure 18 were used to fit and interpret all EIS results. R_{u-t} is the total sum of the un-compensated solution resistance (R_{u-s}) and the ohmic resistance of the electrode material (R_{u-m}) itself. Thus, the differences between R_{u-t} values of the different electrode/KCl systems were understood as dominantly arising from the difference between the natures of

the electrode materials themselves. CPE and R_{ct} respectively represent constant phase elements and charge transfer resistances.



(a)



(b)

Figure 17: Impedance spectra (Bode Plots) in aq. KCl (0.1 M) solution in the presence of $Fe(CN)_6^{3-/4-}$ (8 mM; 1:1), $E_{ac}= 0.010$ V, $E_{dc} = 0.2$ V (for PCP & ILPCP) or 0.17 V (ILCP).

R_{u-t} and Z_{CPE} of similar order of magnitudes as the R_u and Z_{CPE} determined in the absence of $\text{Fe}(\text{CN})_6^{3-/4-}$ were found for all the electrodes. But, the charge transfer resistances (R_{ct}) in the presence of $\text{Fe}(\text{CN})_6^{3-/4-}$ and, hence, the exchange current densities (I_o) were significantly different from the corresponding background values, which are presented in Table 4. The PCP and ILPCP electrodes' equivalent background contributions were about 10% and 13%, respectively. Furthermore, the equivalent circuit for the ILPCP electrode still contained two time constants. In the case of the ILCP electrode, its impedance spectrum in the presence of $\text{Fe}(\text{CN})_6^{3-/4-}$ indicated the need to incorporate a new resistance/ capacitor (RC) element (R_{ct2} , Z_{CPE2}) in the series with the CPE-element, which was already identified in the absence of $\text{Fe}(\text{CN})_6^{3-/4-}$.

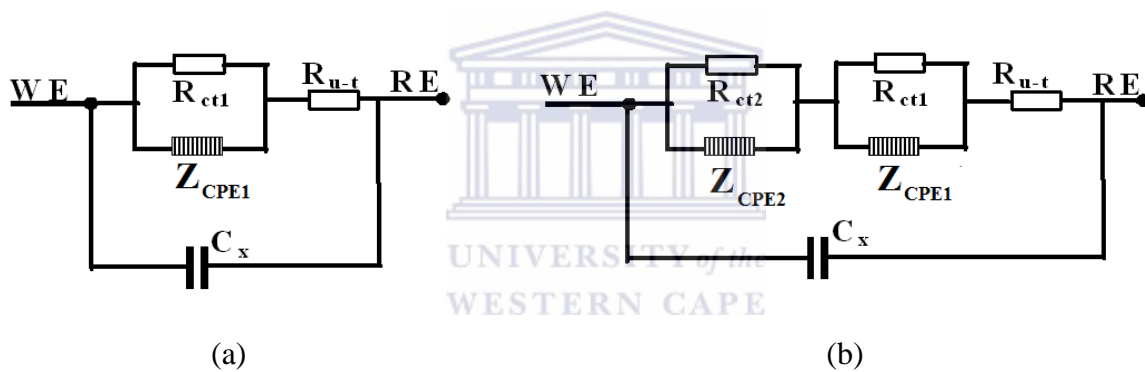


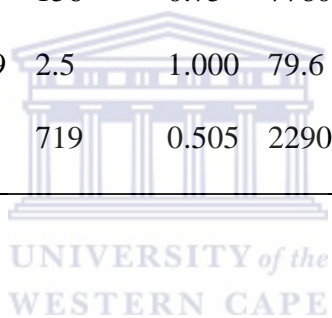
Figure 18: Generalised equivalent circuit models for: (a) PCP and (b) ILCP and ILPCP in the presence of a redox active substance.

The k^o values for the electrode reaction in question were calculated according to Equation 34 from the respective I_o without a need for background correction. Unlike the magnitudes of k^o , which were estimated using the CV data, the k^o values evaluated from the EIS data varied significantly across the different types of electrodes. The ILCP electrode exhibited the highest k^o (81×10^{-3} cm/s) and the PCP exhibited the lowest k^o (1.38×10^{-5} cm/s) values. Therefore, the trend in k^o may be summarized as follows: k^o (ILCP) \gg k^o (ILPCP) \gg k^o

(PCP). Each of the k^o estimated by EIS were two orders of magnitude smaller than the respective k^o values determined by the CV.

Table 4: Equivalent circuit and kinetic parameters estimated using the EIS data (Figure 17) for PCPE, ILCPE, and ILPCP in $\text{Fe}(\text{CN})_6^{3-/4-}$ (8 mM)/ aq. KCl (0.1 M) solution.

Electrode	$R_{ct}/$	$T_{CPE}/$	P_{CPE}	$T_{CPE}/$	$I_o/$	$k^o/$
	$\text{k}\Omega \text{ cm}^2$	$\text{s}^P \text{ M}\Omega^{-1}$		$\text{s}^P \text{ M}\Omega^{-1} \text{ cm}^{-2}$	$\mu\text{A cm}^{-2}$	$10^{-3} \text{ cm s}^{-1}$
PCP	4.84	0.068	0.976	3.4	5.31	0.0138
ILPCP (R_{ct1} , CPE1)	0.0199	0.7	0.795	34.8	98.3	0.255
ILPCP (R_{ct2} , CPE2)	0.261	156	0.75	7760	322	N/A
ILCP (R_{ct1} , CPE1)	0.000819	2.5	1.000	79.6	314000	81.3
ILCP (R_{ct2} , CPE2)	-	719	0.505	22900	-	-



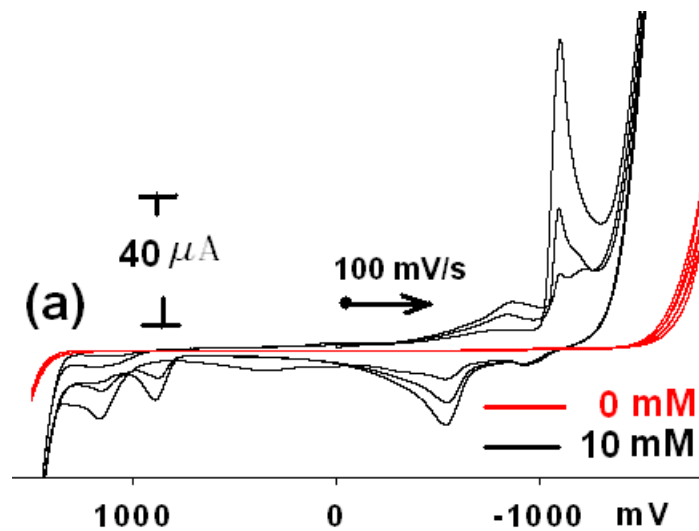
5.3 Electrodeposition of Selected Transition Metal Ions in aq. KCl (0.1 M) solution

Potentiodynamic electrodeposition of multivalent oxy-hydroxy metal oxides was investigated using the solutions of the source ions Fe^{2+} , Cu^{2+} , Co^{2+} , Ce^{4+} , and Mn^{2+} in aq. KCl (0.1 M) solution. As will be shown soon, only Fe^{2+} , Cu^{2+} , and Mn^{2+} were found to have been successfully electrodeposited as concluded based on cyclic voltammetric hallmarks observed during and after electrodeposition.

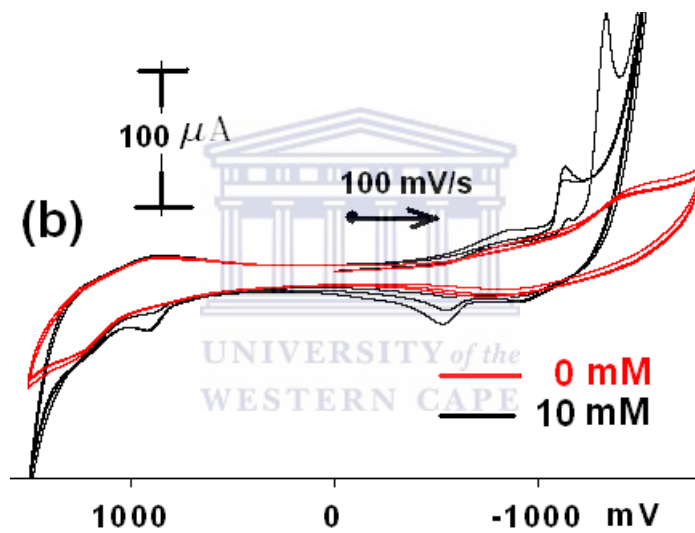
5.3.1 Electrodeposition cyclic voltammograms

Iron (II)

Figure 19 shows CVs of (a) PCPE and (b) ILPCPE in the presence of Fe^{2+} in aq. KCl (0.1 M) solution. The CVs were recorded starting from 0 V where no reaction occurred. Various peaks were observed to evolve and increased in peak height as the number of cycles increased KCl solution. The ionic liquid enhanced the reduction peak current of Fe^{2+} at the CP electrode in aq. KCl (0.1 M) solution, but it generally shifted the peak potentials to higher overpotentials. The increase in peak height and shift in peak potential with cycle number strongly indicated the occurrence of alterations in surfaces of both PCP and ILPCP electrodes as electrode reactions progressed. Most of the peaks in the case of the ILPCP were at higher over-potentials than the corresponding peaks observed for the PCP electrode. This indicated that the electrode reaction was influenced by the presence of the ionic liquid. Formation of electrodeposited species onto both ILPCP and PCP electrodes, hence the ILPCP//FeOx and PCP//FeOx, was confirmed by new and stable cathodic and anodic peaks after changing medium.



(a)

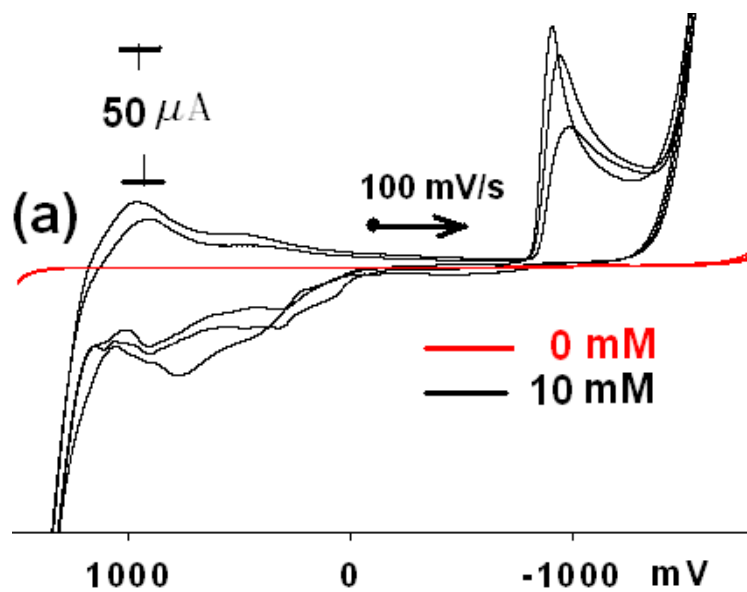


(b)

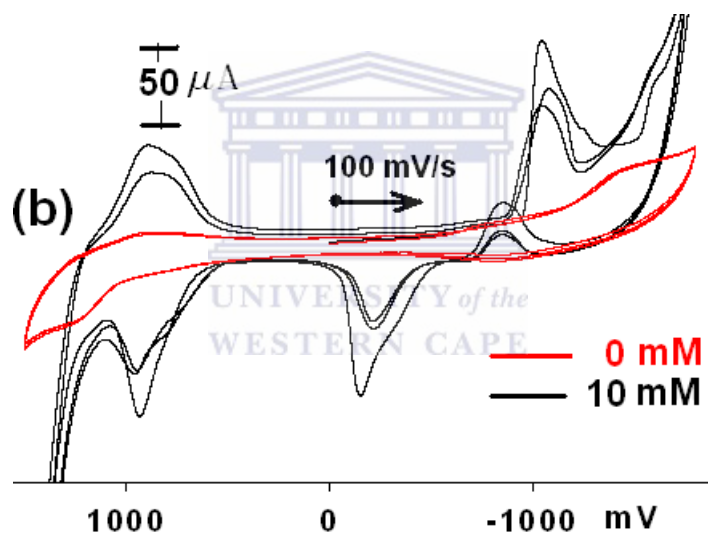
Figure 19: CVs recorded for PCPE (a) and ILPCP (b) in the presence of Fe^{2+} solution in aq. KCl (0.1 M) solution. Curve in red: 0 mM Fe^{2+} . Curve in black: 10 mM Fe^{2+} .

Cobalt (II)

The CVs in Figure 20 show new peaks after the electro-deposition of Co^{2+} at both CPEs which proves that there is Co^{2+} electro-deposition. A pair of anodic and cathodic peaks in both PCPE and ILCPE was observed, in both electrodes, the peaks were unstable and therefore can say that the electro-deposition was not successful.



(a)



(b)

Figure 20: CVs recorded for PCPE (a) and ILPCP (b) in the presence of Co^{2+} in aq. KCl (0.1 M) solution. Curve in red: 0 mM Co^{2+} solution. Curve in black: 10 mM Co^{2+} solution.

Copper (II)

The CVs in Figure 21 show new peaks after the electro-deposition of Cu^{2+} at both CPEs, which proves that there is Cu^{2+} electro-deposition with similar E_p and I_p values but higher peak widths for ILPCPE. A pair of anodic and cathodic peaks in both PCPE and ILCPE was

observed while the peaks on ILPCPE were unstable, indicates the more efficient the deposition at the ILPCPE.

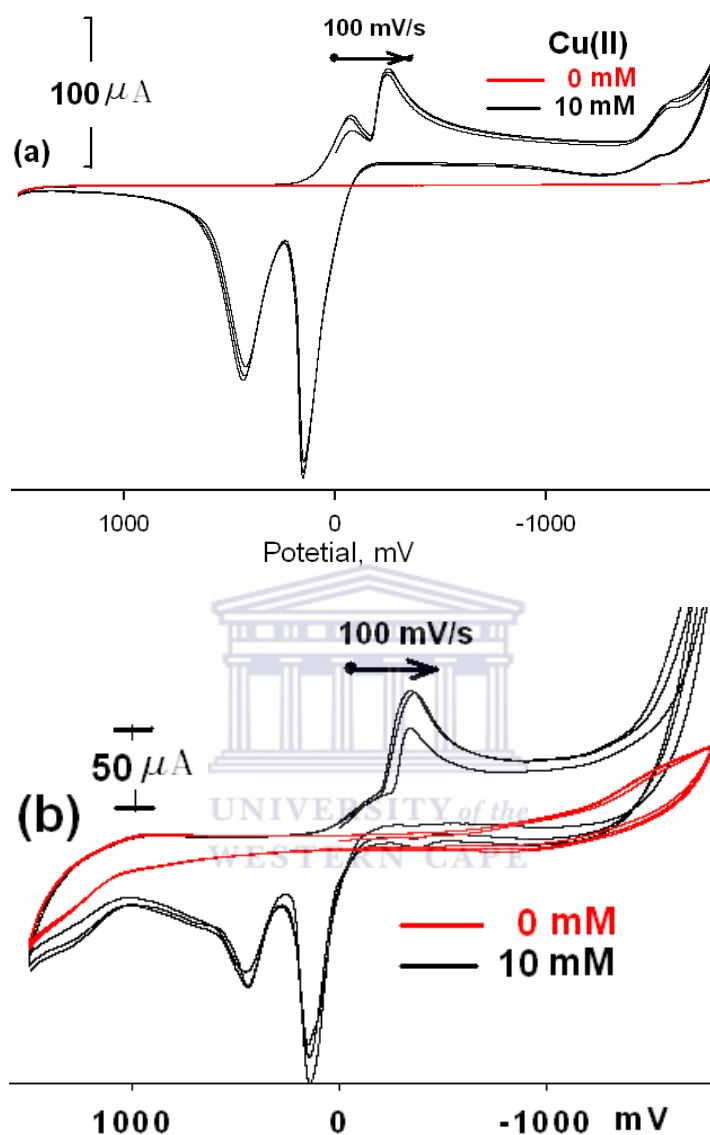


Figure 21: CVs recorded for PCPE (a) and ILPCPE (b) in the presence of Cu^{2+} in aq. KCl (0.1 M) solution. Curve in red: 0 mM Cu^{2+} solution. Curve in black: 10 mM Cu^{2+} solution.

Cerium (II)

The CVs in Figure 22 show new peaks after the electro-deposition of Ce^{2+} at both CPEs which proves that there is Ce^{2+} electro-deposition. One anodic and cathodic peak observed in both PCPE and ILCPE at approximately 1.65 V and 1.7 V respectively, which increased as the successive scans occurs.

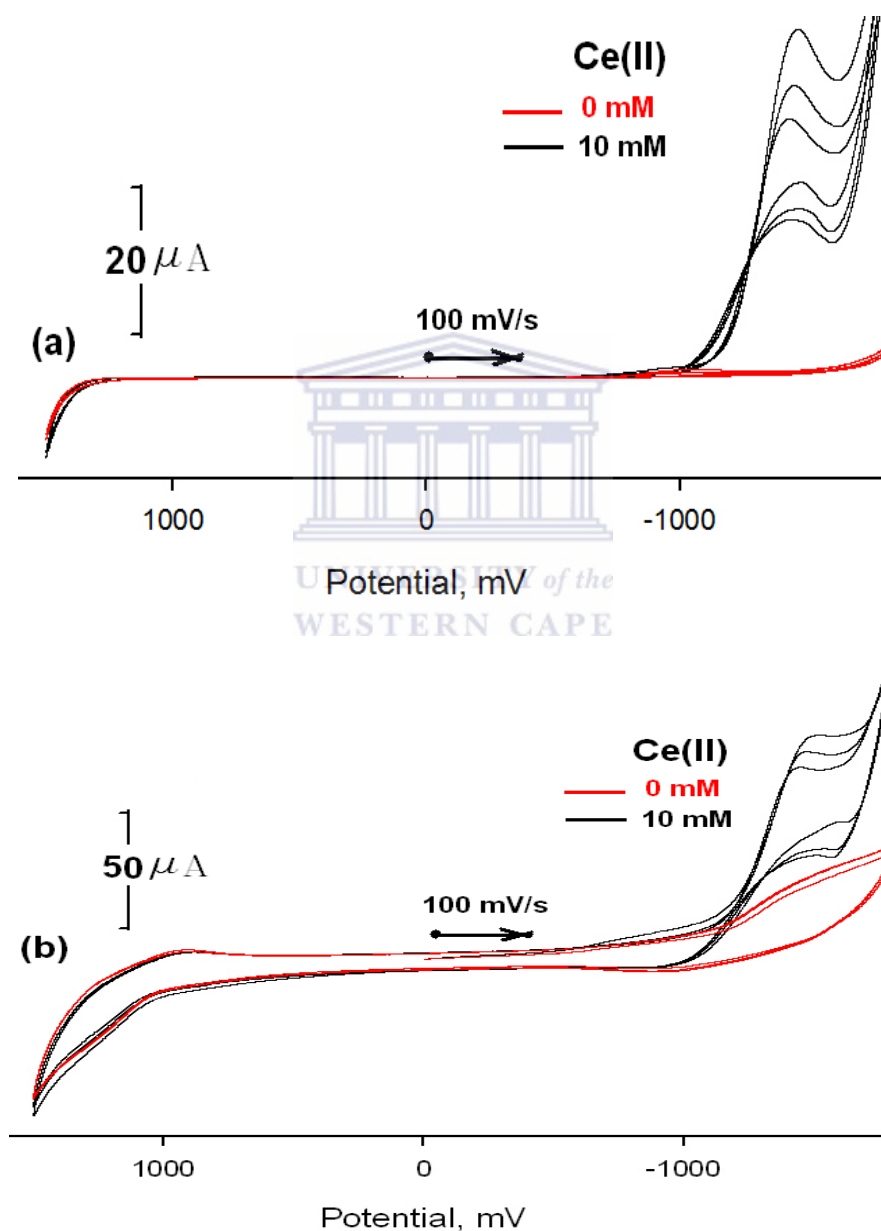


Figure 22: CVs recorded for PCPE (a) and ILPCP (b) in the presence of Ce^{4+} in aq. KCl (0.1 M) solution. Curve in red: 0 mM Ce^{4+} solution. Curve in black: 10 mM Ce^{4+} solution.

Manganese (II)

The CVs in Figure 23 show a pair of anodic and cathodic peaks which were observed at both of the unmodified or PCPE and the ILPCPE on addition of Mn^{2+} solution. But the ILPCPE showed unstable peaks which got lower and lower with successive cyclic scans. On the other hand, these peaks were wider than those observed at the unmodified CPE.

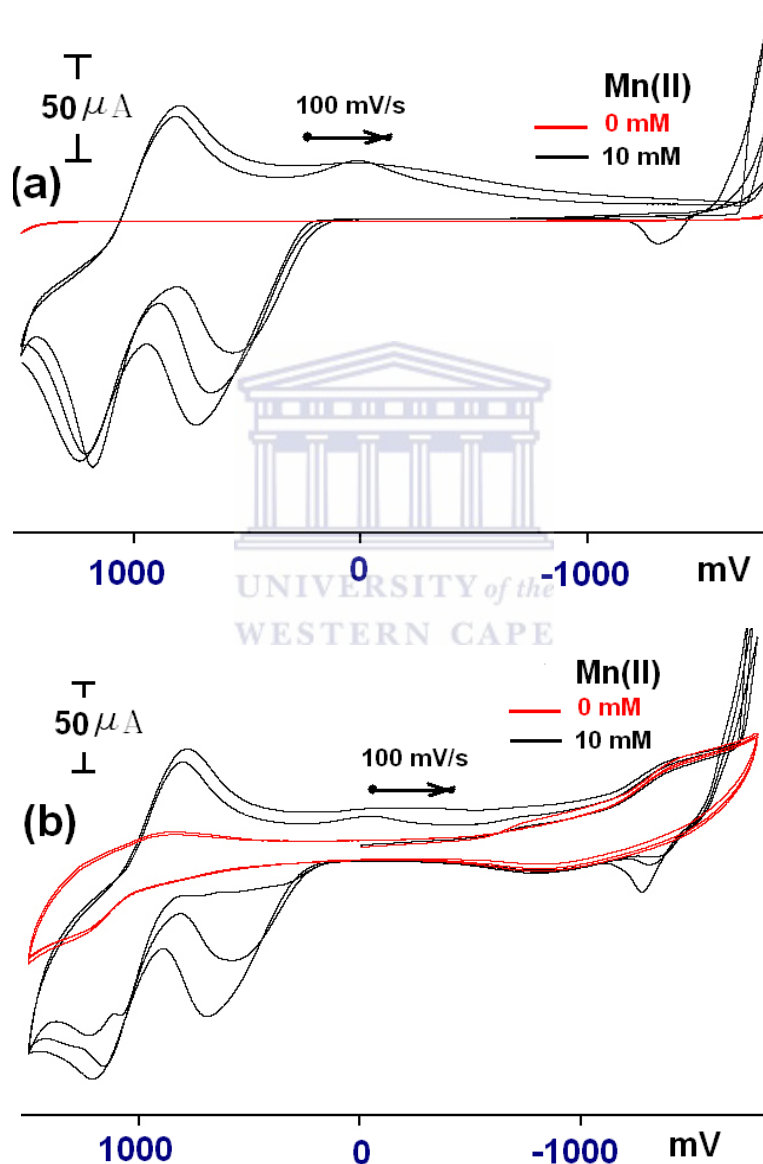


Figure 23: CVs recorded for PCPE (a) and ILPCPE (b) in the presence of Mn^{2+} in aq. KCl (0.1 M) solution. Curve in red: 0 mM Mn^{2+} solution. Curve in black: 10 mM Mn^{2+} solution.

5.3.2 Post-electrodeposition cyclic voltammograms in Aq KCl solution.

Fe_xO_y films

Figures 24 (a) and (b) show overlays of multi-cycle CVs of PCPE (a) and ILPCPE (b) in fresh portions of the electrolyte (aq. KCl, 0.1 M) before (curves in black) and after (curves in red) the Fe²⁺-electrodeposition process. The post-deposition PCPE and ILPCPE respectively exhibited two and four new peaks which were also stable with successive cycles.

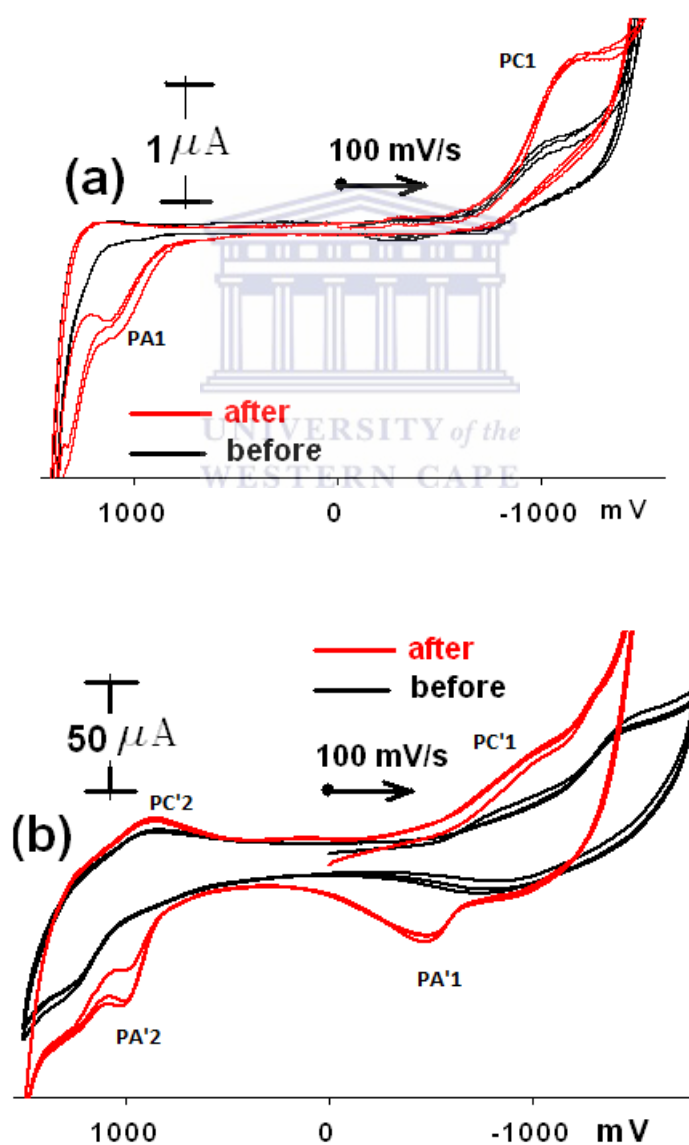


Figure 24: CVs recorded before and after Fe²⁺-electrodeposition at (a) PCPE & (b) ILPCPE

Thus, the post-deposition CVs indicated the surfaces of the electrodes were coated with stable and adherent films of material (Fe_xO_y). The resulting modified CPEs will be referred to as PCPE/ Fe_xO_y and ILPCPE/ Fe_xO_y . The former's peak potentials were -1.2 V (PC1, cathodic) and 1.1 V (PA1, anodic), the latter's were -1.01 V (PC'1, cathodic), 0.8 V (PC'2, cathodic), -0.47 V (PA'1, anodic), and 1 V (PA'2, anodic). Because of the difference between the two electrodes with regard to the positions of the respective peaks, one may say the electrodeposited iron species were different in either of their compositions, phases, structures, or just in the microenvironment.

Co_xO_y films

Figures 25 (a) and (b) show overlays of multi-cycle CVs of PCPE (a) and ILPCPE (b) in fresh portions of the electrolyte (aq. KCl, 0.1 M) before (curves in black) and after (curves in red) the Co^{2+} -electrodeposition process. The post-deposition PCPE and ILPCPE each exhibited four new peaks which were also stable with successive CV cycles. Thus, these post-deposition CVs indicated the surfaces of the electrodes were coated with stable and adherent films of material (Co_xO_y). The resulting modified CPEs will be referred to as PCPE/ Co_xO_y and ILPCPE/ Co_xO_y . The former's peak potentials were -0.50 V (PC1, cathodic), 0.49 V (PA1, anodic), 1.00 V (PC2, cathodic) and 0.490 V, (PC3, cathodic); the latter's were -1.10 V (PC'1, cathodic), -0.25 V (PA'1, anodic), 1.10 V (PA'2, anodic) and 1.10 V (PC'2, cathodic). Because of the difference between the two electrodes with regard to the positions of the respective peaks, one may say the electrodeposited iron species were different in either of their compositions, phases, structures, or just in the microenvironment.

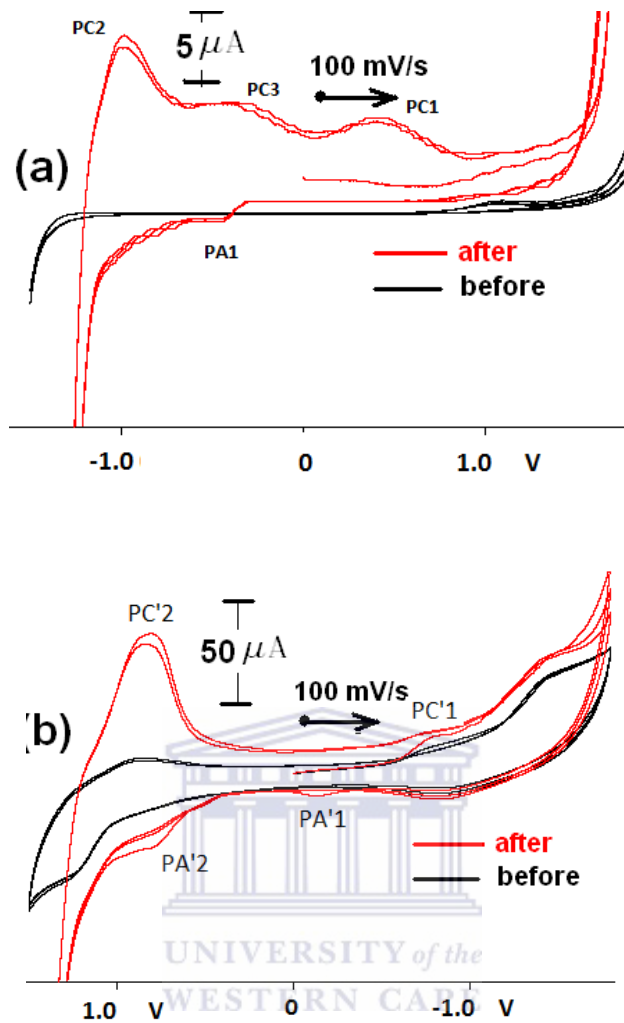


Figure 25: CVs recorded before and after Co^{2+} -electrodeposition at (a) PCPE & (b) ILPCPE

Cu_xO_y films

Figures 26 (a) and (b) show overlays of multi-cycle CVs of PCPE (a) and ILPCPE (b) in fresh portions of the electrolyte (aq. KCl, 0.1 M) before (curves in black) and after (curves in red) the Cu^{2+} -electrodeposition process. While the post-deposition PCPE did exhibit about seven new but unstable peaks, the ILPCPE exhibited none at all. In the former case, the peak heights decreased or diminished with increasing number of CV cycles. These peaks were observed at potentials of -0.49 V (cathodic), 0.60 V (cathodic), -0.30 V (anodic), 0.25 V, (anodic), 0.30 V (anodic), 0.55 V (anodic) and 0.25 V (cathodic). Thus, electrodeposition of

Cu^{2+} occurred only on the PCPE. However, the Cu_xO_y film on the resulting modified-electrode (PCPE/ Cu_xO_y) did not prove to be adherent and stable when observed for three CV cycles.

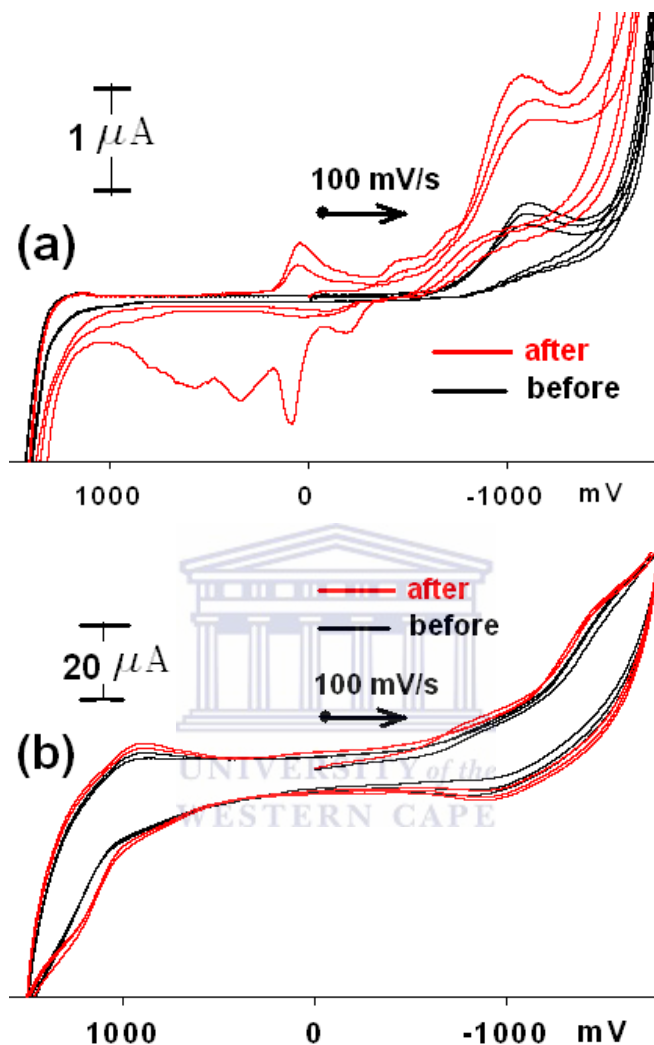


Figure 26: CVs recorded before and after Cu^{2+} -electrodeposition at (a) PCPE & (b) ILPCPE

Ce_xO_y films

Figures 27 (a) and (b) show overlays of multi-cycle CVs of PCPE (a) and ILPCPE (b) in fresh portions of the electrolyte (aq. KCl, 0.1 M solution) before (curves in black) and after (curves in red) the Ce^{4+} -electrodeposition process. Post-electrodeposition CVs of PCPE and ILPCPE did not exhibit any new voltammetric features. This observation supports the

conclusion made earlier based on the CVs of Ce^{4+} that electrodeposition of Ce_xO_y did not occur on both electrodes.

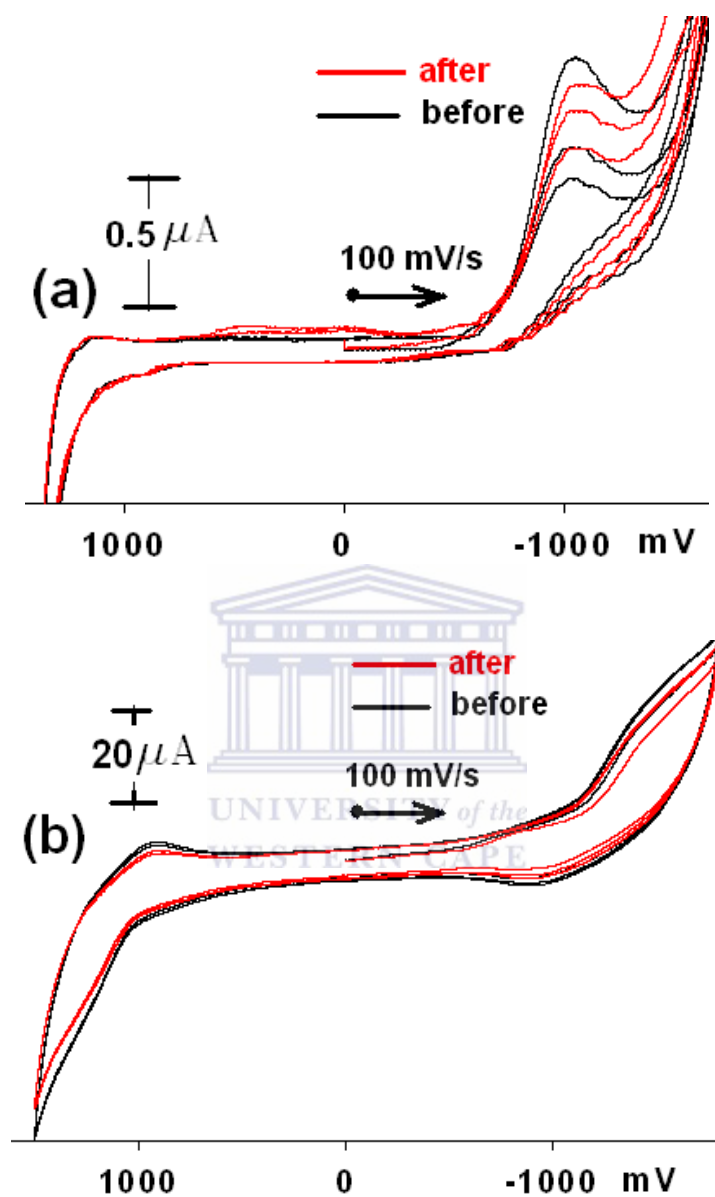


Figure 27: CVs recorded before and after Ce^{2+} -electrodeposition at (a) PCPE & (b) ILPCPE

Mn_xO_y films

Figures 28 (a) and (b) show overlays of multi-cycle CVs of PCPE (a) and ILPCPE (b) in fresh portions of the electrolyte (aq. KCl, 0.1 M solution) before (curves in black) and after (curves in red) the Mn^{2+} -electrodeposition process.

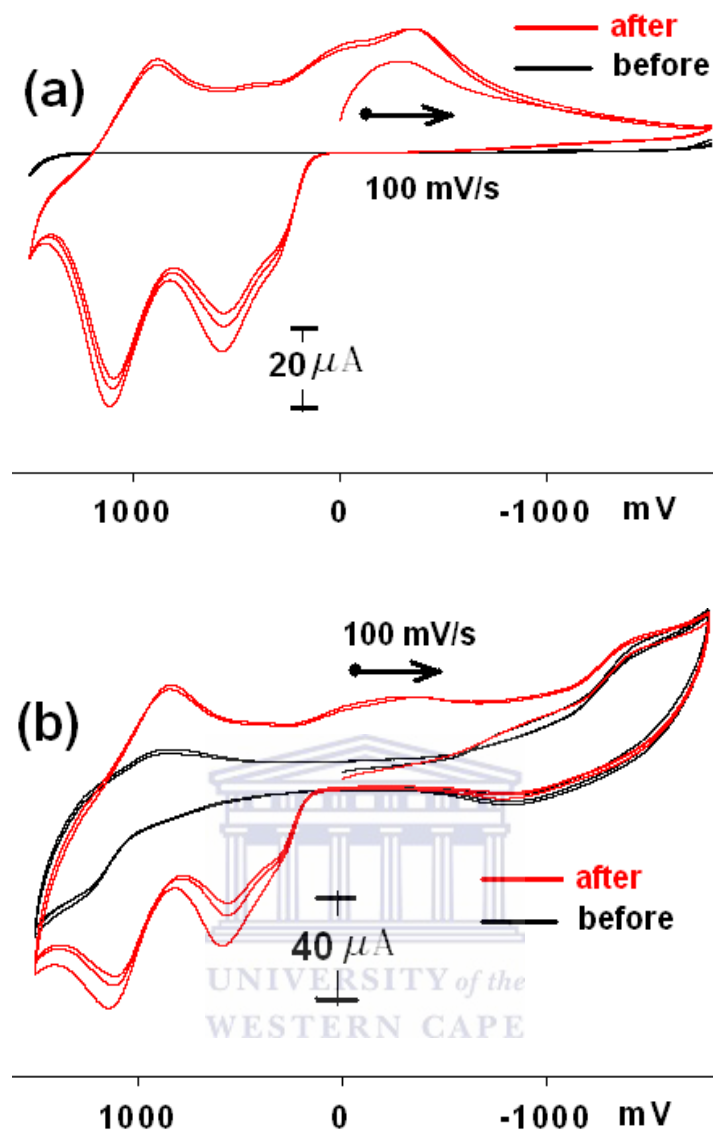


Figure 28: CVs before and after Fe^{2+} -electrodeposition at (a) PCPE & (b) ILPCPE

The post-deposition PCPE and ILPCPE each exhibited four new peaks which were also stable with successive CV cycles. Thus, these post-deposition CVs indicated the surfaces of the electrodes were coated with stable and adherent films of material (Mn_xO_y). The resulting modified CPEs will be referred to as PCPE/ Mn_xO_y and ILPCPE/ Mn_xO_y . The peak potentials in both cases were similar: -0.45 V (cathodic), 0.5 V (anodic), 1.1 V (anodic), and 0.95 V. However, broader and taller peaks were observed in the case of ILPCPE/ Mn_xO_y . Thus, the

deposition of Mn^{2+} at the ILPCPE was more efficient or the resulting Mn_xO_y film was more electroactive. Most probably, this was because of differences in compositions, phases, structures, or just in the microenvironment.

5.3.3 Post-electrodeposition probe with H_2O_2

Fe_xO_y films

The CV curves (in black) in Figure 29(a) and (b) were recorded in a fresh portion of the electrolyte containing H_2O_2 after deposition of Fe^{2+} at the PCPE and ILPCPE, respectively. Both CVs show H_2O_2 reduction (cathodic) peaks with lower over-potentials and increased peak currents relative to the CVs of H_2O_2 before electrodeposition (Figure 13). Thus, these results also confirm that the surfaces of the electrodes were altered during the electrodeposition process forming the modified electrodes: ILPCPE/ Fe_xO_y and PCPE/ Fe_xO_y . H_2O_2 exhibited CVs with similar peak heights and stability at both of the modified-electrodes. However, a lower over-potential H_2O_2 reduction (cathodic peak) was observed for ILPCPE/ Fe_xO_y (-1.1 V) compared to the PCPE/ Fe_xO_y (-1.3 V). Furthermore, unlike the bare electrodes, H_2O_2 oxidation (anodic) peaks were observed this time because of the electrodeposited material in both cases. It exhibited a higher anodic peak height at the ILPCPE/ Fe_xO_y , and a lower anodic peak potential at the ILPCPE/ Fe_xO_y .

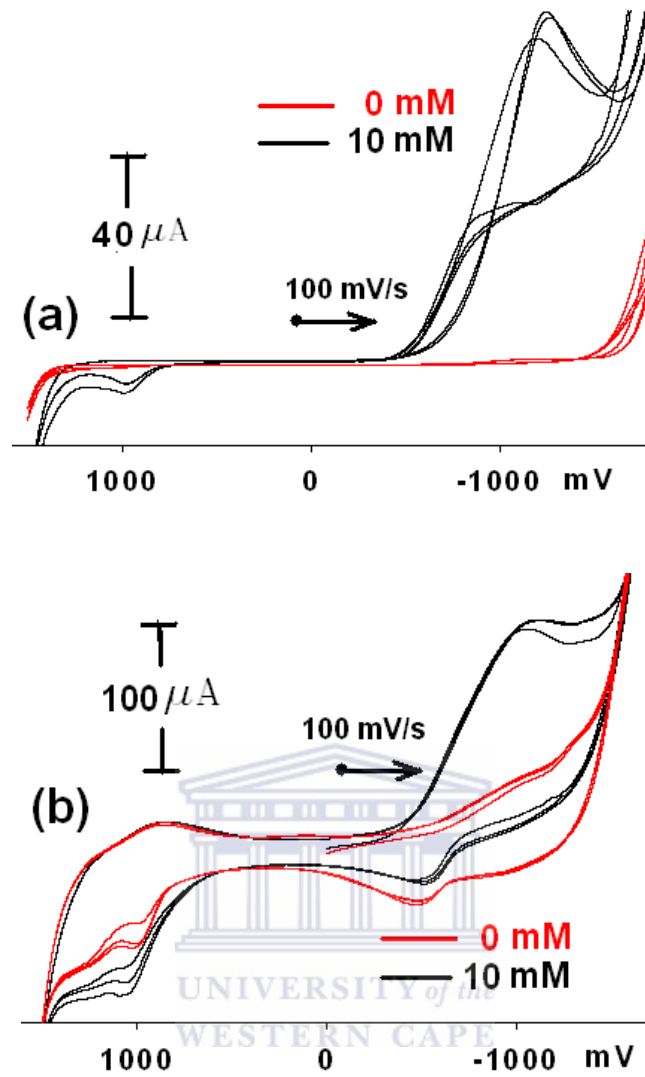


Figure 29: CVs of H_2O_2 at (a) PCPE/ Fe_xO_y and (b) ILPCPE/ Fe_xO_y in aq. KCl

Co_xO_y films

The CV curves (in black) in Figure 30(a) and (b) were recorded in a fresh portion of the electrolyte containing H_2O_2 after deposition of Co^{2+} at the PCPE and ILPCPE, respectively. Unlike its CVs at the corresponding bare electrodes (Figure 13), H_2O_2 exhibited both cathodic and anodic peaks at the resulting Co_xO_y -modified electrodes (PCPE/ Co_xO_y and ILPCPE/ Co_xO_y).

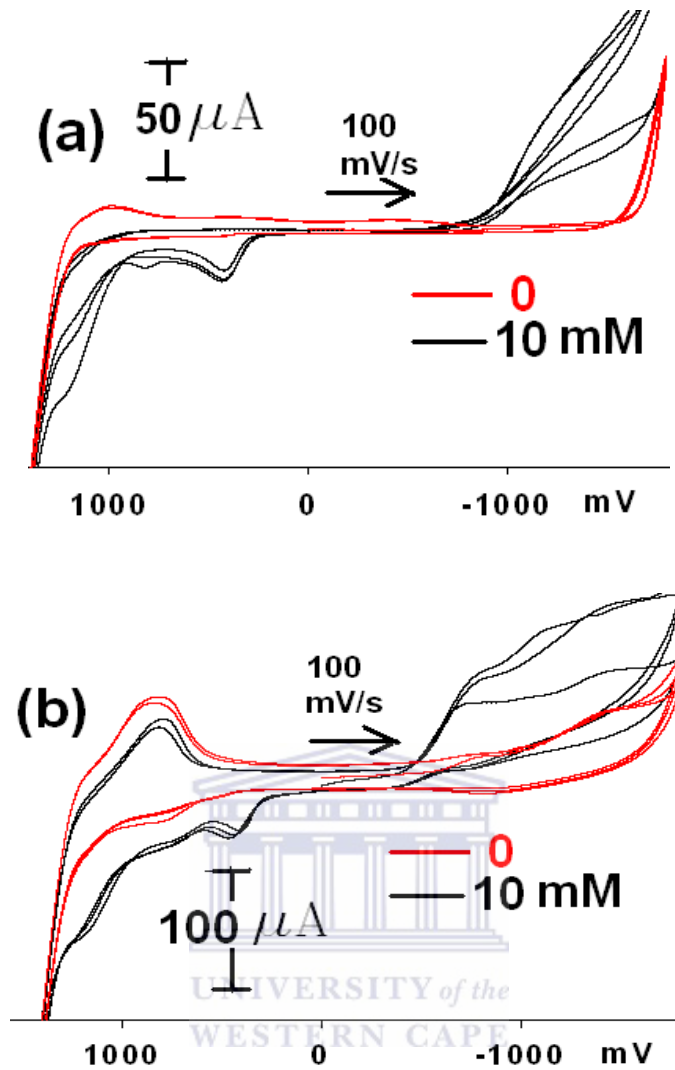


Figure 30: CVs of H_2O_2 at (a) PCPE/ Fe_xO_y and (b) ILPCPE/ Fe_xO_y in aq. KCl

In contrast with the PCPE/ Co_xO_y , a new H_2O_2 -reduction peak was observed for ILPCPE/ Co_xO_y at about -0.75 V and the peak height at -1.4 V almost doubled. Even the anodic peaks potentials were similar; anodic peak height for ILPCPE/ Co_xO_y almost double of that observed at the PCPE/ Co_xO_y .

Cu_xO_y films

The CV curves (in black) in Figure 31 (a) and (b) show the CVs of H_2O_2 in a fresh portion of the electrolyte (aq. KCl, 0.1 M) after attempted electrodeposition of Cu^{2+} at the PCPE and ILPCPE, respectively, to form PCPE/ Cu_xO_y and ILPCPE/ Cu_xO_y . Nevertheless, these CVs of

H₂O₂ did not exhibit any significant difference from its CVs at the freshly prepared electrodes (Figure 13). This confirmed the previous conclusion that electrodeposition of Cu²⁺ not realized.

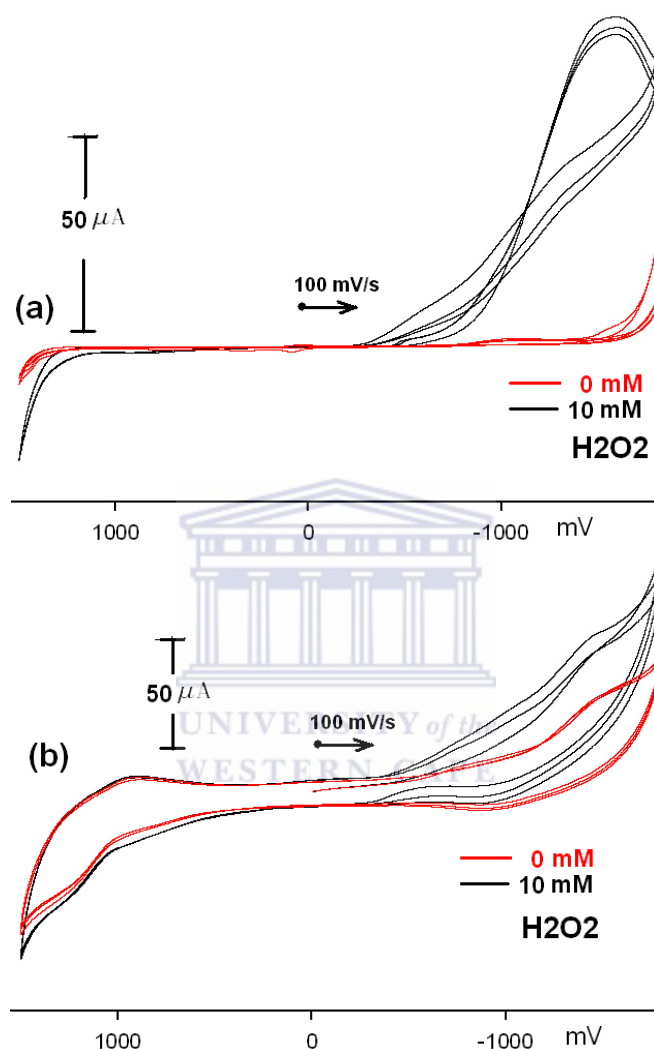


Figure 31: CVs of H₂O₂ at (a) “PCPE/Fe_xO_y“ and (b) “ILPCPE/Fe_xO_y“ in aq. KCl

Ce_xO_y films

The CV curves (in black) in Figure 32 (a) and (b) show the CVs of H₂O₂ in a fresh portion of the electrolyte (aq. KCl. 0.1 M solution) after attempted electrodeposition of Ce²⁺ at the PCPE and ILPCPE, respectively, to form PCPE/Ce_xO_y and ILPCPE/Ce_xO_y. Nevertheless, these CVs of H₂O₂ (black curves) did not exhibit any significant difference from its CVs at

the freshly prepared electrodes. This confirmed the previous conclusion that electrodeposition of Ce^{4+} not realized.

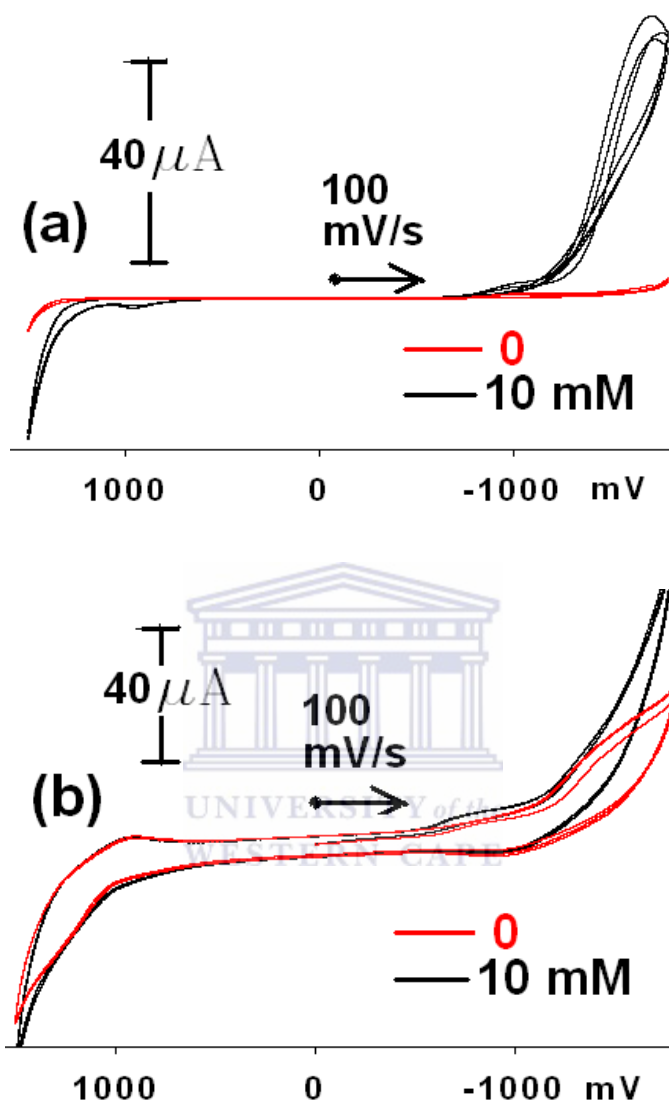


Figure 32: CVs of H_2O_2 at (a) “PCPE/ Ce_xO_y ” and (b) “ILPCPE/ Ce_xO_y ” in aq. KCl (0.1 M) solution.

Mn_xO_y films

The CV curves (in black) in Figure 33 (a) and (b) were recorded in a fresh portion of the electrolyte containing H_2O_2 after deposition of Mn^{2+} at the PCPE and ILPCPE, respectively. It is evident that much higher H_2O_2 -reduction (cathodic) currents were observed in these CVs

than the CVs of H_2O_2 at the corresponding bare electrodes (Figure 13), confirming the deposition of a Mn_xO_y film on both electrodes to form PCPE/ Mn_xO_y and ILPCPE/ Mn_xO_y .

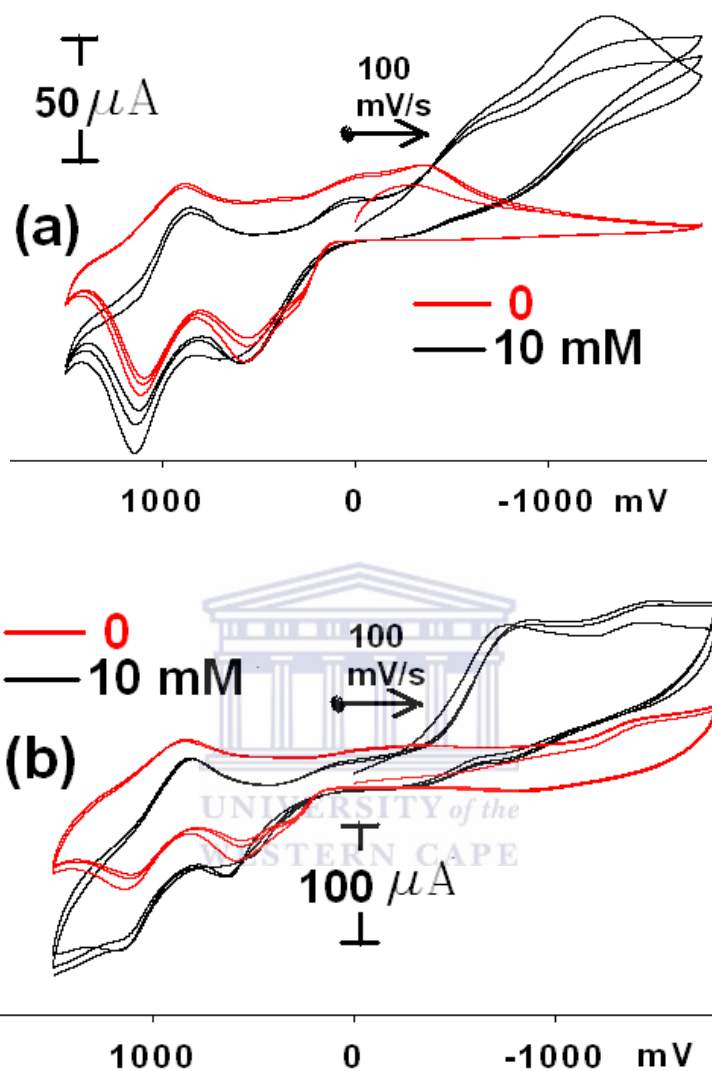


Figure 33: CVs of H_2O_2 at (a) PCPE/ Mn_xO_y and (b) ILPCPE/ Mn_xO_y

No obvious oxidation of H_2O_2 was observed at both of PCPE/ Mn_xO_y and ILPCPE/ Mn_xO_y . Both exhibited similar pattern of H_2O_2 reduction peaks, but in the case of the latter the peak height at 0.75 V was enhanced to prominence. This indicated the reduction of H_2O_2 at ILPCPE/ Mn_xO_y was faster or more efficient.

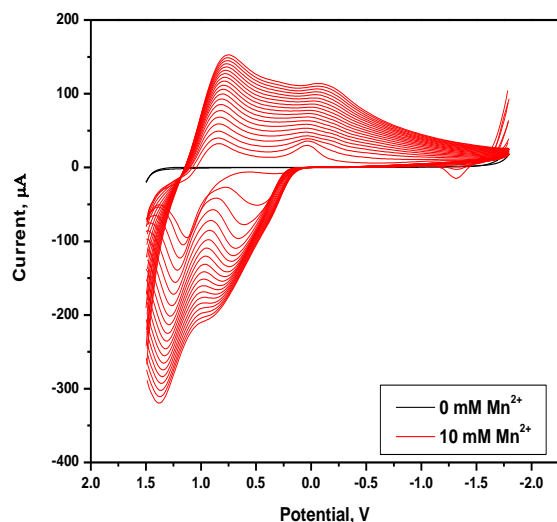
5.4 Effect of Electrolyte Type on Mn_xO_y Electrodeposition

Electro-deposition CVs of Mn^{2+} at the three electrodes ((a) PCPE, (b) ILPCPE, (c) ILCPE) in different aqueous electrolytes (KCl, NaCl, KNO_3 , NH_4Cl , LiCl, NaOAC, and $NaClO_3$), each 0.1 M, are shown from Figures 34 to 40. The potential ranges of study (+1.50 V to -1.80 V), a scan rate of 100 mV s^{-1} , and potential scans of 20 cycles were kept the same for all. The electro-deposition processes were started by an initial anodic scan from 0 V to 1.5 V.

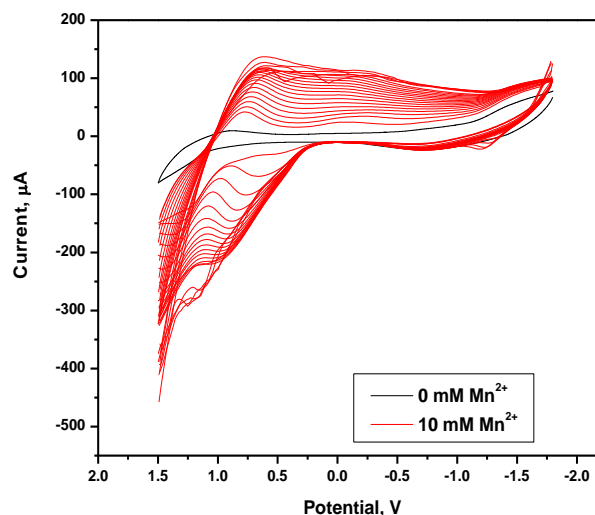
5.4.1 Electrodeposition

Aq. KCl as electrodeposition medium

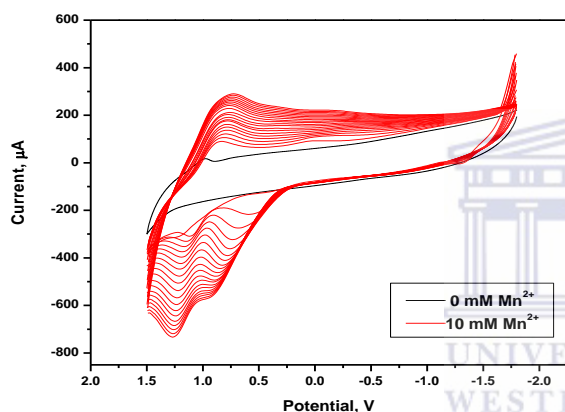
Figures 34a, b, and c show the electrodeposition CVs of Mn^{2+} at PCPE, ILPCPE, and ILCPE, respectively, in aq. KCl (0.1 M) solution. In all cases, two anodic and two cathodic peaks height grew with increasing scan number were observed. This indicated that the Mn^{2+} was successfully deposited at all electrodes. The respective first cycles shows a single anodic process and two cathodic peaks. A second and a lower-potential anodic peak was observed only as of the second cycle, indicating, by then, the surfaces of the electrodes was covered by a new film of material. As the electro-deposition process progressed, the anodic peaks shifted to more positive potentials and the cathodic to more negative potentials. This could be because of the increase in film resistance with the increase of film thickness as more and more layers of Mn_xO_y were deposited. ILCPE and ILPCPE showed wider peaks with higher peak current compared to PCPE.



a)



b)



c)

Figure 34: Multi-cycle CVs of Mn^{2+} at (a) PCPE, (b) ILPCPE, and (c) ILCPE in aq. KCl (0.1 M) solution.

Aq. NaCl as electrodeposition medium

Figures 35a, b, and c show the electrodeposition CVs of Mn^{2+} at PCPE, ILPCPE, and ILCPE, respectively, in aq. NaCl (0.1 M) solution. In all cases, two anodic and two cathodic peaks height grew with increasing scan number were observed. This indicated that the Mn^{2+} was successfully deposited at all electrodes. The respective first cycles shows a single anodic process and two cathodic peaks. A second and a lower-potential anodic peak was observed only as of the second cycle, indicating, by then, the surfaces of the electrodes was covered by a new film of material. As the electro-deposition process progressed, the anodic peaks shifted to more positive potentials and the cathodic to more negative potentials. This could be

because of the increase in film resistance with the increase of film thickness as more and more layers of Mn_xO_y were deposited. ILCPE and ILPCPE showed wider peaks with higher peak current compared to PCPE.

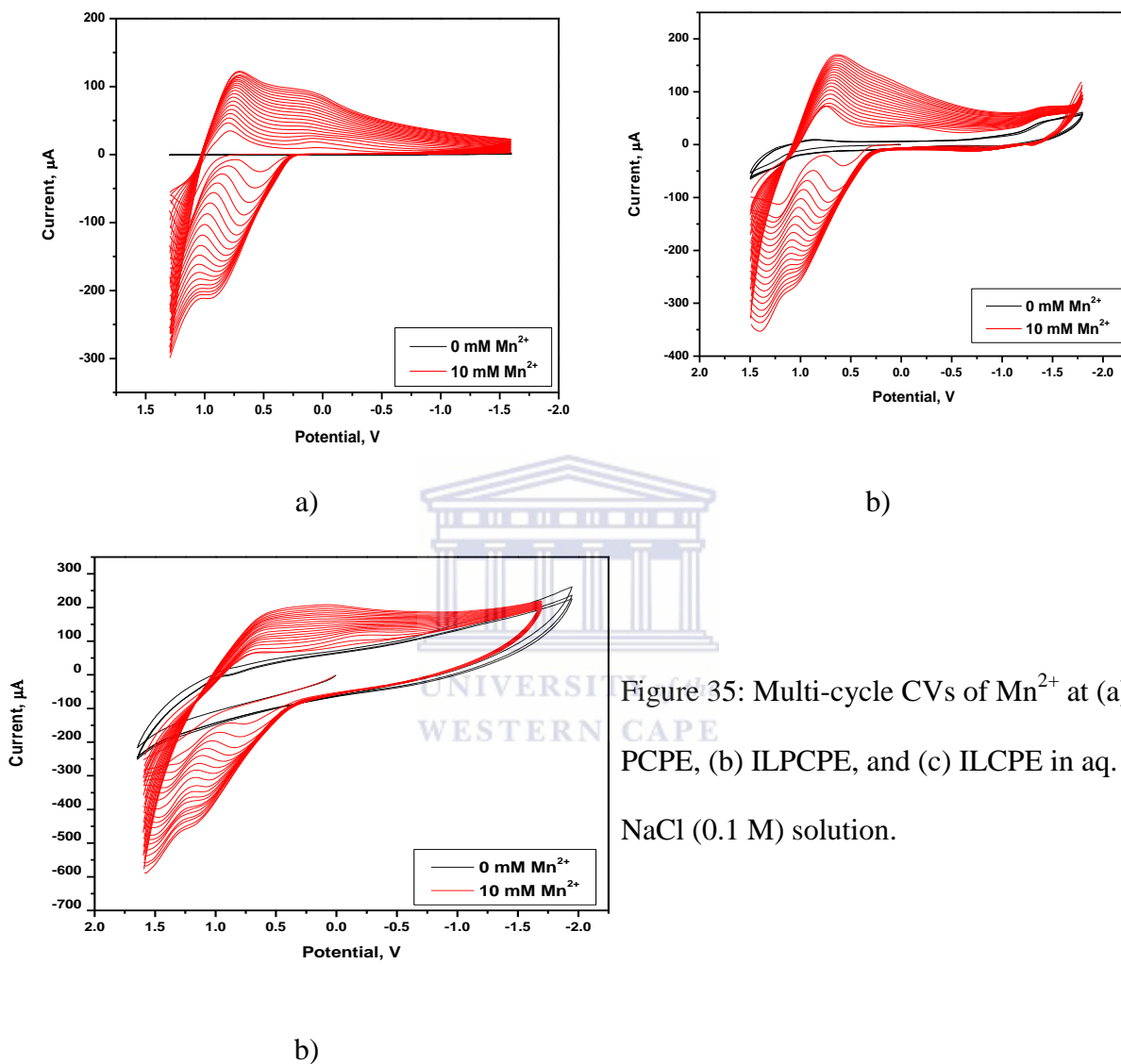


Figure 35: Multi-cycle CVs of Mn^{2+} at (a) PCPE, (b) ILPCPE, and (c) ILCPE in aq. NaCl (0.1 M) solution.

Aq. KNO_3 as electrodeposition medium

Figures 36a, b, and c show the electrodeposition CVs of Mn^{2+} at PCPE, ILPCPE, and ILCPE, respectively, in aq. KNO_3 (0.1 M) solution. In all cases, two anodic and two cathodic peaks height grew with increasing scan number were observed. This indicated that the Mn^{2+} was successfully deposited at all electrodes. The respective first cycles shows a single anodic

process and two cathodic peaks. A second and a lower-potential anodic peak was observed only as of the second cycle, indicating, by then, the surfaces of the electrodes was covered by a new film of material. As the electro-deposition process progressed, the anodic peaks shifted to more positive potentials and the cathodic to more negative potentials. This could be because of the increase in film resistance with the increase of film thickness as more and more layers of Mn_xO_y were deposited. ILCPE and ILPCPE showed wider peaks with higher peak current compared to PCPE.

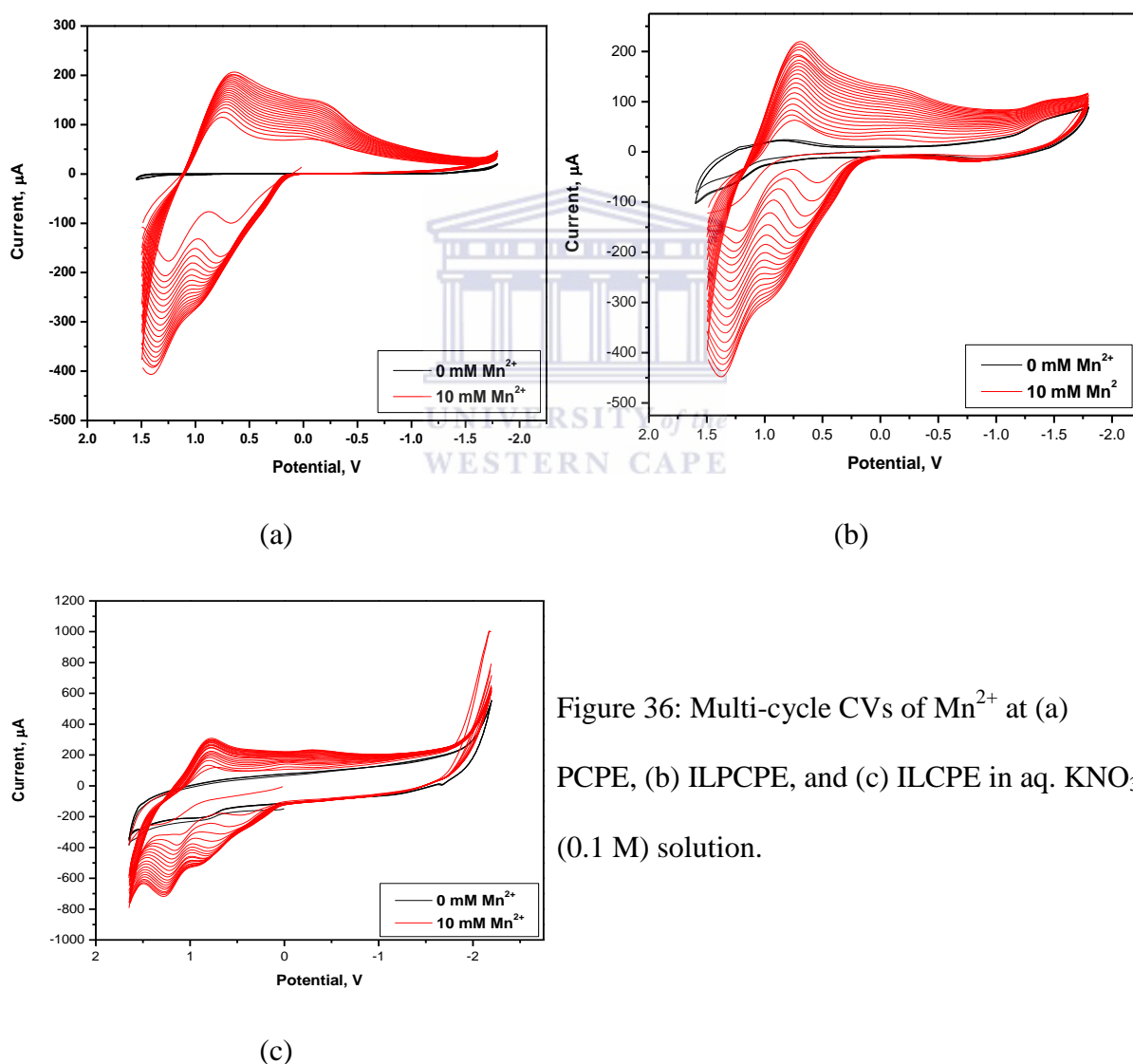


Figure 36: Multi-cycle CVs of Mn^{2+} at (a) PCPE, (b) ILPCPE, and (c) ILCPE in aq. KNO_3 (0.1 M) solution.

Aq. LiCl as electrodeposition medium

Figures 37a, b, and c show the electro-deposition CVs of Mn^{2+} at PCPE, ILPCPE, and ILCPE, respectively, in aq. LiCl (0.1 M) solution. In all cases, two anodic and two cathodic peaks height grew with increasing scan number were observed. This indicated that the Mn^{2+} was successfully deposited at all electrodes.

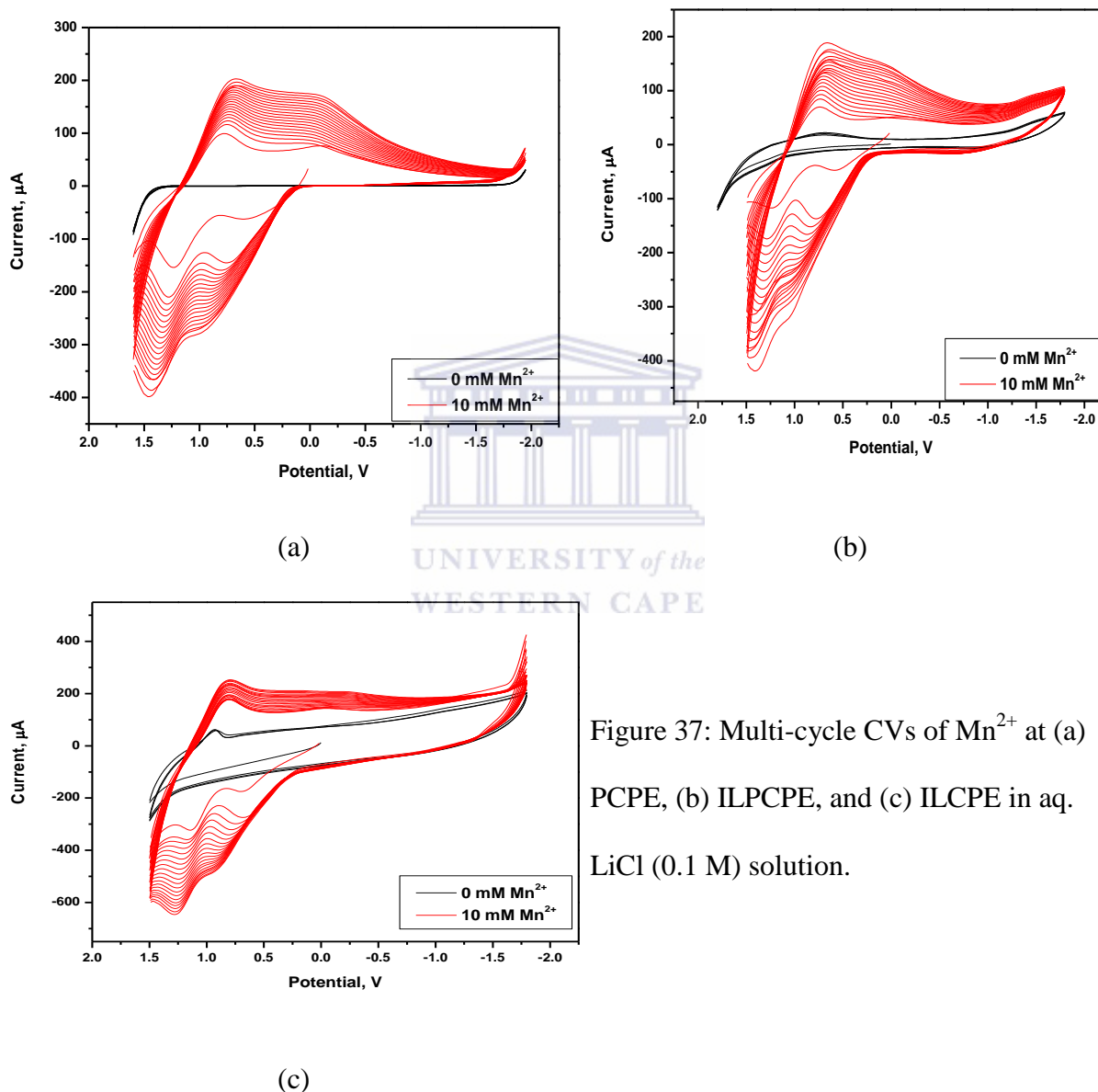


Figure 37: Multi-cycle CVs of Mn^{2+} at (a) PCPE, (b) ILPCPE, and (c) ILCPE in aq. LiCl (0.1 M) solution.

As the electro-deposition process progressed, the anodic peaks shifted to more positive potentials and the cathodic to more negative potentials. This could be because of the increase in film resistance with the increase of film thickness as more and more layers of Mn_xO_y were

deposited. ILCPE and ILPCPE showed wider peaks with higher peak current compared to PCPE.

Aq. NH₄Cl as electro-deposition medium

Figures 38a, b, and c show the electro-deposition CVs of Mn²⁺ at PCPE, ILPCPE, and ILCPE, respectively, in aq. NH₄Cl (0.1 M) solution. In all cases, two anodic and two cathodic peaks height grew with increasing scan number were observed. This indicated that the Mn²⁺ was successfully deposited at all electrodes.

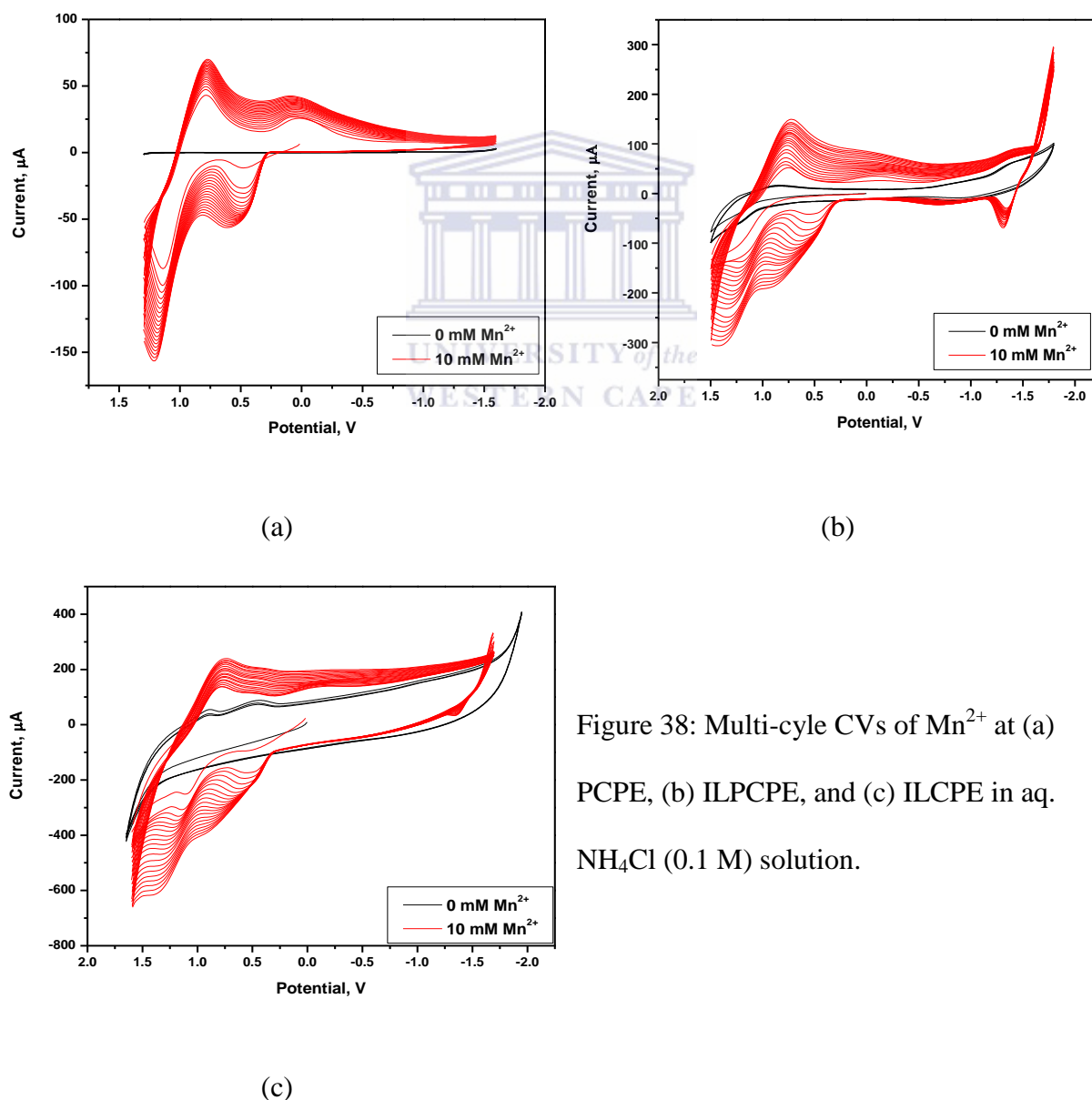


Figure 38: Multi-cycle CVs of Mn²⁺ at (a) PCPE, (b) ILPCPE, and (c) ILCPE in aq. NH₄Cl (0.1 M) solution.

As the electro-deposition process progressed, the anodic peaks shifted to more positive potentials and the cathodic to more negative potentials. This could be because of the increase in film resistance with the increase of film thickness as more and more layers of Mn_xO_y were deposited. ILCPE and ILPCPE showed wider peaks with higher peak current compared to PCPE.

Aq. NaOAc as electrodeposition medium

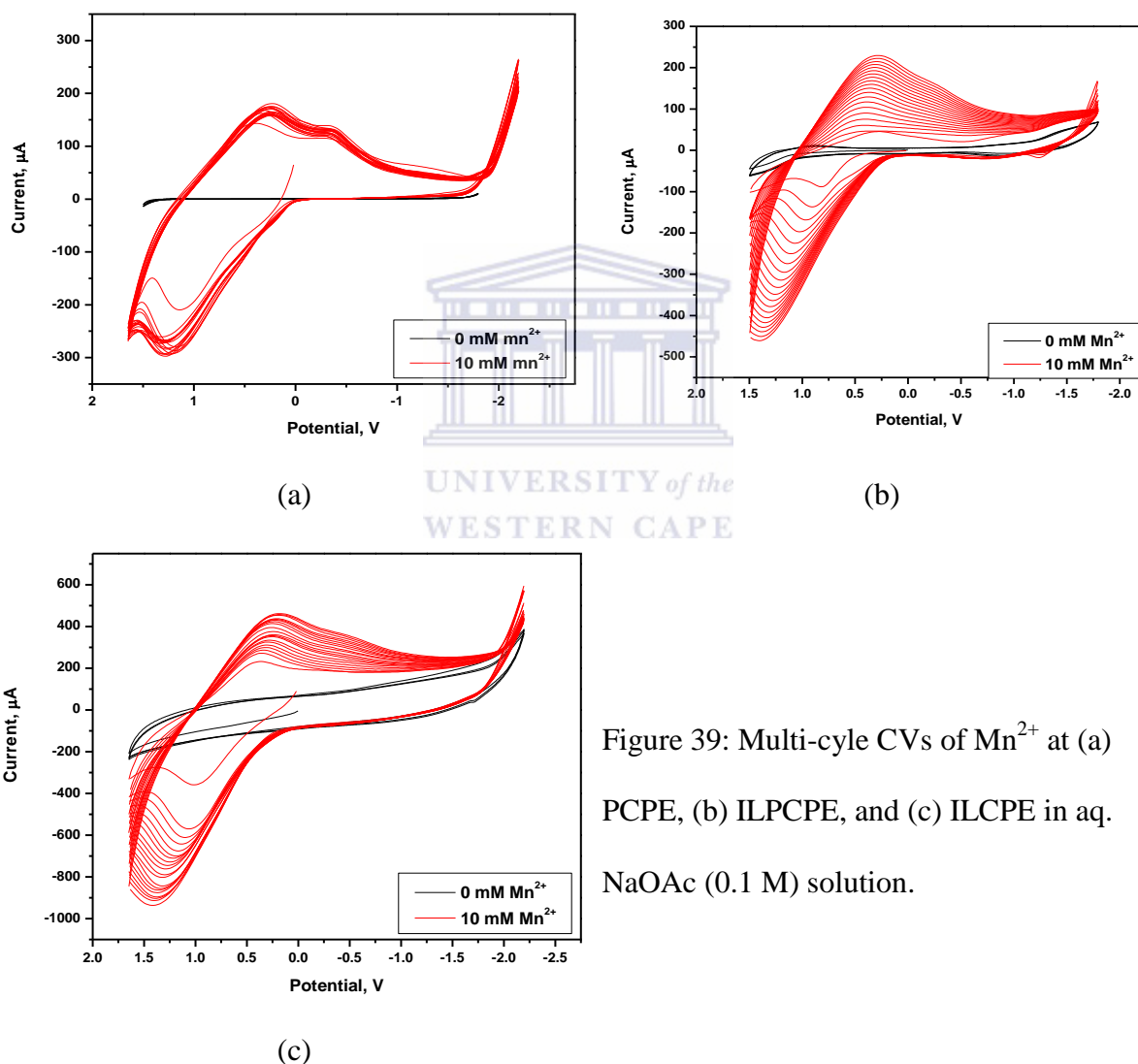


Figure 39: Multi-cycle CVs of Mn^{2+} at (a) PCPE, (b) ILPCPE, and (c) ILCPE in aq. NaOAc (0.1 M) solution.

Figures 39a, b, and c show the electro-deposition CVs of Mn^{2+} at PCPE, ILPCPE, and ILCPE, respectively, in aq. NaOAc (0.1 M) solution. In all cases, an anodic peak and two cathodic peaks height grew with increasing scan number were observed. This indicated that

the Mn^{2+} was successfully deposited at all electrodes. As the electro-deposition process progressed, the anodic peaks shifted to more positive potentials and the cathodic to more negative potentials. This could be because of the increase in film resistance with the increase of film thickness as more and more layers of Mn_xO_y were deposited. ILCPE and ILPCPE showed wider peaks with higher peak current compared to PCPE

Aq. NaClO_3 as electrodeposition medium

Figures 40a, b, and c show the electro-deposition CVs of Mn^{2+} at PCPE, ILPCPE, and ILCPE, respectively, in aq. NaClO_3 (0.1 M) solution.

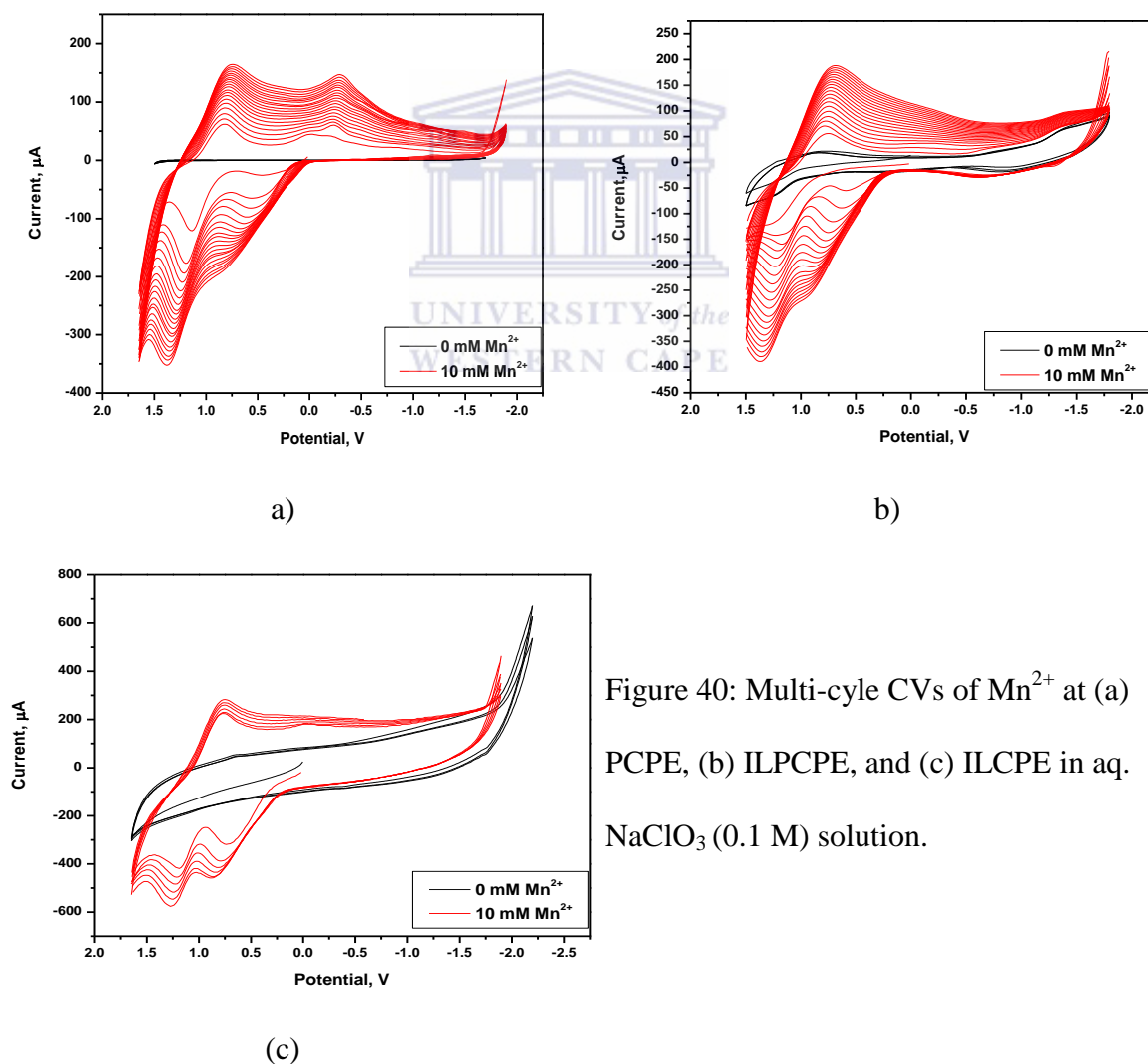
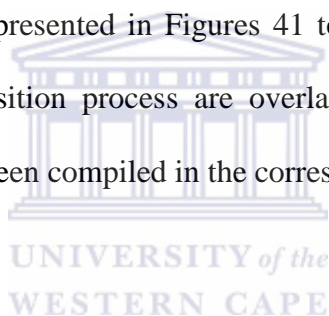


Figure 40: Multi-cycle CVs of Mn^{2+} at (a) PCPE, (b) ILPCPE, and (c) ILCPE in aq. NaClO_3 (0.1 M) solution.

In all cases, two anodic and two cathodic peaks which grew with increasing scan number were observed. This indicated that the Mn^{2+} was successfully deposited at all electrodes. As the electro-deposition process progressed, the anodic peaks shifted to more positive potentials and the cathodic to more negative potentials. This could be because of the increase in film resistance with the increase of film thickness as more and more layers of Mn_xO_y were deposited. ILCPE and ILPCPE showed wider peaks with higher peak current compared to PCPE.

5.4.2 Post-electro-deposition CVs in fresh Mn^{2+} solution-free electrolytes

Post-electrodeposition CVs of different electrodes (a) PCP, (b) ILPCP, and (c) ILCP and in different electrolytes have been presented in Figures 41 to 47. The respective control CVs recorded before the electrodeposition process are overlaid as shown in the figure. Peak potentials and current have also been compiled in the corresponding tables.



Aq. KCl solution as electrolyte

The CVs Mn_xO_y -modified electrodes in fresh aq. KCl (0.1 M) solution are presented in Figure 41. Its peak potential and anodic peak current data are compiled in Table 5. Comparing the pre- and post-electrodeposition CVs, one can conclude that the deposition of Mn_xO_y on the surfaces of the PCPE and ILPCPE was successful, while it wasn't as significant for the ILCPE. In the case of the ILCPE, the difference between these CVs was not as significant indicating a much smaller extent of deposition. PCPE/ Mn_xO_y exhibited two major anodic peaks and two major cathodic peaks. Eventhough the peaks of ILPCPE/ Mn_xO_y were broad and less resolved, the same number peaks as PCPE/ Mn_xO_y were evident. The potentials of the peaks of ILPCPE/ Mn_xO_y and ILCPE/ Mn_xO_y were shifted to higher potentials as a result of which only one of the two anodic peaks were observed in potential

range investigated. Nevertheless, based on comparison of the anodic peaks heights, the largest amount of Mn_xO_y was deposited on the ILPCPE, the next at PCPE.

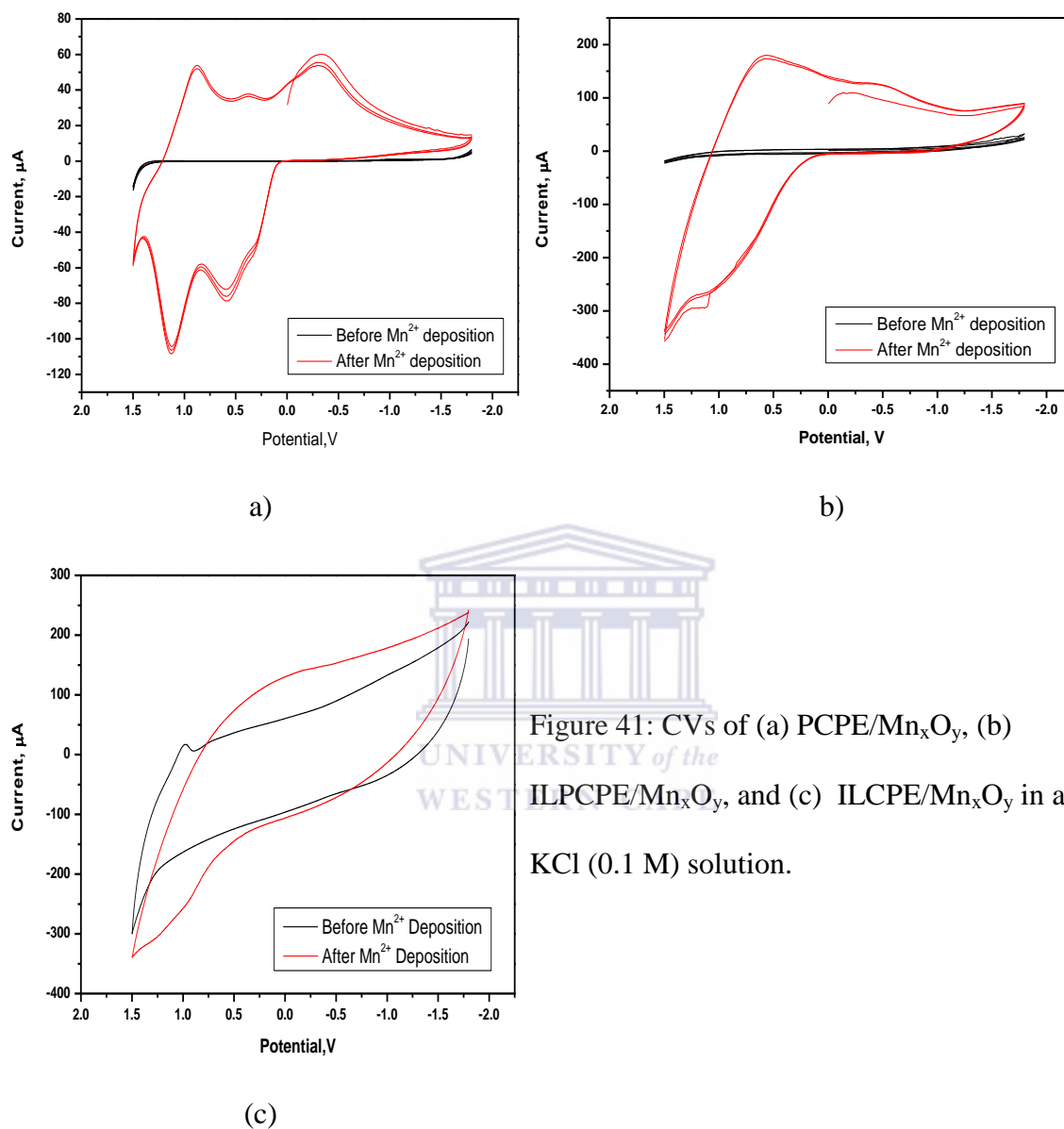


Figure 41: CVs of (a) PCPE/ Mn_xO_y , (b) ILPCPE/ Mn_xO_y , and (c) ILCPE/ Mn_xO_y in aq. KCl (0.1 M) solution.

Table 5: Values of E_{pa} , E_{pc} , and I_{pa} of Mn_xO_y films formed in aq. KCl (0.1 M) solution.

Electrode	E_{pa-I}/V	E_{pa-II}/V	E_{pc-I}/V	E_{pc-II}/V	E_{pc-III}/V	$I_{pa-I}/\mu A$	$I_{pa-II}/\mu A$
PCPE/ Mn_xO_y	0.5776	1.132	0.8786	0.356	-0.3326	-79.40	-108.1
ILPCPE/ Mn_xO_y	-	1.1043	0.5694	-0.5157	-	-	-260.3
ILCPE/ Mn_xO_y	-	0.9674	-	-	-	-	-75.10

Aq. NaCl solution as electrolyte

The CVs Mn_xO_y -modified electrodes in fresh aq. NaCl (0.1 M) solution are presented in Figure 42. Its peak potential and anodic peak current data are compiled in Table 6.

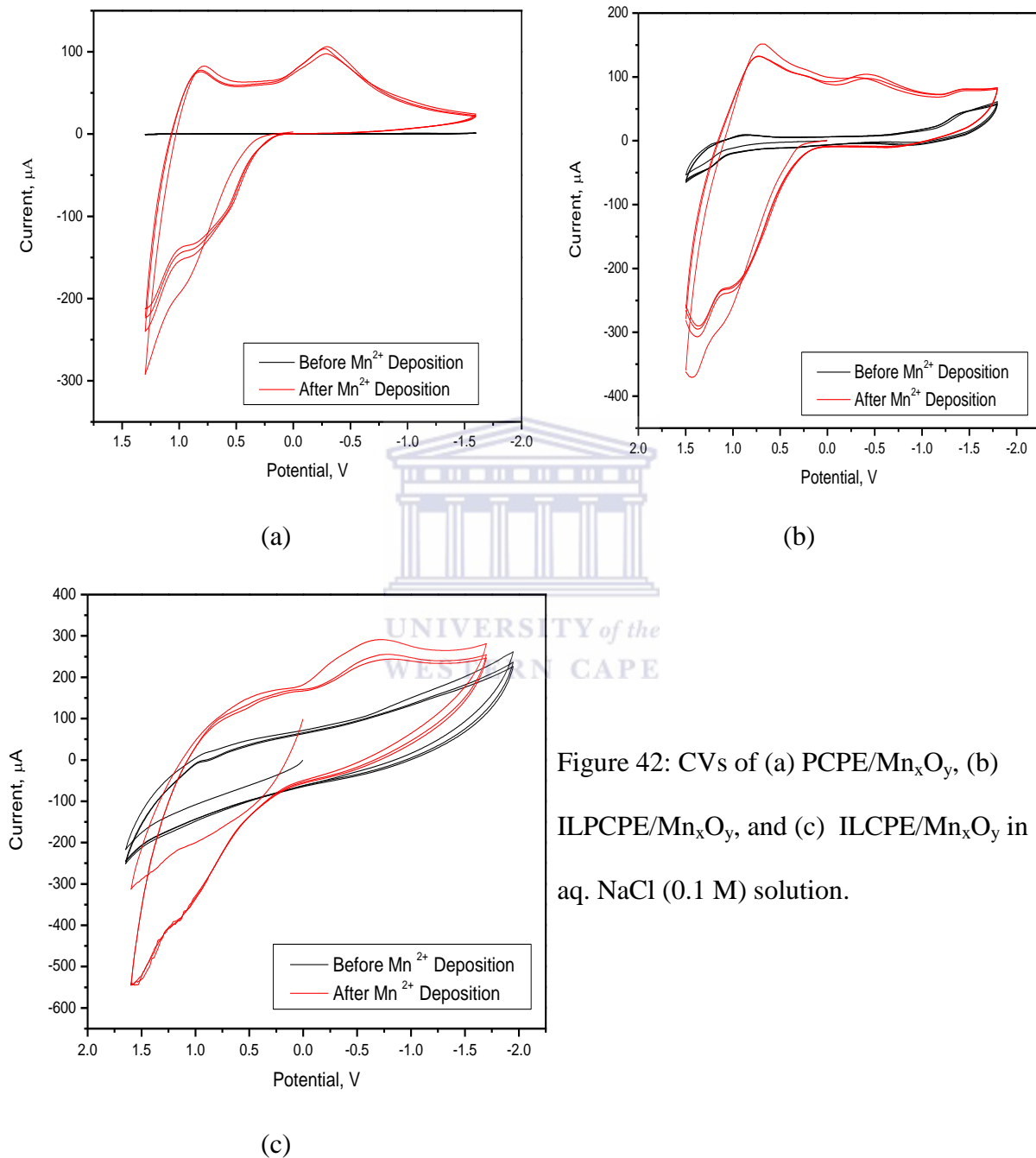


Figure 42: CVs of (a) PCPE/ Mn_xO_y , (b) ILPCPE/ Mn_xO_y , and (c) ILCPE/ Mn_xO_y in aq. NaCl (0.1 M) solution.

Comparing the pre- and post-electrodeposition CVs, one can conclude that the deposition of Mn_xO_y on all electrodes was successful. Two pairs of anodic and cathodic peaks were evident in each case. However, in the case of ILPCPE/ Mn_xO_y and ILCPE/ Mn_xO_y the respective higher-

overpotential anodic peaks lied outside the scan range. The peaks of these were also broader and less resolved. The potentials of the peaks of ILPCPE/Mn_xO_y and ILCPE/ Mn_xO_y were shifted to higher potentials as a result of which only one of the two anodic peaks were observed in potential range investigated. Nevertheless, based on comparison of the anodic peaks heights, the largest amount of Mn_xO_y was deposited on the ILPCPE, the next at ILCPE.

Table 6: Values of E_{pa} , E_{pc} , and I_{pa} of Mn_xO_y films formed in aq. NaCl as measured in fresh aq. NaCl (0.1 M) solution.

Electrode	E_{pa-I}/V	E_{pa-II}/V	E_{pc-I}/V	E_{pc-II}/V	$I_{pa-I}/\mu A$	$I_{pa-II}/\mu A$
PCPE/Mn _x O _y	0.532	0.875	0.822	-0.271	-87.9	-148
ILPCPE/Mn _x O _y	0.999	1.38	0.739	-0.434	-228	-300
ILCPE/Mn _x O _y	1.14	-	0.140	-0.721	-248	-

Aq. KNO₃ solution as electrolyte

The CVs Mn_xO_y-modified electrodes in fresh aq. KNO₃ (0.1 M) solution are presented in Figure 43. Its peak potential and anodic peak current data are compiled in Table 7. Comparing the pre- and post-electrodeposition CVs, one can conclude that the deposition of Mn_xO_y on all electrodes was successful. Two pairs of stable anodic and cathodic peaks which remained stable were evident, indicating the formation adherent films regardless of the electrode. The peaks also well resolved in each case. The peaks were observed at higher and higher potentials when going from left to right in the order PCPE/Mn_xO_y < ILPCPE/Mn_xO_y < ILCPE/Mn_xO_y. Nevertheless, based on comparison of the anodic peaks heights, the largest amount of Mn_xO_y was deposited on the ILPCPE, while there appeared to be no difference between PCPE/Mn_xO_y and ILCPE/ Mn_xO_y in this regard.

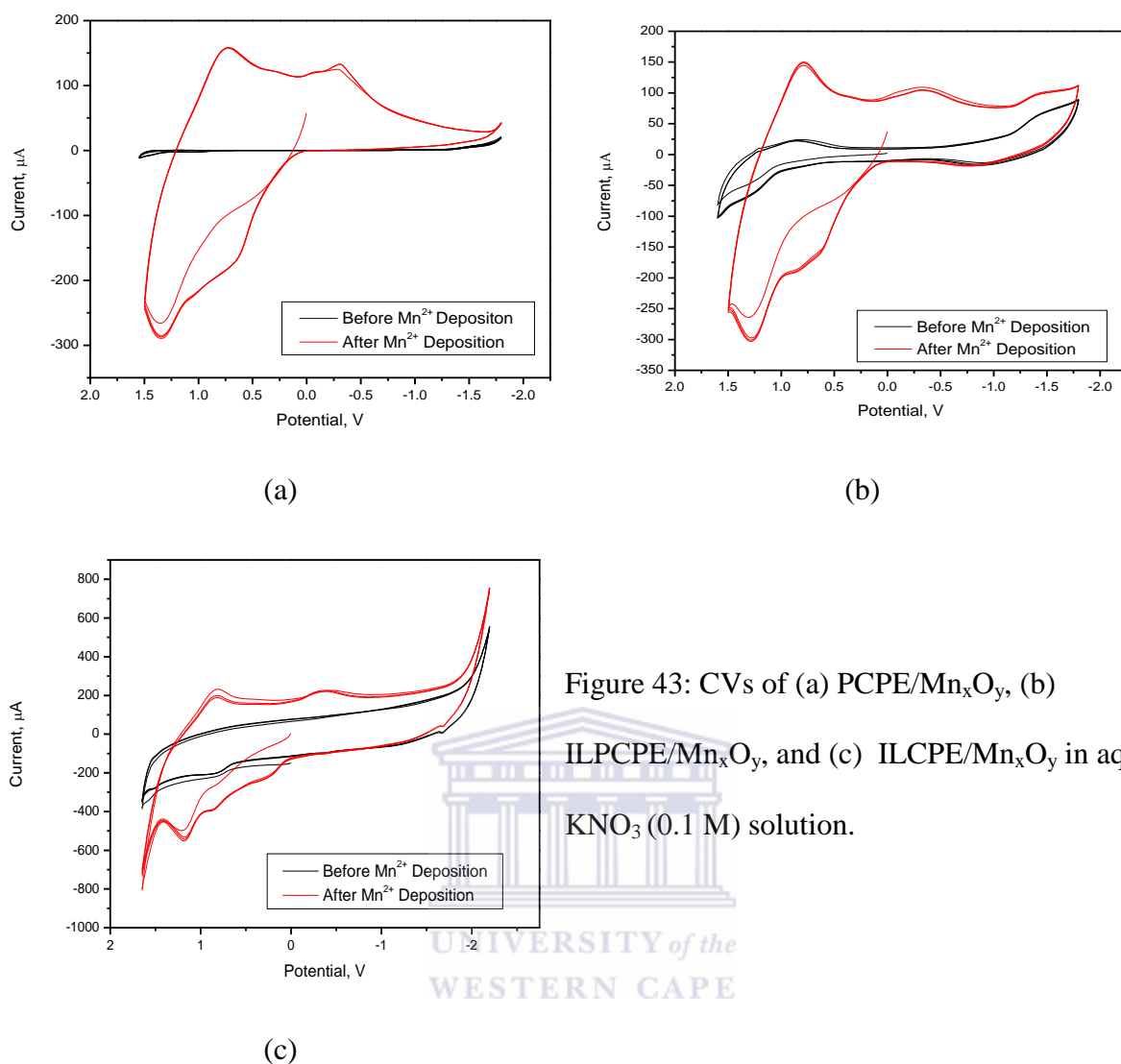


Figure 43: CVs of (a) PCPE/Mn_xO_y, (b) ILPCPE/Mn_xO_y, and (c) ILCPE/Mn_xO_y in aq. KNO₃ (0.1 M) solution.

Table 7: Postdeposition E_{pa} , E_{pc} , and I_{pa} values of Mn_xO_y films in aq. KNO₃ (0.1 M) solution.

Electrode	E_{pa-I} / V	E_{pa-II} / V	E_{pc-I} / V	E_{pc-II} / V	I_{pa-I} / μA	I_{pa-II} / μA
PCPE/Mn _x O _y	0.637	1.35	0.729	0.290	-165	-288
ILPCPE/Mn _x O _y	0.856	1.29	0.790	-0.342	-180	-376
ILCPE/Mn _x O _y	0.873	1.18	0.797	-0.391	-199	-290

Aq. LiCl solution as electrolyte

The CVs Mn_xO_y-modified electrodes in fresh portion of aq. LiCl (0.1 M) solution are presented in Figure 44. Its peak potential and anodic peak current data are compiled in Table 8. Comparing the pre- and post-electrodeposition CVs, one can conclude that the deposition of

Mn_xO_y on all electrodes was successful. Two pairs of stable anodic and cathodic peaks which remained stable were evident, indicating the formation adherent films regardless of the electrode type. The peaks also well resolved in each case, except for the two cathodic peaks of ILPCPE. The peaks were observed at higher and higher potentials when going from left to right in the order ILCPE/ Mn_xO_y < PCPE/ Mn_xO_y < ILPCPE/ Mn_xO_y . Nevertheless, based on comparison of the anodic peak heights, no significant difference was observed between them with regard to the amount of Mn_xO_y deposited.

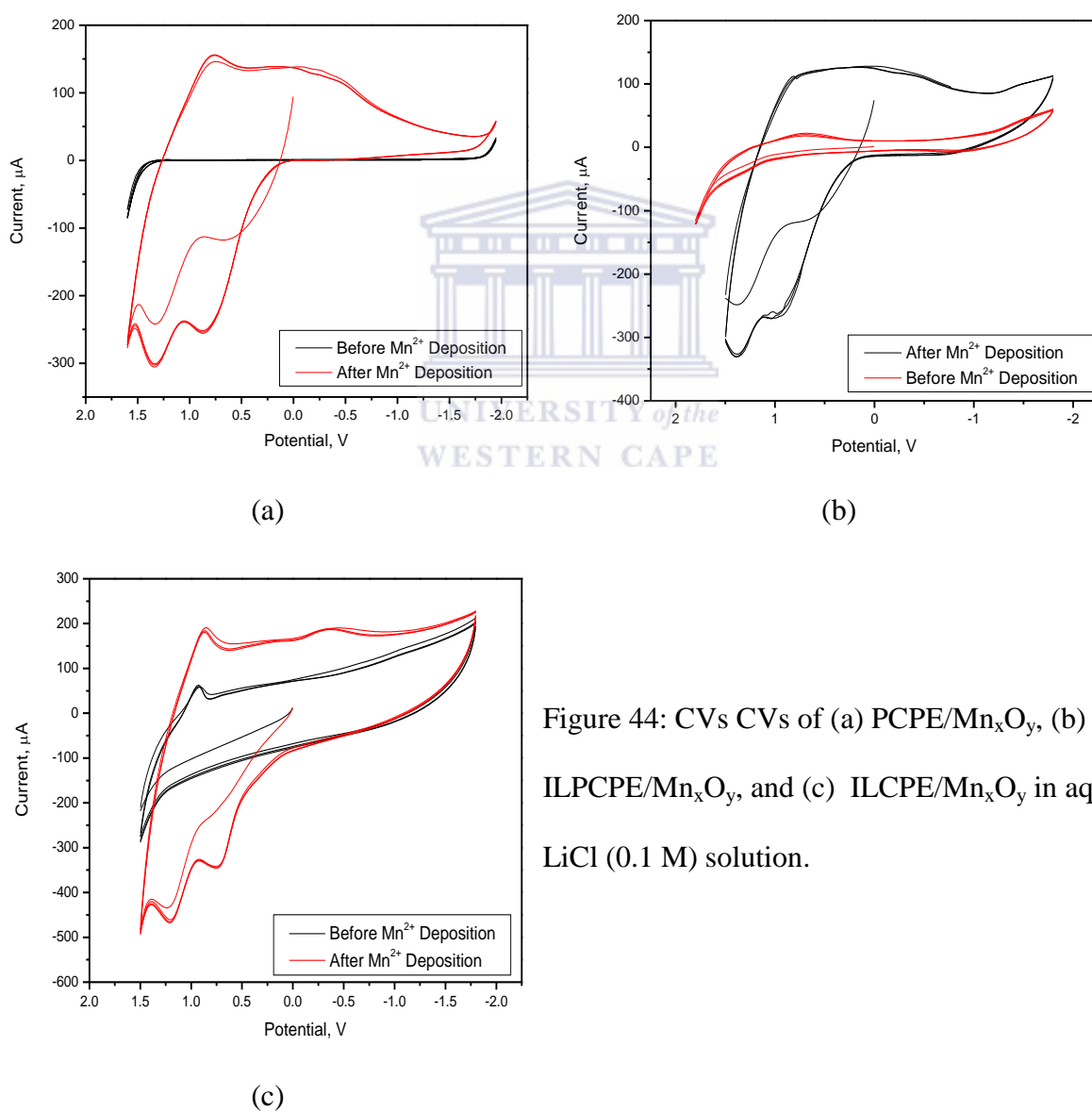


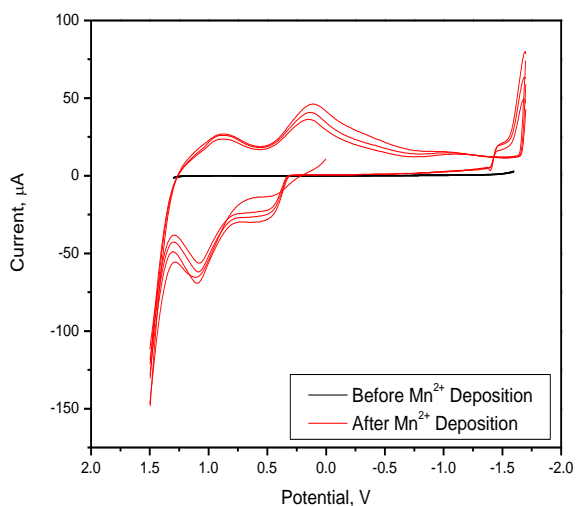
Figure 44: CVs CVs of (a) PCPE/ Mn_xO_y , (b) ILPCPE/ Mn_xO_y , and (c) ILCPE/ Mn_xO_y in aq. LiCl (0.1 M) solution.

Table 8: Postdeposition E_{pa} , E_{pc} , and I_{pa} values of Mn_xO_y films aq. LiCl (0.1 M) solution.

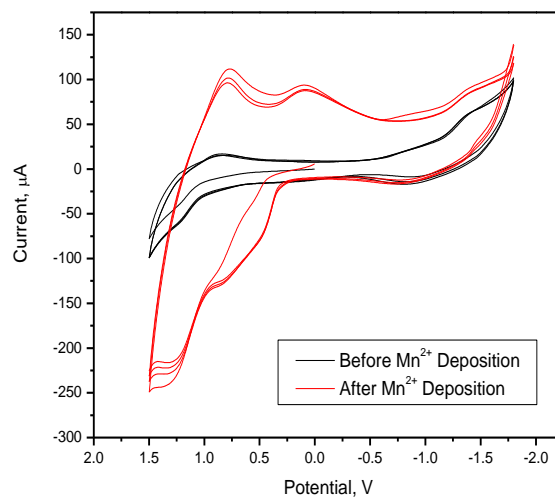
Electrode	E_{pa-I} / V	E_{pa-II} / V	E_{pc-I} / V	E_{pc-II} / V	I_{pa-I} / μA	I_{pa-II} / μA
PCPE/ Mn_xO_y	0.865	1.35	0.763	0.031	-258	-304
ILPCPE/ Mn_xO_y	0.951	1.40	-	-0.381	-243	-307
ILCPE/ Mn_xO_y	0.739	1.19	0.233	-0.349	-233	-322

Aq. NH_4Cl solution as electrolyte

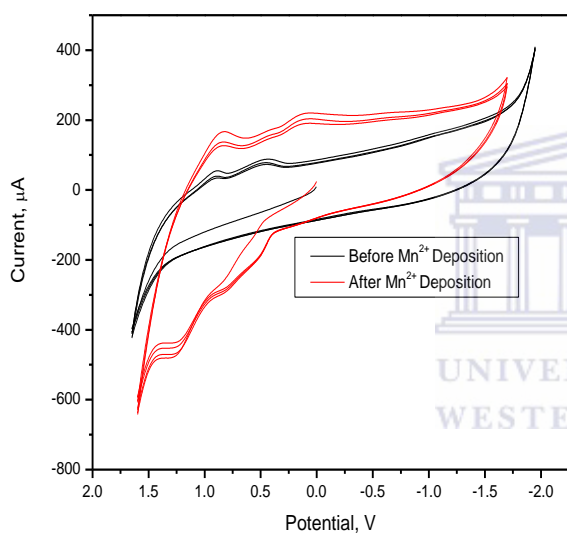
The CVs Mn_xO_y -modified electrodes in fresh portion of aq. NH_4Cl (0.1 M) solution are presented in Figure 45. Its peak potential and anodic peak current data compiled in Table 9. Comparing the pre- and post-electrodeposition CVs, one can conclude that the deposition of Mn_xO_y on all electrodes was successful. Two pairs of stable anodic and cathodic peaks, which remained stable were evident, indicating the formation adherent films regardless of the electrode type. The peaks were also well resolved in each case. The peaks were observed at higher and higher potentials when going from left to right in the order PCPE/ Mn_xO_y < ILPCPE/ Mn_xO_y < ILCPE/ Mn_xO_y . However, based on comparison of the peak heights, the lowest amount of Mn_xO_y was deposited on PCPE, while the highest was for the IPCPE/ Mn_xO_y . The quantity of the film on the latter electrode could as high as four times or more compared to the former, but only slightly higher relative to ILPCPE/ Mn_xO_y .



(a)



(b)



(c)

Figure 45: CVs CVs of (a) PCPE/ Mn_xO_y , (b) ILPCPE/ Mn_xO_y , and (c) ILCPE/ Mn_xO_y in aq. $NH_4Cl(0.1 M)$ solution.

Table 9: Postdeposition E_{pa} , E_{pc} , and I_{pa} values of Mn_xO_y films in aq. $NH_4Cl (0.1 M)$ solution.

Electrode	E_{pa-I} / V	E_{pa-II} / V	E_{pc-I} / V	E_{pc-II} / V	$I_{pa-I} / \mu A$	$I_{pa-II} / \mu A$
PCPE/ Mn_xO_y	0.504	1.11	0.884	0.099	-28.3	-64.5
ILPCPE/ Mn_xO_y	0.797	1.31	0.780	0.080	-118	-229
ILCPE/ Mn_xO_y	0.831	1.25	-	-	-140	269

Aq. NaOAc solution as electrolyte

The CVs Mn_xO_y -modified electrodes in fresh portion of aq. NaOAc (0.1 M) solution are presented in Figure 46. Its peak potential and anodic peak current data are compiled in Table 10.

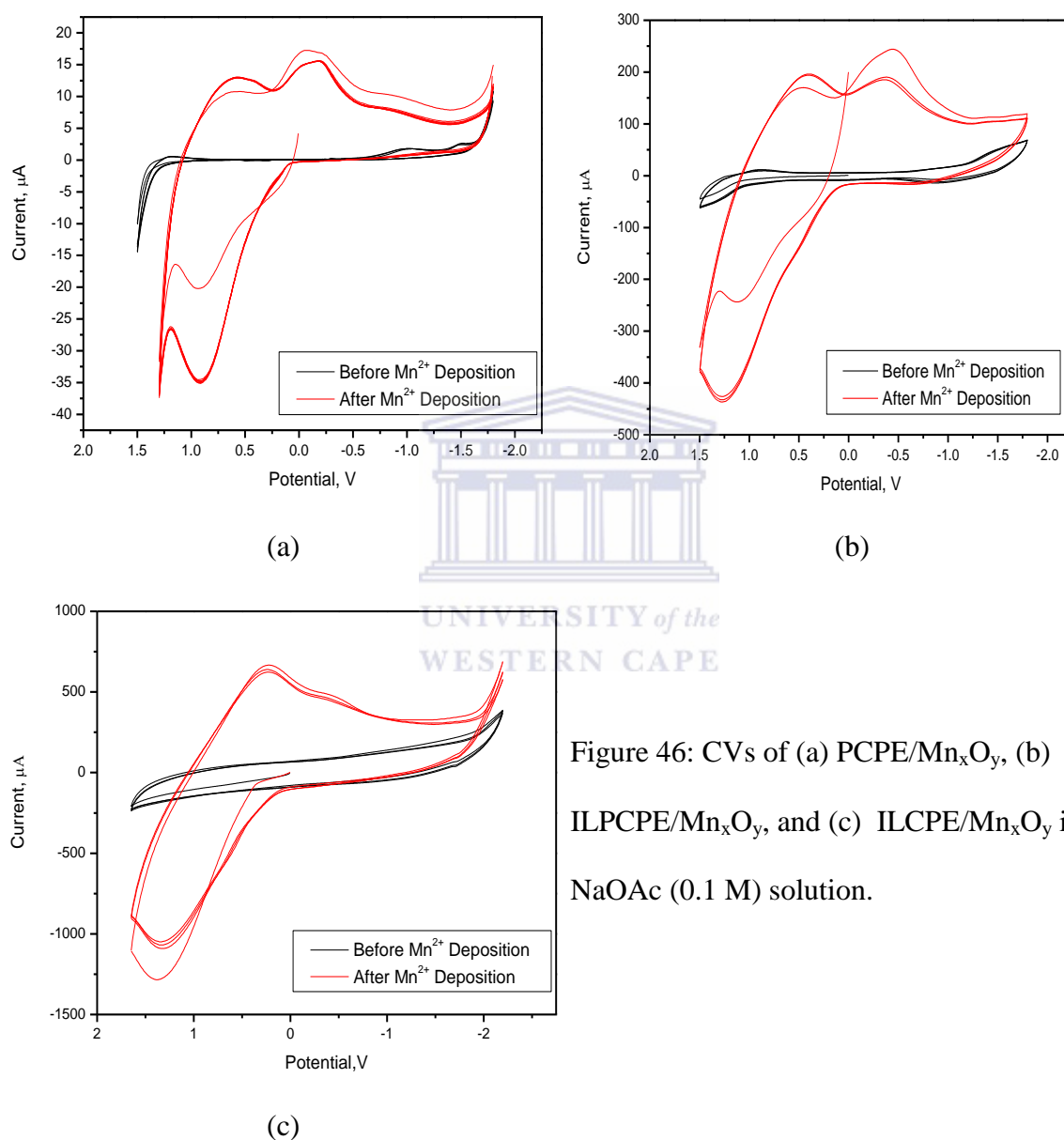


Figure 46: CVs of (a) PCPE/ Mn_xO_y , (b) ILPCPE/ Mn_xO_y , and (c) ILCPE/ Mn_xO_y in aq. NaOAc (0.1 M) solution.

Comparing the pre- and post-electrodeposition CVs, one can conclude that the deposition of Mn_xO_y on all electrodes was successful. One major anodic only and two cathodic peaks were observed in this electrolyte which remained stable were evident, indicating the formation

adherent films regardless of the electrode type. It appears the two anodic peaks exhibited in the other electrolytes were not resolved in this case. For PCPE/Mn_xO_y and ILPCPE/Mn_xO_y the two cathodic peaks were well resolved, but only slightly with regard to the ILPCPE/Mn_xO_y. The peaks were observed at higher and higher potentials when going from left to right in the order PCPE/Mn_xO_y < ILPCPE/Mn_xO_y < ILCPE/Mn_xO_y. Based on comparison of the peak heights, the highest amount of Mn_xO_y was deposited on ILCPE, and only about 50% and 10% deposited on the PCPE/Mn_xO_y and ILPCPE, respectively.

Table 10: Postdeposition E_{pa} , E_{pc} , and I_{pa} values of Mn_xO_y films in aq. NaOAc (0.1 M) solution.

Electrode	E_{pa-I} / V	E_{pa-II} / V	E_{pc-I} / V	E_{pc-II} / V	I_{pa-I} / μ A	I_{pa-II} / μ A
PCPE/Mn _x O _y	-	0.916	0.552	-0.164	-	-35.0
ILPCPE/Mn _x O _y	-	1.27	0.393	-0.375	-	-419
ILCPE/Mn _x O _y	-	1.34	0.251	-0.410	-	-964

Aq. NaClO₃ solution as electrolyte

The CVs Mn_xO_y-modified electrodes in fresh portion of aq. NaClO₃ (0.1 M) solution are presented in Figure 47. Its peak potential and anodic peak current data are compiled in Table 11. Comparing the pre- and post-electrodeposition CVs, one can conclude that the deposition of Mn_xO_y on all electrodes was successful. Two pairs of stable anodic and cathodic peaks which remained stable were evident, indicating the formation adherent films regardless of the electrode type. The peaks were also well resolved, except for the anodic peaks of PCPE/Mn_xO_y. The position of peaks shift to higher and higher potentials when going from left to right in the order PCPE/Mn_xO_y < ILCPE/Mn_xO_y < ILPCPE/Mn_xO_y. However, based on comparison of the peak heights, the highest amount of Mn_xO_y was estimated for the

ILPCPE/Mn_xO_y, followed by ILCP/Mn_xO_y (about 33% less), which in turn followed by PCPE/Mn_xO_y (about 85% less).

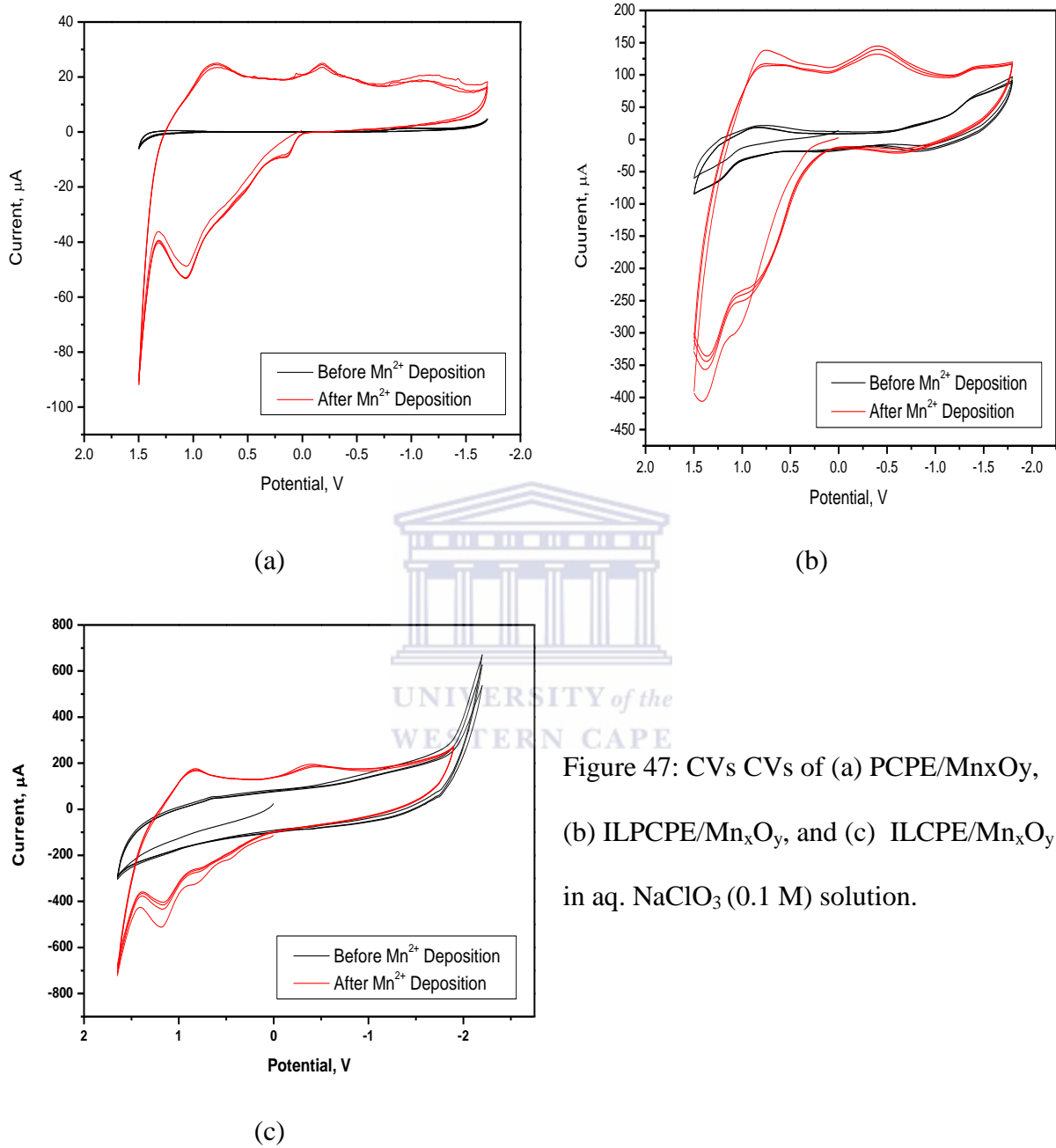


Figure 47: CVs CVs of (a) PCPE/Mn_xO_y, (b) ILPCPE/Mn_xO_y, and (c) ILCPE/Mn_xO_y in aq. NaClO₃ (0.1 M) solution.

Table 11: Postdeposition E_{pa} , E_{pc} , and I_{pa} values of Mn_xO_y films in aq. $NaClO_3$ (0.1 M) solution.

Electrode	E_{pa-I} / V	E_{pa-II} / V	E_{pc-I} / V	E_{pc-II} / V	I_{pa-I} / μA	I_{pa-II} / μA
PCPE/ Mn_xO_y	0.147	1.07	0.797	-0.195	-9.05	-52.6
ILPCPE/ Mn_xO_y	0.941	1.37	0.790	-0.417	-236	-344
ILCPE/ Mn_xO_y	0.760	1.13	0.837	-0.376	-124	-253

5.4.3 FTIR spectroscopic examination

Paraffin, the ionic liquid, and their 1:1 mixture

ATR-FTIR spectra of the paraffin oil (P), 1-methyl-3-octylimidazolium bis(trifluoromethylsulphonyl)imide (IL), and their 1:1 (v/v) mixture (P+IL) are presented in Figure 48. These were recorded in order to help identify the origin of IR absorption peaks in the IR spectra of CP materials. Though of the paraffin used in this study of spectroscopic grade, paraffin is in general known to be was a mixture of a wide range of medium-chain length, liquid alkanes with very low volatility. Its FTIR prominent peaks were assigned as follows: 2920 cm^{-1} ($\nu_{as}\text{ CH}_2$), 2852 cm^{-1} ($\nu_{as}\text{ CH}_3$), 1459 cm^{-1} ($\delta_{as}\text{ CH}_3$), 1377 cm^{-1} ($\delta_s\text{ CH}_3$), 722 cm^{-1} ($\delta\text{ CH}_3$ rocking). The IL (structure given in Figure 2) exhibited far more number of peaks as expected from its larger number of types of functional groups than paraffin has. Because of its alkyl groups (1-methyl or 3-octyl), this one as well exhibited some similar peaks as paraffin: 2931 cm^{-1} ($\nu_{as}\text{ CH}_2$), 2861 cm^{-1} ($\nu_{as}\text{ CH}_3$), and 1469 cm^{-1} ($\delta_{as}\text{ CH}_3$). However, these common peaks were relatively weaker in intensity and blue-shifted in position by about 10 cm^{-1} relative to the corresponding peaks of paraffin. This was probably because, in the IL, these functional groups exist in a lower concentration and belong to alkyl

groups bonded to the N atom unlike their free counterparts in paraffin. The rest of the peaks were assigned as follows: ν_s (C-F) at 1133 or 1179 cm^{-1} ; $\nu(\text{CF}_3) = 1348 \text{ cm}^{-1}$, 653 cm^{-1} , 613 cm^{-1} , 569 cm^{-1} , and 510 cm^{-1} ; $\nu_{\text{as}}(\text{R}_2\text{SO}_2) = 1348 \text{ cm}^{-1}$; $\nu_s(\text{R}_2\text{SO}_2) = 1179 \text{ cm}^{-1}$; and $\nu(-\text{C}=\text{N}^+-\text{R}_2) = 1573 \text{ cm}^{-1}$. The absence of the $\nu_s(\text{N-H})$ peak near 3500 cm^{-1} is also a hall mark of the IL. The spectrum of the mixture of paraffin and the IL exhibited peaks originating from both components. The assignment of the above peaks was done with the help of text [104, 105] and a correlation chart in a handbook [106]



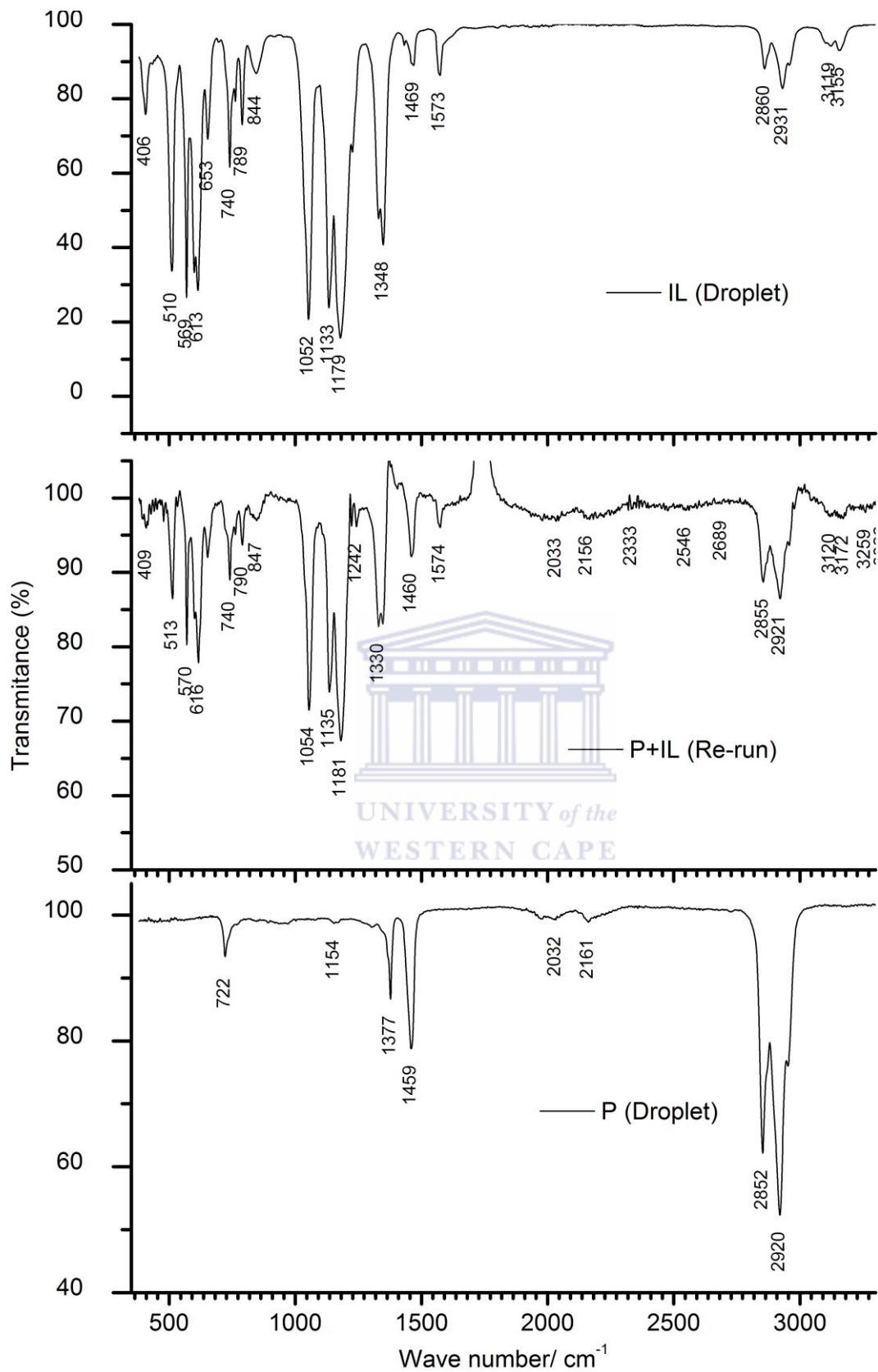


Figure 48: ATR-FTIR Spectra of the paraffin oil (P), ionic liquid (IL), and their 1:1 (v/v) mixture (P+IL)

Graphite, PCPE, ILPCPE, and ILCPE

ATR-FTIR spectra of as prepared PCP, ILPCP, and ILCP are presented in Figure 49. The spectrum of the graphite powder is also included. Its peak features at 2088 cm^{-1} , 2331 cm^{-1} , and 2666 cm^{-1} were used as hallmarks of graphite particles in the pastes. These peaks were indeed observed for all of the fresh CPs. However, the first distinct effect of the paste formation, regardless of its composition, was the drastic shift of the base-line absorption to a higher average transmittance: from 40% to over 80%. This indicated a large proportion of the graphite particles had their surfaces covered by the liquid binders when the pastes were formed. The respective spectra unequivocally reflected the corresponding compositions.

PCPE/Mn_xO_y, ILPCPE/Mn_xO_y, and ILCPE/Mn_xO_y

The ATR-FTIR spectra of PCPE/ Mn_xO_y, ILPCPE/ Mn_xO_y, and ILCPE/ Mn_xO_y prepared in aq. KCl are shown in Figure 49 together with the spectra of the respective CPEs before electrodeposition. The most obvious change after electrodeposition was the attenuation to obscurity of the characteristic peaks of graphite particles (2088 cm^{-1} , 2331 cm^{-1} , and 2666 cm^{-1}) regardless of the CP. Indeed, the graphite particles are the only sites where electrodeposition of Mn_xO_y is initiated. The electrodeposition resulted in a new cluster of particles with new morphology and optical characteristics masking the graphite particles. The second observation was that, regardless of the CP, the intensities of the paraffin and IL peaks decreased following the electrodeposition process. As the Mn_xO_y film grew both in thickness and sideways, into the inter-particle spaces and then over the surface regions occupied by the binder causing the latter to be less available for IR absorption. Finally, it was not obvious if there were any new IR absorption peaks due to the Mn_xO_y films deposited on ILPCPE and ILCPE. The PCPE/Mn_xO_y, however, exhibited three new ones at 1217 cm^{-1} , 1366 cm^{-1} , and 1737 cm^{-1} . The future work will have to verify and explain these two interesting observations.

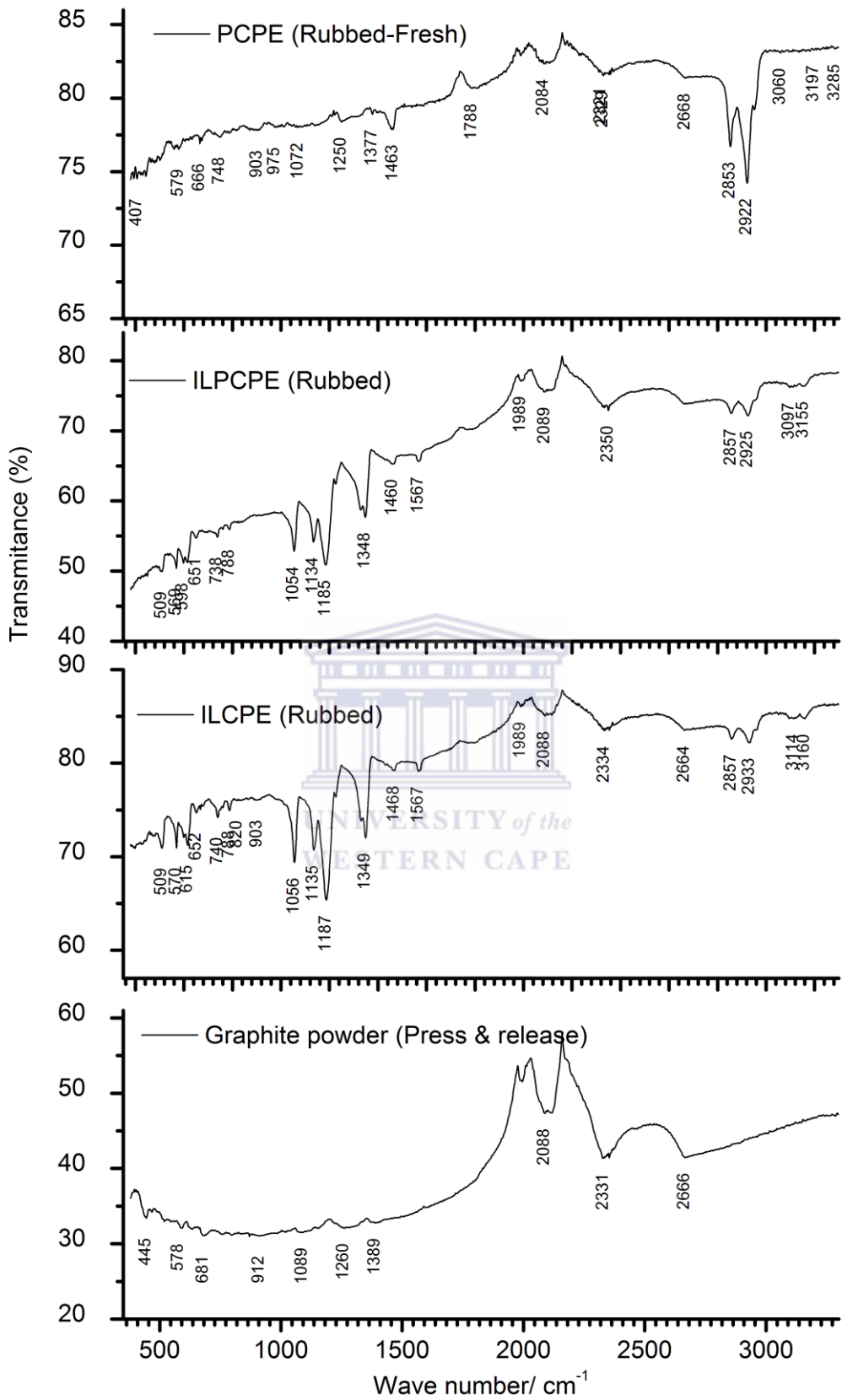


Figure 49: ATR-FTIR spectra of graphite powder, PCPE, ILPCPE, and ILCPE.

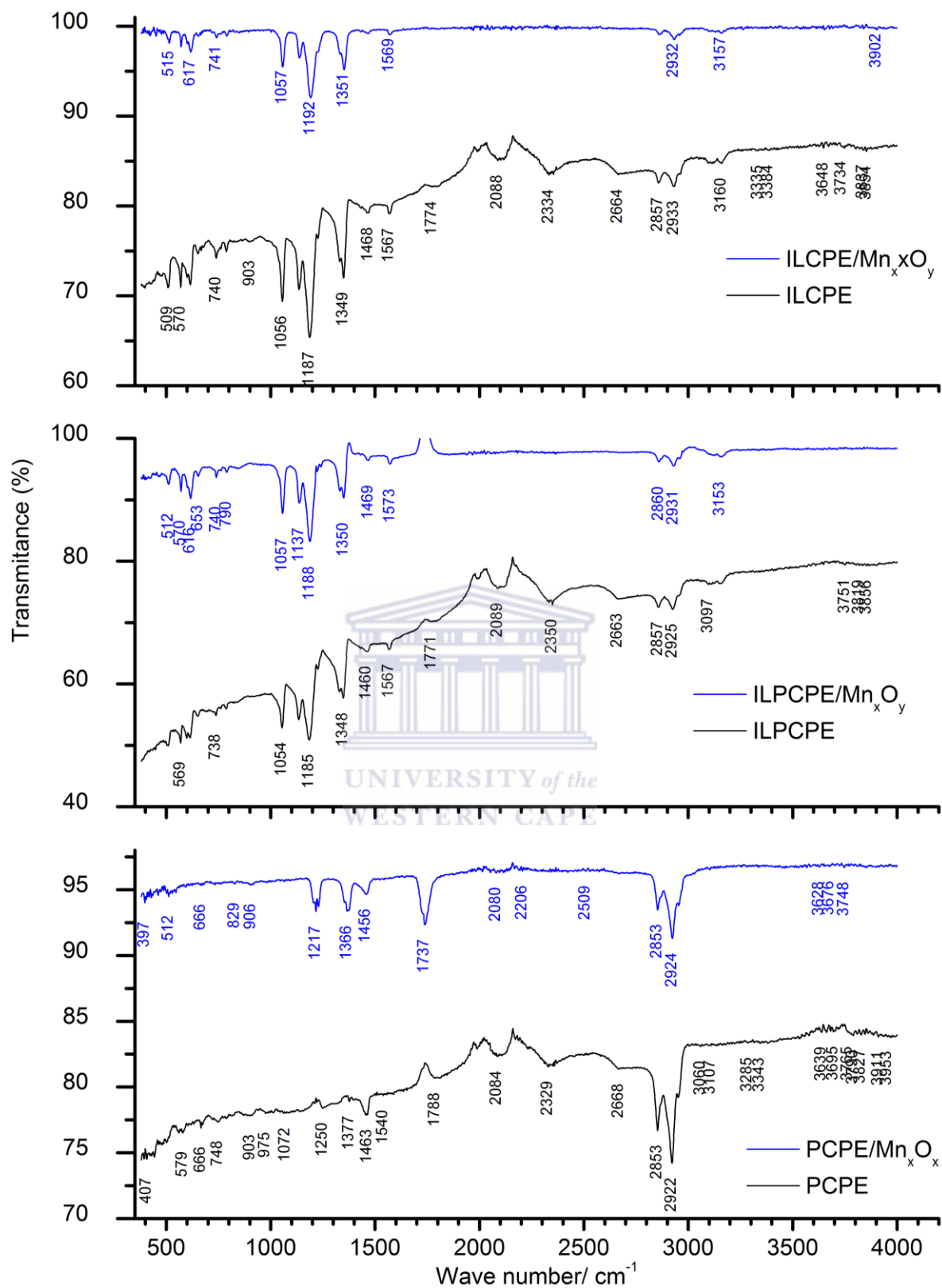
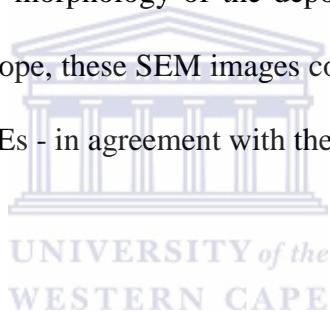
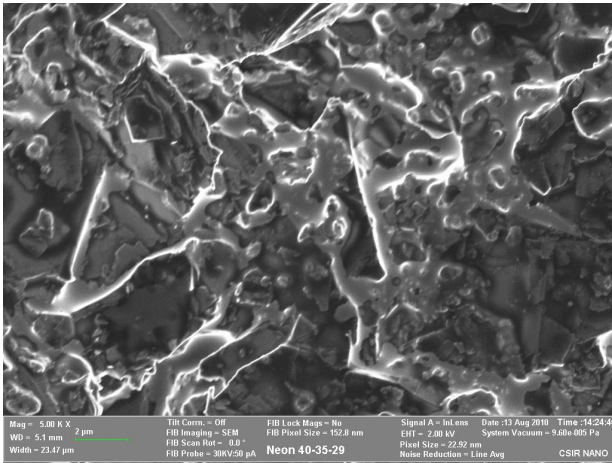


Figure 50: ATR-FTIR spectra PCPE/ Mn_xO_y, ILPCPE/ Mn_xO_y, and ILCPE/ Mn_xO_y prepared in aq. KCl (0.1 M) solution. The spectra of the CPEs before electrodeposition are also shown overlaid.

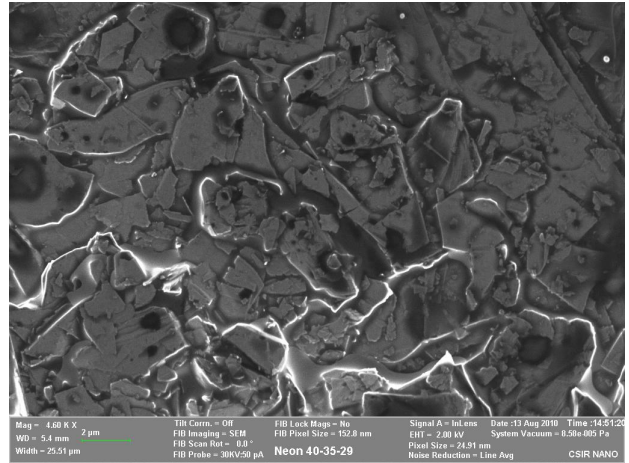
5.4.4 Scanning electron microscopic examination

SEM images of surface samples of PCPE (a & a'), ILPCPE (b & b'), and ILCPE (c and c') after the electrodeposition of Mn^{2+} in aq. KNO_3 (0.1 M) solution (a, b, & c) and KCl (0.1 M) solution (a', b' & c') are shown in Figure 51. Comparing each of these images with the images of the corresponding as-prepared fresh CPs samples (see Figure 14), one can see differences in shades and sub-micron features which might have been caused by electrodeposited clusters of Mn_xO_y . It is the edges of the graphite flakes that appear to have been altered more significantly in contrast with their planar sides as the latter appear less sharper and brighter after electrodeposition of the metal oxide. Thus, even though no information was available on the morphology of the deposited Mn_xO_y because insufficient resolution of the electron microscope, these SEM images confirm the electrodeposition of the Mn^{2+} was successful at all the CPEs - in agreement with the outcomes of the CV studies.

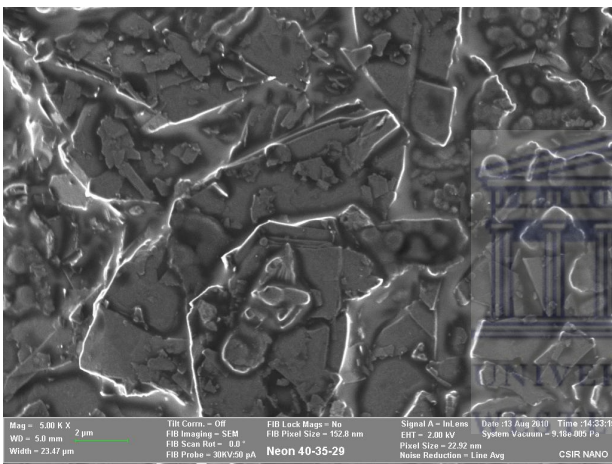




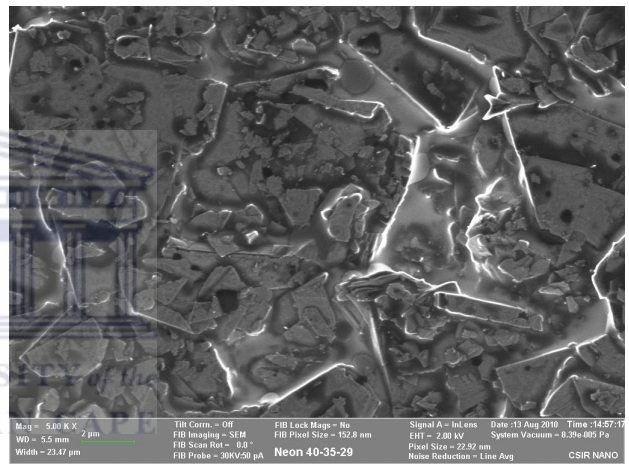
(a)



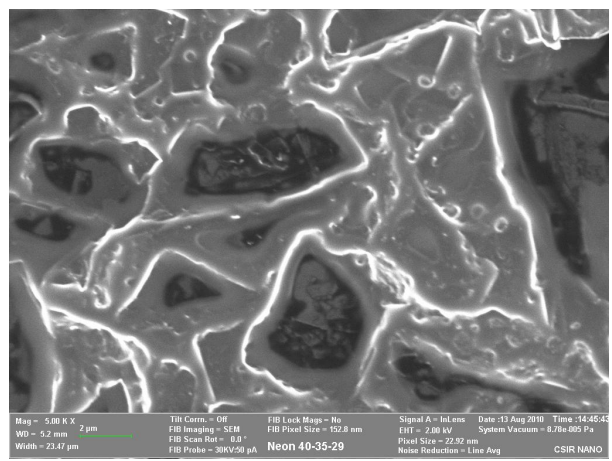
(a')



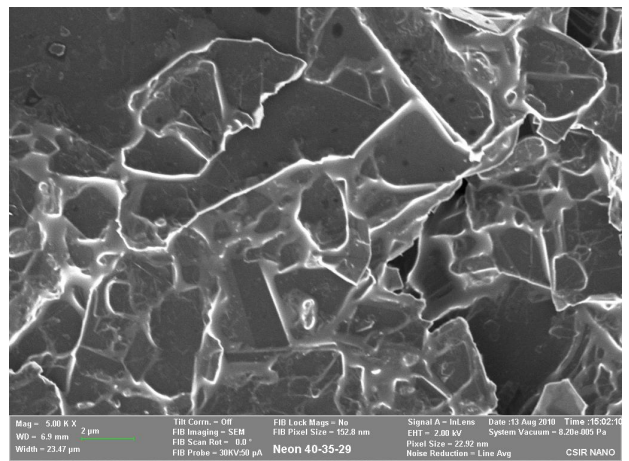
(b)



(b')



(c)



(c')

Figure 51: SEM images of surface samples of PCPE (a & a'), ILPCPE (b & b'), & ILCPE (c & c') after electrodeposition of Mn^{2+} in aq. KNO_3 (a, b, & c) and KCl solution (a', b' & c').

Page left blank



6. SUMMARY AND CONCLUSIONS

Carbon paste electrode (CPE) materials containing 1-methyl-3-octylimidazolium bis(trifluoromethylsulfonyl) imide [MOIM][Tf₂N] – a hydrophobic room temperature ionic liquid (IL) were studied in this work. CPEs with (a) the IL as the only binder (ILCPE) and (b) 1:1 (v/v) IL: paraffin mixture as the binder (ILPCPE) were prepared, electrochemically characterized, and applied to the electrodeposition of films of multivalent transition metal oxides (MV-TMO) from five precursor ions (Fe²⁺, Mn²⁺, Cu²⁺, Co²⁺, Ce⁴⁺) in aq. KCl (0.1 M) solution. The study also included the CV and EIS investigation of the electrode kinetics of the Fe(CN)₆^{3-/4-} redox system at these electrodes.

The IL caused an increase in background current of the CPE by about 100-folds relative to paraffin. In this regard, the electrodes compared according to following decreasing order: ILCP (~2.5 mA cm⁻²) > ILPCP > PCP (~0.05 mA cm⁻²). Even though the best, i.e. background peak free, working-potential ranges were +1.2 to -1.3 V (ILCP) and +1.0 to -1.2 V (ILPCP) in aq. KCl (0.1 M) solution, a potential window of +1.5 V to -1.8 V was available regardless of the CPE.

According to EIS results, the ILPCPE in aq. KCl (0.1 M) solution exhibited the behavior of a two-phase interface in contrast with the PCP and ILCP. The ILCPE/electrolyte interface exhibited a higher capacitive property than the PCP by more than three orders of magnitude as measured by the T_{CPE} parameter. However, the PCPE/electrolyte behaved more as an ideal capacitor than the other two which exhibited diffusion-like pseudo capacitive processes.

The electrode reaction of the redox-probe Fe(CN)₆³⁻ at these IL containing CPEs electrodes was faster than at the PCPE; however, most of the differences in the magnitudes of peak currents among the electrodes appeared to be because of differences in effective surface

areas. The redox potential of the $\text{Fe}(\text{CN})_6^{3-/4-}$ was not significantly affected by the ionic liquid and remained about 200 mV.

The IL enhanced the reduction peak current of the transition metal ions at the CP electrodes in aq. KCl, but it shifted the peak potentials to higher overpotentials. Changes in peak height and potential with cycle number strongly indicated the occurrence of alterations in surfaces of both PCP and ILPCP electrodes. This indicated that the electrode reaction was influenced by the presence of the ionic liquid. Formation of electrodeposited films onto the CPEs was confirmed for Fe^{2+} , Co^{2+} , and Mn^{2+} by new and stable post-electrodeposition cathodic and anodic peaks. Relative values these new peaks (peak heights) indicated that the amount of the electrodeposit films on the ILPCPE surface was much higher than that for the other two electrodes. CVs of H_2O_2 as a redox probe supported the same conclusions.

The electrodeposition of Mn^{2+} was effective in seven types of aqueous electrolytes (KCl, NaCl, NH_4Cl , NaClO_3 , LiCl, KNO_3 , CH_3COONa) according to the hallmarks observed during the respective electrodeposition and post-electrodeposition CVs. The formation of electrodeposited films was confirmed by the disappearance of the IR peaks characteristic of graphite particles, and appearance of new shades and submicron features in the ATR-FTIR spectra and SEM images recorded for surface samples after electrodeposition.

This study demonstrated that the use of this IL alone or in combination with paraffin as a binder in the development of viable alternative CPE materials with superior performance for the electrodeposition of MV-TMOs films than the traditional paraffin CPE. In combination with the advantages of easy preparation methods and physical “morpheability” in to any shape, these CPEs will be more useful in electrochemical technologies based on high-surface area MV-TMO films in general, and Mn_xO_y films in particular. For instance, these could be supercapacitors, solar cells, and water and atmospheric treatment technologies. Their broad

potential windows meant the ILPCPE and ILCPE provide an alternative, electrochemically inert surface for the study and sensing of a wide range of substances.



7. BIBLIOGRAPHY

1. Wang, S.F.X., Hua Yu Zeng, Qing Xiang, *Design of carbon paste biosensors based on the mixture of ionic liquid and paraffin oil as a binder for high performance and stabilization*. *Electrochemistry Communications*, 2007. **9**(4): p. 807-812.
2. Schmuki, P., *From Bacon to barriers: a review on the passivity of metals and alloys*. *Journal of Solid State Electrochemistry*, 2002. **6**(3): p. 145-164.
3. Waryo, T., et al., *Amperometric Hydrogen Peroxide Sensors with Multivalent Metal Oxide-Modified Electrodes for Biomedical Analysis 13th International Conference on Biomedical Engineering*, C.T. Lim and J.C.H. Goh, Editors. 2009, Springer Berlin Heidelberg. p. 829-833.
4. Zhang, H., Bu, L., Li, M., Hong, K., Visser, A.E., Rogers, R.D. and Mays, J.W. , *Homopolymerization and Block Copolymer Formation in Room-Temperature Ionic Liquids*. *ACS Symposium Series*, 2002. **828**: p. 114-124.
5. Chou, S., Cheng Fangyi , Chen Jun *Electrodeposition synthesis and electrochemical properties of nanostructured γ -MnO₂ films*. *Journal of Power Sources*, 2006. **162**: p. 727-734.
6. Peulon, S., et al., *Thin layers of iron corrosion products electrochemically deposited on inert substrates: synthesis and behaviour*. *Electrochimica Acta*, 2004. **49**(17-18): p. 2891-2899.
7. Švancara, I., Walcarius A., Kalcher K., Vytřas K., *Carbon paste electrodes in the new millennium*. *Central European Journal of Chemistry*, 2009. **7**(4): p. 598-656.
8. Mikyše, T., Svancara I., Kalcher K., Bartos M., Vytras K., Ludvik J., *New Approaches to the Characterization of Carbon Paste Electrodes Using the Ohmic Resistance Effect and Qualitative Carbon Paste Indexes*. *Anal. Chem.*, 2009. **81**: p. 6327-6333.

9. Adams, R.N., *Carbon Paste electrodes* Anal. Chem., 1958. **30**: p. 1576.
10. Svancara, I., Vytras K., Kalcher K., Walcarius A., Wang J., *Carbon Paste Electrodes in Facts, Numbers, and Notes: A Review on the Occasion of the 50-Years Jubilee of Carbon Paste in Electrochemistry and Electroanalysis*. Electroanalysis, 2009. **21**: p. 7-28.
11. Ivan, S., Karel Vytras, Kurt Kalcher, Alain Walcarius, Joseph Wang, *Carbon Paste Electrodes in Facts, Numbers, and Notes: A Review on the Occasion of the 50-Years Jubilee of Carbon Paste in Electrochemistry and Electroanalysis*. Electroanalysis, 2009. **21**(1).
12. Wei, S., Yuanyuan Duan, Yinzhuo Li, Hongwei Gao, Kui Jiao, *Electrochemical behaviors of guanosine on carbon ionic liquid electrode and its determination*. Talanta, 2009. **78**: p. 695-699.
13. Adams, R.N., *Electrochemistry at solid electrodes*. Dekker, New York, 1969.
14. Tasis, D., Tagmatarchis, N., Bianco, A., Prato, M., *Chemistry of Carbon Nanotubes* Che. Rev., 2006. **106**: p. 1035-1136.
15. Pei, L., Hongbo Sang, Zhimei Sun, *Cloud point extraction and graphite furnace atomic absorption spectrometry determination of manganese(II) and iron(III) in water samples*. Journal of Colloid and Interface Science, 2006. **304**: p. 486-490.
16. Ongera, G.B.E., Kumara Swamy, Umesh Chandra, B.S. Sherigara, *Simultaneous detection of dopamine and ascorbic acid using polyglycine modified carbon paste electrode: A cyclic voltammetric study*. Journal of Electroanalytical Chemistry, 2009. **636**: p. 80-85.
17. Svancara, I., Karel Vytras, Jiri Barek, and Jiri Zima, *Carbon Paste Electrodes in Modern Electroanalysis*. Critical Reviews in Analytical Chemistry, 2001. **31**(4): p. 311-345.

18. Karel, V., Ivan Svancara, Radovan Metelka, *Carbon paste electrodes in electroanalytical chemistry*. Journal of the Serbian Chemical Society, 2009. **74**(10).
19. Schachl, K., Alemu Hailemichael, Kalcher K., Moderegger Helmut, Svancara Ivan, Vytras Karel, *Amperometric determination of hydrogen peroxide with a manganese dioxide film-modified screen printed carbon electrode*. Fresenius' Journal of Analytical Chemistry, 1998. **362**(2): p. 194-200.
20. Ikede, S., Sutake H., Kohri Y., *Flow injection analysis with an amperometric detector utilizing the redox reaction of iodate ion*. Chem. Lett., 1984. **6**: p. 873-876.
21. Szebelledy, L., Somogyi Z., *Coulometric analysis as methods of precision. V. Determination of hydrazine*, Z. Anal. Chem., 1938. **112**: p. 391-395.
22. Svancara, I.S.K., *Testing of unmodified carbon Paste electrodes* Chem. Listy, 1999. **93**: p. 490-499.
23. Bengi, U.S.A.O., *Electroanalytical Application of Carbon Based Electrodes to the Pharmaceuticals*. Analytical Letters, 2007. **40**(5): p. 817-853.
24. Yiyi, S., Yougen Tang, Hongtao Liu, Ping He, *Electrochemical determination of hydroquinone using hydrophobic ionic liquid-type carbon paste electrodes*. Chemistry Central Journal, 2010. **4**: p. 17.
25. Kalcher, K., *Chemically modified carbon paste electrodes in voltammetric analysis*. . Electroanalysis, 1990. **60**: p. 483-493.
26. Spichiger-Keller, U.E., *Chemical Sensors and Biosensors for Medical and Biological Applications*. Wiley-VCH, Weinheim, 1998(© 1998).
27. Waryo, T.T., Vytras, K., Kalcher K. (Eds.), *Sensing in Electroanalysis*. University of Pardubice, Czech Republic, EU, 2005: p. 145-191.

28. Waryo, T.T., *Metal oxide-modified carbon amperometric H₂O₂-transducers and oxidase-biosensors*, PhD thesis, January 11, 2006. Institute of Chemistry, Department of Analytical Chemistry, K.F. University of Graz, Austria.
29. Grygar, T., *Electrochemistry of transition metal oxides and hydroxides in aqueous environment*. Institute of Inorganic Chemistry, Czech Republic, 2002.
30. READE[®], *Reade Advanced Materials offers: Magnetite (Fe₃O₄) powder*. Available online: http://www.reade.com/Products/Minerals_and_Ores/magnetite.html (©1997 Reade Advanced Materials), July 2005.
31. Cox, P.A., *Transition Metal Oxides – an introduction to their electronic structures and properties*. Clarendon press, Oxford, 1992: p. 24.
32. Coedy, J.M.D., Chien, C. L., *Half-metal ferromagnetic oxides*. 2003, 2003. **28**: p. 720-724.
33. Franger, S., Berthet P., Berthon J., *Electrochemical synthesis of Fe₃O₄ nanoparticles in alkaline aqueous solutions containing complexing agents*. J Solid State Electrochem, 2004. **8**(2004): p. 218-223.
34. Koslow, C.M., *Bulletin of the Chemical Society of Japan*. 1974. **47**: p. 1646-1650.
35. Li, Y., Liao, Qian, Y., *Hydrothermal synthesis of ultrafine α-Fe₂O₃ and Fe₃O₄ powders*. Materials Research Bulletin, 1998. **33**: p. 841-844.
36. Abe, O.K., Masafumi; Umezawa, Reiko, *Mechanochemical redox process for synthesis of fine magnetite powders*. Funtai Kogaku (Japan), 2005. **42**: p. 199-205.
37. Alcalá, M.D.C., J. M.; Real, C.; Grygar, T.; Nejezchleba, M.; Subart, J.; Petrovsky, E., *Synthesis of nanocrystalline magnetite by mechanical alloying of iron and hematite*. Journal of Material Science, 2004. **39**: p. 2365-2370.
38. Mouhandess, M.T., Chassagneux, F., Durand, B., Vitori, O., *Electrochemical reduction of hematite incorporated in a carbon paste electrode*. Comptes Rendus des

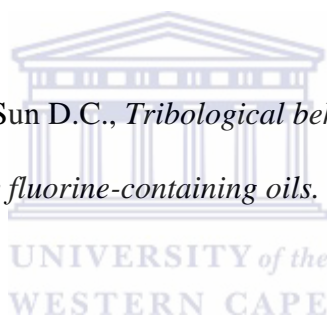
- Seances de l'Academie des Sciences, Serie C: Sciences Chimiques, 1980. **290**: p. 267-270.
39. Mouhandess, M.T., Chassagneux, F.; Durand, B.; Vitori, O., *Effect of iron oxide (α -Fe₂O₃) morphology on electrochemical behaviour*. Comptes Rendus des Seances de l'Academie des Sciences, Serie 2: Mecanique-Physique, Chimie, Sciences de l'Universe, Sciences de la Terre, 1982. **290**: p. 571-574.
 40. Mouhandess, M.T., Chassagneux, F.; Durand, B.; Sharara, Z. Z.; Vitori, O., *Some Advantages of carbon paste electrodes in the morphological study of finely divided iron oxides*. Journal of Material Science, 1985a. **20**: p. 3289-3299.
 41. Mouhandess, M.T., Chassagneux, F.; Durand, B.; Vitori, O., *Electroreactivity of iron(III) oxides incorporated in a carbon paste electrode*. Material Science Monographs 1985b. **28A**: p. 549-554.
 42. Grygar, T., *Phenomenological kinetics of irreversible electrochemical dissolution of metaloxide microparticles*. J. Solid State Electrochem, 1998. **2**: p. 127-136.
 43. Scholz, F., Nitschke, L., Henrion, G., *A new procedure for fast electrochemical analysis of solid materials*. Naturwissenschaften, 1989. **76**: p. 71-72.
 44. Keiser, J.T., Brown, C. W., Heidersbach, R. H. , *The electrochemical reduction of rust films on weather steel surface*. J. Electrochem. Soc., 1982. **129**: p. 2686-2689.
 45. Grenier, J.C., Wattiaux A.; Fournes L., Pouchard M., Etournea J., *The electrochemical oxidation: a new way for preparing highly oxidized ferrites*. J. de Physique IV **7** (C1, 7th International Conference on Ferrites, 1996), 1997. **C1/49 – C1/52**.
 46. Mancey, D.S., Shoesmith, D. W., Lipkowski, J., McBride A. C., Noel J., *An electrochemical investigation of dissolution of magnetite in acidic electrolytes*. J. Electrochem. Soc., 1993. **140**: p. 637.

47. White, A.F., Peterson, M. L., Hochella, Jr M. F., *Electrochemistry and dissolution kinetics of magnetite and ilmenite*. *Geochimica et Cosmochimica Acta*, 1994. **58**: p. 1859-1875.
48. Haruyama, S.M., K., *The dissolution of magnetite in acidic perchlorate solutions*. *Corrosion Science*, 1978. **18**: p. 263-274.
49. Sharara, Z.H.V., O.; Durand, B., *Electrochemical oxidation of divalent iron mixed oxides using carbon paste electrodes*. *Electrochimica Acta*, 1984. **29**: p. 1689-1693.
50. Xiaoli, C., Guodong Liu, Yuehe Lin, *Amperometric biosensors based on carbon paste electrodes modified with nanostructured mixed-valence manganese oxides and glucose oxidase*. *Nanomedicine: Nanotechnology, Biology, and Medicine*, 2005. **1**: p. 130- 135.
51. Schachl, K., Alemu Hailemichael, Kalcher Kurt, Jezkova Jitka, Svancara Ivan, Vytras Karel, *Amperometric Determination of Hydrogen Peroxide With a Manganese Dioxide-modified Carbon Paste Electrode Using Flow Injection Analysis*. *Analyst*, 1997. **122**(9): p. 985-989.
52. Negussie, W.B., Petr Kotzian, Klemens Schachl , Hailemichael Alemuc, Emir Turkušić , Amira Čopra, Helmut Moderegger, Ivan Švancara, Karel Vytřas, Kurt Kalcher, *(Bio)sensors based on manganese dioxide-modified carbon substrates: retrospections, further improvements and applications*. *Talanta*, 2004. **64**: p. 1151-1159.
53. Xingwang, Z., Zhihui Guo, *Potentiometric determination of hydrogen peroxide at MnO₂-doped carbon paste electrode*. *Talanta*, 2000. **50**: p. 1157-1162.
54. Zhang, W., Cheng C.Y., *Manganese metallurgy review. Part I: Leaching of ores/secondary materials and recovery of electrolytic/chemical manganese dioxide*. *Hydrometallurgy*, 2007. **89**: p. 137-159.

55. Banks C.E., Moore R.R., Tomčík P., Peters J., Davis J., Komorsky-Lovric S., Compton, *Manganese detection in marine sediments: anodic vs. cathodic stripping voltammetry*. *Talanta*, 2000. **65**: p. 423-429.
56. Miroslav, K., Valery Kochev, *The potential of manganese in construction of electrodes modified with thin liquid films of lipids*. *Journal of Electroanalytical Chemistry*, 2004. **571**: p. 73-80.
57. Yuehe, L., Xiaoli Cui, Liyu Li, *Low-potential amperometric determination of hydrogen peroxide with a carbon paste electrode modified with nanostructured cryptomelane-type manganese oxides*. *Electrochemistry Communications*, 2005. **7**: p. 166-172.
58. Wei, D., Ari Ivaska, *Applications of ionic liquids in electrochemical sensors*. *Analytical Chimica Acta*, 2008. **607**: p. 126-135.
59. Wei, S., Dandan Wang, Ruifang Gao, Kui Jiao, *Direct electrochemistry and electrocatalysis of hemoglobin in sodium alginate film on a BMIMPF₆ modified carbon paste electrode*. *Electrochemistry Communications*, 2007. **9**: p. 1159-1164.
60. Matsumoto K., Ito Y., *Room temperature molten fluorometallates: 1-ethyl-3-methylimidazolium hexafluoroniobate(V) and hexafluorotantalate(V)*. *Journal of Fluorine Chemistry*, 2002. **115**: p. 133-135.
61. Ngo, H.L., LeCompte, K., Hargens, L., McEwen, A.B. , *Thermal Properties of Imidazolium Ionic Liquids*. *Thermochim. Acta*, 1998. **97**: p. 357-358.
62. Brennecke, J.F., Maginn E.J., *Ionic Liquids: Innovative Fluids for Chemical Processing*. *AIChE Journal*, 2001. **47**(11): p. 2384-2389.
63. Bartsch, R.A., Chun, S., Dzyuba, S.V., *Ionic Liquids as Novel Diluents for Solvent Extraction of Metal Salts by Crown Ethers*. *ACS Symposium Series*, 2002. **818**: p. 58-68.

64. Lu, Q., Wang H., Ye C., Liu W., Xue Q., *Room temperature ionic liquid 1-ethyl-3-hexylimidazolium-bis(trifluoromethylsulfonyl)-imide as lubricant for steel-steel contact*. Tribology International 2004. **37**: p. 547-552.
65. K. Matsumoto, R.H., . *A new room temperature ionic liquid of oxyfluorometallate anion: 1-Ethyl-3-methylimidazolium oxypentafluorotungstate (EMImWOF5)*. Journal of Fluorine Chemistry, 2005. **126**: p. 1095-1100.
66. Martyn, J.E., Kenneth R. Seddon, *Ionic liquids. Green solvents for the future*. Pure Appl. Chem., 2000. **72**(7): p. 1391–1398.
67. Hagiwara, R., Ito Y. , *Room temperature ionic liquids of alkylimidazolium cations and fluoroanions*. Journal of Fluorine Chemistry, 2000. **105**: p. 221-227.
68. Zhou, Y., Schattka, J.H., Antonietti, M., *Room-Temperature Ionic Liquids as Template to Monolithic Mesoporous Silica with Wormlike Pores via a Sol-Gel Nanocasting Technique*. NanoLetters, 2004. **4**(3): p. 477-481.
69. Law, G., Watson P.R. , *Surface Tension Measurement of N-Alkylimidazolium Ionic Liquids*. Langmuir, 2001a. **17**: p. 6138-6141.
70. Bowers, J.a.V.-G., M.C., *Surface Ordering of Amphiphilic Ionic Liquids*. Langmuir, 2004. **20**: p. 309-312.
71. Ming-Jay, D., Po-Yu Chen, I-Wen Sun, *Electrochemical study and electrodeposition of manganese in the hydrophobic butylmethylpyrrolidinium bis((trifluoromethyl)sulfonyl) imide room-temperature ionic liquid*. Electrochimica Acta, 2007. **53**: p. 1931-1938.
72. Virtanen, S., *Electrochemical Theory* in *Encyclopedia of Electrochemical Power Sources*, G. Editor-in-Chief: Jürgen, Editor 2009, Elsevier: Amsterdam. p. 56-63.
73. Earle, M.J., McCormac, P.B., Seddon, K.R., *Diels-Alder Reactions in Ionic Liquids*. Green Chemistry, 1999. **1**: p. 23-25.

74. Earle, M.J., Seddon, K.R., Adams, C.J., Roberts, G., *Friedel - Crafts Reactions in Room Temperature Ionic Liquids*. Chemical Communications (Cambridge), 1998. **19**: p. 2097-2098.
75. Park, S., Kazlauskas R.J., *Biocatalysis in Ionic Liquids-Advantages Beyond Green Technology*. Current Opinion in Biotechnology, 2003. **14**: p. 432-437.
76. Mazurkiewicz, J.H., Innis, P.C., Wallace, G.G., MacFarlane, D.R. and Forsyth, M., *Conducting Polymer Electrochemistry in Ionic Liquids*. Synthetic Metals, 2003. **135-136**: p. 31-32.
77. Poole, C.F., *Chromatographic and spectroscopic methods for the determination of solvent properties of room temperature ionic liquids*. Journal of Chromatography A, 2004. **1037**: p. 49-82.
78. Liu, W., Chen Y., Ou Z., Sun D.C., *Tribological behavior of sialon ceramics sliding against steel lubricated by fluorine-containing oils*. Tribology International, 2002. **35**: p. 503-509.
79. Lu, Q., Ye C., Liu W., Xue Q., *Room temperature ionic liquid 1-ethyl-3-hexylimidazolium-bis(trifluoromethylsulfonyl)-imide as lubricant for steel-steel contact*. Tribology International, 2004. **37**: p. 547-552.
80. Chen, H., Wang Yuling, Liu Ying, Wang Yizhe, Qi Li, Dong Shaojun, *Direct electrochemistry and electrocatalysis of horseradish peroxidase immobilized in Nafion-RTIL composite film*. Electrochemistry Communications, 2007. **9**: p. 469-474.
81. Mohammad, R.G., Negar Motakef-Kazemi, Parviz Norouzi, and Sepideh Khoei, *A Modified Ho^{3+} Carbon Paste Electrode Based on Multi-walled Carbon Nanotubes (MWCNTs) and Nanosilica*. Int. J. Electrochem. Sci., 2009. **4**: p. 906-913.
82. Bard, J.A., Faulkner R. Larry *Electrochemical Methods: Fundamentals and Applications*. Wiley, 2000. **2nd Edition**.



83. Nicholson, R.S., *Theory and Application of Cyclic Voltammetry for Measurement of Electrode Reaction Kinetics*. Anal. Chem., 1965. **37**: p. 1351-1355.
84. Rusling, J.F., Forster R.J. , *Electrochemical catalysis with redox polymer and polyion-protein films* Journal of Colloid and Interface Science, 2003. **262**: p. 1-15.
85. Laviron, E., *Adsorption, autoinhibition and autocatalysis in polarography and in linear potential sweep voltammetry*. Electroanalytical Chemistry and Interfacial Electrochemistry, 1974. **52**: p. 355-393.
86. Baroukov, E., Macdonald J.R. , *Impedance Spectroscopy- Theory, Experiment, and Application* Wiley-Interscience, 2005.
87. Delahay, P., *New Instrumental Methods in Electrochemistry*. Wiley-Interscience, New York, 1954: p. Chap. 7.
88. Astavef, M.G., Russ. J. Electrochem, 2000. **36**: p. 274.
89. Barsoukov, E., Macdonald J.R. , *Impedance Spectroscopy- Theory, Experiment, and Application* Wiley-Interscience, 2005.
90. Scriber Associates, Inc., ZViewTM Impedance/gain phase graphing and analysis software operating manual (version 3.2), Revised 7/2007
91. Waryo, T.T., Lecture notes.
92. Lasia, A., Bockris J., White R.E., *Modern aspects of electrochemistry*. Kluwer Academic/ Plenum Publishers, NY, 1999. **32**: p. 143-248.
93. Antoine, A., *Principles of Nuclear Magnetic Resonance* Cambridge University Press: Cambridge, UK, 1998: p. 895.
94. Wei, L., Fang W., Dan L., Min X.Q., Gu Y., Xin S.Z., *FTIR-ATR detection of proteins and small molecules through DNA conjugation*. Sensors and Actuators B, 2006. **114**: p. 445-450.

95. Chittur, K.K., *FTIR/ATR for protein adsorption to biomaterial surfaces* Biomaterials, 1998. **19**: p. 357-369.
96. Oberg, K.A., Fink A.L., *A new attenuated total reflectance Fourier transform infrared spectroscopy method for the study of proteins in solution* Anal. Biochem., 1998. **256**: p. 92-106.
97. Arzate-Vazques, J., Chanona-Perez J.J., Calderon-Dominguez G., Terres-Rogers E., Garibay-Febles V. Martinez-Rivas A., Gutierrez-Lopez G.F., *Microstructural characterization of chitosan and alginate films by microscopy techniques and texture image analysis*. Carbohydrate Polymer, 2012. **87**: p. 289-299.
98. Kozarac, Z., Mobius D., Martin Romero M.T., *Characterisation of Aquatic Natural Microlayers by Monolayer Techniques and Brewster Angle Microscopy*. Wat. Res., 2000. **34**: p. 1463-1472.
99. Takeshi, N., Jean-Louis E., Jacques-Louis D.B. , *A scanning electron microscopy (SEM) study of sediments from Lake Cristol, southern French Alps, with special reference to the identification of the Pinus cembra and other Alpine Pinus species based on SEM pollen morphology* Review of Palaeobotany and Palynology, 2000. **108**: p. 1-15.
100. Imogen, P., Geoffrey E.L. , *Alternative SEM Techniques for observing pyritised fossil material*. Review of Palaeobotany and Palynology, 2000. **112**: p. 287-295.
101. Liu, H., P. He, Z. Li, C. Sun, L. Shi, Y. Liu, G. Zhu, J. Li., *An ionic liquid-type carbon paste electrode and its polyoxometalate-modified properties*. Electrochemistry Communications, 2005a. **7**: p. 1357-1363.
102. Davies, T.J., R.R. Moore, C.E. Banks, R.G. Compton, *The voltammetric response of electrochemically heterogeneous surfaces*. J. Electroanal. Chem., 2004. **574**: p. 123-152.

103. Davies, T.J., S. Ward-Jones, C.E. Banks, J. del Campo, R. Mas, F.X. Munoz, R.G. Compton, *The cyclic and linear sweep voltammetry of regular arrays of microdisc electrodes: Fitting of experimental data*. J. Electroanal. Chem., 2005. **585**: p. 51-62.
104. Gunzler, H., Gremlich H.U. , *IR Spectroscopy - An Introduction*. © WILEY-VCH, Weinheim, 2002.
105. Robinson, J.W., Frame E. M. S. , Frame G. M., *Undergraduate instrumental analysis, 6th Ed.*, Marcel Dekker © 2005 NY.
106. Lide, D.R.E., *Handbook of chemistry and physics*, CRC Press ©2002.



Page Left Blank



Page Left Blank

